Influence of materials properties on the performance of triboelectric nanogenerators harvesting systems

Carlos Callaty Garcia
Mestrado em Engenharia Física
Departamento de Física e Astronomia
2022

Orientador
Prof. Dr. João Oliveira Ventura, Investigador principal, Faculdade de Ciências da Universidade do Porto

U.PORTO

FACULDADE DE CIÊNCIAS
UNIVERSIDADE DO PORTO

Todas as correções determinadas pelo júri, e só essas, foram efetuadas.

O Presidente do Júri,

Porto, _____/_____/_____

UNIVERSIDADE DO PORTO

MASTERS THESIS

Influence of materials properties on the performance of triboelectric nanogenerators harvesting systems

Author:
Carlos Miguel CALLATY Garcia

Supervisor:
João VENTURA

A thesis submitted in fulfilment of the requirements
for the degree of MSc. Engineering Physics

at the

Faculdade de Ciências da Universidade do Porto
Departamento de Física e Astronomia

December 13, 2022

" It's not about how many times you fall down, but how many times you get back up. "

Abraham Lincoln

Declaração de Honra

Eu, Carlos Miguel Callaty Garcia, inscrito no Mestrado em engenharia física da Faculdade de Ciências da Universidade do Porto declaro, nos termos do disposto na alínea a) do artigo 14.º do Código Ético de Conduta Académica da U.Porto, que o conteúdo da presente dissertação/relatório de estágio/projeto "Influence of materials properties on the performance of triboelectric nanogenerators harvesting systems" reflete as perspetivas, o trabalho de investigação e as minhas interpretações no momento da sua entrega.

Ao entregar esta dissertação/relatório de estágio/projeto "Influence of materials properties on the performance of triboelectric nanogenerators harvesting systems" , declaro, ainda, que a mesma é resultado do meu próprio trabalho de investigação e contém contributos que não foram utilizados previamente noutros trabalhos apresentados a esta ou outra instituição.

Mais declaro que todas as referências a outros autores respeitam escrupulosamente as regras da atribuição, encontrando-se devidamente citadas no corpo do texto e identificadas na secção de referências bibliográficas. Não são divulgados na presente dissertação/relatório deestágio/projeto "Influence of materials properties on the performance of triboelectric nanogenerators harvesting systems" quaisquer conteúdoscuja reprodução esteja vedada por direitos de autor. Tenho consciência de que a prática de plágio e auto-plágio constitui um ilícito académico.

Carlos Callaty

Porto, 9 de dezembro de 2022

Acknowledgements

I would like to thank many people, ranging from friends and family to colleagues. Starting with my supervisor, professor João Ventura, I would want to thank him not only for the guidance provided in the thesis, but also for being a fantastic person through difficult situations, some of which were not related to the thesis.

For the colleagues that worked on triboelectrics, Isabel Gonçalves taught me how to work with COMSOL. She has also given numerous suggestions and provided countless opportunities for scientific conversation that resulted in new ideas for the research. I've learned a lot from it all!

Everything has a starting point, and for this thesis, in addition to professor João Ventura's excellent advice, suggestions and great discussions about this work throughout the thesis, Cátia Rodrigues also made important contributions in this area.

Fernando and Pedro Cruz, engineers from the mechanical and electronic laboratories, were crucial in creating the pieces and connections for the experimental arrangement. I'm grateful for their assistance and advice with the setup build.

Now, for my friends, they gave me a lot of great moments through out my journey on university of high and lows and had an infinite patience to wait while I would finish my lunch! From this last statement, I would like to thank João Silva, Bruno Mota, Luís Dias, Alexandra Oliveira, Rita Bugalhão, Beatriz Soares, Cláudia Rodrigues, José Mesquita, Nuno Mendes, Ana Silva and Francisco Carvalho for the amusing moments at lunch and study breaks, as well as for being fantastic friends.

Luís Dias deserves special recognition for being the best friend I ever had. First and foremost, he has given advice while respecting my decision. Second, I've learned a lot about music, not only through composing but also through listening to music and attending concerts. It has broadened my perspective on the music world, particularly the metal scene.

Finally, and most importantly, my family. I'd like to express my gratitude to my parents and grandparents for their support. My grandfather, Helder Santos, constantly gave me things to learn and encouraged me to study hard so that I would not make the same mistake he made by not studying. He was quite knowledgeable, and I am now finishing

my master's degree in a field that he could have studied. When I was younger, my grandfather, Helder Santos, and grandmother, Maunela Santos, were always there for me. Now it is my turn to work and help them!

To round off the acknowledgements, my parents, Carlos and Ana Garcia, were always supportive of my decisions and encouraged and assisted me in pursuing the course I desired. Choosing the University of Porto over one in Lisbon that was closer to my home was undoubtedly the best decision I had made, and they provided me with everything I needed to pursue my ambition. My mother and I almost died at birth, and I had issues as a result of being born prematurely at only 30 weeks and developing hydrocephalus. Because of my parents' efforts and a bit of luck, I am a normal person with no complications or learning disabilities.

UNIVERSIDADE DO PORTO

Abstract

Faculdade de Ciências da Universidade do Porto
Departamento de Física e Astronomia

MSc. Engineering Physics

Influence of materials properties on the performance of triboelectric nanogenerators harvesting systems

by Carlos Miguel CALLATY Garcia

Triboelectric nanogenerators (TENGs) are an appealing energy harvester due to their environmental friendliness, low cost, and low maintenance in the face of the world's worsening climatic crisis. With diverse operating modes, such as contact-separation, sliding, single electrode, and freestanding, these devices convert mechanical into electrical energy and they can supply energy to various devices, such as in maritime and medicine applications.

In this work, the focus was on studying the contact-separation mode using numerical simulations and experimentally to better understand the optimisation of TENGs. In the numerical simulations, parameters such as TENG's area, triboelectric material thickness, and relative permittivity were varied and compared with an existing model, while in the experimental setup, the behaviour of TENGs in the 20 - 105 °C temperature was measured and analysed. For both studies, contact-separation TENGs are modelled as a double-plate capacitor where one material is fixed and the other comes into contact with it periodically, generating electrostatic charges. To evaluate TENGs' performance with the varying parameters, the open circuit voltage, short circuit current, optimum resistance, and maximum power output are used.

The numerical simulation results show that when the area (thickness) rises, the short circuit current increases (decreases) and the open circuit voltage increases (decreases). Furthermore, with an increase in area (thickness), the optimal resistance decreased (increased) and the power increased (decreased). Most of these results match the compared theoretical model and reasons were given for the difference observed for the open

circuit voltage. In the relative permittivity study, a comparison was made between a nanoparticle-doped material and one with the equivalent relative permittivity, in which they agreed with each other on the open circuit voltage and short circuit voltage, as predicted by the models. However, only those parameters match, and a charge correction to the surface material's with equivalent relative permittivity was made to better understand the relationship between relative permittivity and surface charge.

The performed temperature study used PDMS of various thicknesses and nanoparticle-doped PDMS with its own developed manufacturing process against copper and aluminium samples. As the temperature increased, a drop in the performance of the open circuit voltage and short circuit current was typically observed.

This work gave a better understanding of how TENG's performance is affected by varying its properties and temperature. For future work, increasing the working range of the setup while further researching and mitigating sample deterioration, improving the manufacturing process of PDMS nanoparticle-doped samples, and better understanding the unexpected tendencies of the open circuit voltage are the next steps following of this work.

UNIVERSIDADE DO PORTO

Resumo

Faculdade de Ciências da Universidade do Porto
Departamento de Física e Astronomia

Mestrado em Engenharia Física

Influência das propriedades dos materiais no desempenho de sistemas de nanogeneradores triboeléctricos

por Carlos Miguel CALLATY Garcia

Nanogeradores triboelétricos (TENGs) são coletores de energia que estão a despertar interesse devido a serem uma tecnologia limpa de baixo custo e baixa manutenção com o propósito de substituir energia vinda de combustíveis fósseis face à crise climática que está cada vez pior. Os TENGs têm vários tipos de operação que são os seguintes: contacto-separação, deslizamento, elétrodo único e o de camada de movimento livre. Todos estes modos convertem energia mecânica em elétrica que podem ser usados em várias aplicações (marítimas e medicina).

Neste trabalho usou-se o modo contacto-separação em simulações numéricas e numa experiência laboratorial para compreender melhor como otimizar os TENGs. Nas simulações numéricas variou-se os seguintes parâmetros do TENG: área, espessura dum material triboelétrico e a permitividade relativa. Os resultados destas simulações foram comparados com o modelo existente para o modo de contacto-separação. Na experiência laboratorial estudou-se como o desempenho do TENG é afetado com aumento da temperatura que vai desde 20 até 105 °C. Em ambos os estudos, o TENG de contacto-separação é modelado como um condensador de placas paralelas, onde um material está fixo e o outro desloca-se, entrando em contacto periodicamente com o material fixo, produzindo cargas eletrostáticas. Os parâmetros usados para avaliar o desempenho do TENG foram: tensão de circuito aberto, corrente de curto-circuito, resistência ótima e a potência máxima.

Com os resultados das simulações numéricas verifica-se que com o aumento da área (espessura), a corrente de curto-circuito aumenta (diminui) e a tensão de circuito aberto aumenta (diminui). A resistência ótima diminui (aumenta) e a potência máxima aumenta

(diminui) com o aumento da área (espessura). A maioria destes resultados estão de acordo com modelo teórico e foram encontradas razões para a diferença dos resultados na tensão de circuito aberto e o modelo teórico. No estudo da permitividade relativa foi feita uma comparação entre um material dopado com nanopartículas e outro sem as partículas, mas com um valor de permitividade relativa equivalente. Ambos os casos da comparação estão de acordo nos resultados da tensão de circuito aberto e da corrente de curto-circuito e foi feita uma correção de carga que relacionava a densidade de superfície de carga com a permitividade equivalente para compreender melhor a relação entre ambas.

No estudo da variação da temperatura usou-se amostras de PDMS com vários valores de espessura e uma amostra de PDMS dopada com nanopartículas, feita com um método de fabrico desenvolvido no decorrer deste trabalho. Estas eram as amostras fixas, enquanto as amostras que faziam o contacto eram de alumínio ou cobre. Neste estudo verificou-se que com o aumento da temperatura, a tensão de circuito aberto e a corrente de curto-circuito diminuíam.

Este trabalho ajudou em ter uma melhor perceção de como os TENGs são afetados pela variação das suas propriedades e temperatura. Como trabalho futuro, os seguintes pontos serão os passos seguintes deste trabalho: aumentar a temperatura de execução da experiência e encontrar maneiras e compreender melhor o que faz diminuir a deterioração dos materiais com a temperatura, melhorar o processo de dopagem de materiais com nanopartículas e explorar mais as tendências inesperadas da tensão de circuito aberto para a área e a espessura.

Contents

List of Figures

This thesis is dedicated to my family and close friends for their love and support during my journey of highs and lows in physics and physics engineering courses.

I would like to emphasise my grandfather, Helder Santos, for encouraging me to study throughout my life. Without realising it, I enrolled in a course associated with the area that he would have pursued if he had continued his studies past the fourth class.

Chapter 1

Introduction

The triboelectric nanogenerator (TENG) is a promising environmentally friendly energy harvester being developed that is able to convert mechanical energy to electrical energy [1]. The demand for environmentally friendly energy harvesters has been gigantic over the years because of extreme weather events, such as the recent extreme water drought throughout Europe in 2022 [2], the increase in global temperature by 1.5°C post pre-industrial era [3] and high emissions of CO_2 and other gases, which is still rising [4]. All of these factors contribute to the worsening global climate crisis, and to minimise the growth of this crisis, the investment in developing energy harvesters capable of replacing energy coming from fossil fuels has increased in recent years, aiming to reduce emissions and salvage the Earth from a possible worse future [3].

The main objective of this thesis is to better understand how one can enhance TENG performance. The thesis is divided in two parts. In the first part, we perform a numerical study using COMSOL on how the area, thickness and relative permittivity of the TENG materials influence the corresponding outputs. In the second part, an experimental setup is used to investigate the influence of temperature on the TENGs for a variety of materials (such as PDMS and $SrTiO_3$ doped PDMS).

After a brief overview of energy harvesters in this chapter, chapter 2 is dedicated to the triboelectric effect, the triboelectric nanogenerators, materials and properties that affect the performance of the TENG. In chapter 3, it is explained the numerical procedures used for the simulations on COMSOL and the experimental procedures for the physical experiment with temperature. The following chapters present the results of the numerical simulations and the physical experiment.

We begin with a quick overview of the main energy harvesters currently available in order to situate TENGs in the energy harvesting field.

1.1 Energy harvesting

Energy harvesting consists in capturing and converting the energy coming from the environment to electrical energy. The importance of this method to obtain energy is astonishing. An example of the utility of energy harvesters are devices in remote or hard to reach areas. An energy harvester like a solar panel can be used instead of a battery to power sensors or actuators, reducing the need of maintenance and contributing to a reduction in pollution by battery waist [5, 6]. Energy harvesting systems allow to extend the life time of devices, being also low cost and environmental friendly [6].

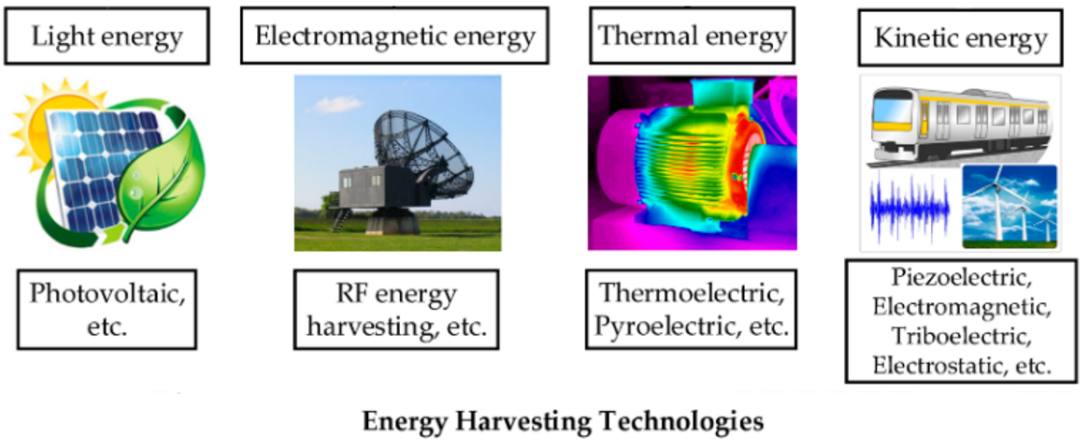

FIGURE 1.1: Main types of energy and harvesting technologies that can supply energy. (Adapted from Ref. [7].)

There are many ways to harvest energy from environmental sources, such as electromagnetic, thermal or mechanical energy (Fig. 1.1). Each of them is a vast world on its own with a lot of research. Here, a very brief overview of various technologies is provided to offer an idea of the current status of energy harvesting devices.

Harvesting light energy coming from the sun is accomplished with photovoltaic panels by converting electromagnetic energy to electrical energy [5]. Photovoltaic panels are widely used around the world and the installation of this technology, in terms of power, is increasing year by year [8]. There are various types of solar cells, all in the pursuit to maximise the energy efficiency while being low cost. Despite mono-crystal and poly-crystal

silicon solar cells being cheaper and the most widely used solar cells due to the optimisation process along the years, there are other solar cells that are more efficient. Some of them are still being developed in laboratories.

The perovskite solar cells are an example. The efficiency of these cells obtained in laboratory was around 22.1%, which is comparable with the efficiency of the mono-crystal and poly-crystal silicon cells. Despite the fact that there are still issues with perovskite solar cells, it is a promising technology because new methods of boosting their efficiency are being discovered and there is a chance for commercialization in the future [9].

The broadcasting and communications industries use radio waves frequently, so, it is being thought about how to effectively convert radio wave frequencies to electrical energy. The power of these emitted waves is in the 0.2 nW/cm^2 to 1 $\mu W/cm^2$ range [10]. Despite being a modest amount, the emitted power can increase as communication and broadcasting technologies advance. Radio frequency (RF) waves are continuously emitted by the respective sources, which means that the energy captured is roughly constant throughout the day. The fact that RF energy is not much affected by temperature or weather is another significant benefit, which justifies the usage of RF waves in broadcasting [10, 11]. There are many types of sources that release RF waves. Some of them are FM (87.5 MHz to 108 MHz), TV broadcasting (41 MHz to 250 MHz and 470 MHz to 950 MHz) and WiFi (2.45 GHz to 5 GHz) [11]. Research was done to determine how to harvest these waves and how harvesting efficiency varies with distance. The main conclusions were that the obtained power can differ substantially between RF harvesters prototypes and frequencies. Between 2 and 10 Km the power drops 1 or even 2 order of magnitudes, with the peak of power being around the µW. Although further research is still needed, it has the potential to provide energy to gadgets with low energy usage [10, 11].

To harvest thermal energy, thermoelectric and pyroelectrics generators are two areas of interest. Thermoelectric generators aim to use the wasted heat by a source linked to automobiles, aerospace, marine industry, for example, to produce energy. The simplicity, low maintenance and low cost are the advantages of these devices [12]. The usage of these devices at low temperatures is possible as coolers, since studies have proven a higher efficiency at lower temperatures than at room temperature [13]. The concept of operation of the thermoelectric relies on spatial thermal gradients and convert heat flows into electrical energy. Nowadays, a thermoelectric generator can produce between µW and mW [14].

The pyroelectrics generators also convert heat into electrical energy. However, they use fluctuations on the temperature over time that can be seen as a temporal, rather than the spatial, gradient. This is useful for micro generators and thermal sensors smaller than the spatial gradient. An example of an application is the use of a pyroelectric nanogenerators to power a self-respiratory system. This is done by using the gradients of temperature between the environment and human body temperatures as source of energy production [15].

To harvest kinetic energy, there are solutions, such as piezoelectric generators, electromagnetic and triboelectric.

Piezoelectric generators convert mechanical into electrical energy by bending, squeezing or stretching the piezoelectric material [5, 11, 16]. Applications for piezoelectric generator are varied, including sensors that are self powered by environmental vibrations or from human motion for health monitoring. A more specific application, despite still being developed, is monitoring human organs [5, 17].

Electromagnetic generators produce energy by the relative movement of a coil and a magnet. An electromotive force results from a variation of magnetic flux induced from a magnetic coil and a source of magnetic source that is a permanent magnet [6, 11].

Finally, there is also the TENG that it will be discussed in detail in the next chapter.

Chapter 2

Triboelectric nanogenerators

Understanding the triboelectric effect and the charge transfer mechanisms that make the TENG function is crucial before describing how the TENG works.

2.1 The triboelectric effect

The triboelectric effect, which has been known to exist for hundreds of years, occurs when two materials come into contact or rub against one another, creating electrostatic charges. In more detail, when two different surfaces come into contact, a chemical bond is formed between some regions of the two surfaces [1], causing charges on the surfaces to transfer to the other one in order to equalise the electrochemical potential between the surfaces [1]. These charges can be electrons, ions or pieces of nano-sized material. When the surfaces are separated, charge equilibrium is broken. Thus, there is going to be negative charges accumulated on one surface and positive charges on the other. This creates a potential difference between the surfaces, resulting in electrostatic energy [1, 18, 19]. The electrical conductivity of a material has an influence on how long it can hold charges on a surface. The more electrically insulating the material is, the longer it can hold the charge that it accumulates [1]. Triboelectric effect can be bothersome for safety reasons. For example, in aircraft, electrostatic charge accumulates because of air friction, interfering with the radio frequencies used in communication with the aircraft. However, the triboelectric effect can also be provoked on purpose to harvest energy by using a TENG [1, 18].

2.1.1 Charge mechanism transfer of the triboelectric effect

As was previously mentioned, the triboelectric effect is made possible by three different kinds of charge holders (electrons, ions and nano-material). We will now revised each of these possibilities.

2.1.1.1 Electron charge transfer

Electrons are the main charge transfer particles in solid-solid contact electrification. It is possible to determine the work function on the surface of the material, indicating the energy needed to remove one electron by photoemission spectroscopy [20, 21].

When two surfaces come into contact, electron-hole pairs form near the Fermi surface, promoting the flow of electrons from the lowest work function surface to the highest work function to reach an equilibrium state. When both surfaces are separated, electrons flow in the reverse direction through tunnelling effect due to a gap appearing between the materials to reach an equilibrium with the material and electrode. This equilibrium is harder to reach because, as the distance between materials increases, the electron transfer through tunnelling exponentially diminishes. From experiments made with the metal-dielectric triboelectric pairs, the surface charge density σ, and the work function can be related to each other using the Poisson equation [19, 20]:

$$\sigma = \alpha\varepsilon \left(\frac{\Phi_M - \Phi_I}{\lambda} \right), \tag{2.1}$$

where Φ_M is the electrostatic potential for the metal, and Φ_I is electrostatic potential for the dielectric, ε is the dielectric constant of the material, λ is the penetration depth, and α is the leading factor with a value of 1.77×10^{-13} for the pair metal-dielectric [20].

2.1.1.2 Ion charge transfer

Ion transfer is also an important charge transfer mechanism in the triboelectric effect. On a triboelectric material surface, there are strongly and loosely bonded ions. Weaker bond ions can then be transferred when contact occurs with another material's surface, so that charge of the same sign as the strong bond ions can be accumulated in the newly transferred surface [19, 20].

Studies have proven that humidity has an influence on the charge density variation when a sample is in a controlled environment [19]. The amount of humidity or water

vapour can act as a donor or acceptor to motivate the charge density variation by supplying ions to the surfaces of the materials, even if the materials used cannot contribute with mobile ions [19].

2.1.1.3 Charge transfer with nano-material

The strain of rubbing and pressing two materials together causes small portions of the materials to adhere to the opposite surface. The energy barrier for particle transference shrinks as the amount of strain applied increases, allowing nanosized particles to pass through from one material to the other [20].

There are two parameters to take into account as this transfer wears both materials down. These parameters are the chemical wear and the physical load stress that can be seen in the next equation [20]:

$$\Gamma = \Gamma_0 \times \exp\left(-\frac{\Delta U_{act}}{K_B T}\right) \times \exp\left(\frac{\sigma_N \Delta V_{act}}{K_B T}\right), \tag{2.2}$$

where the ΔV_{act} is the effective activation volume, and σ_N is the normal load stress and the adhesive force to the other material. Γ is the wear rate of the material, k_B is the Boltzmann constant, T is the temperature, Γ_0 is the effective attempt frequency, and the ΔU_{act} is the internal free energy of activation by chemical processes [20].

In Eq. (2.2), the exponential on the left is related to chemical wear due to rubbing and the one on the right is related to normal load stress. These two parameters provide the tribological contribution to the material removal process and the first one, the chemical wear is negligible for contact-separation triboelectric effect [20].

2.2 Triboelectric nanogenerators

Triboelectric nanogenerators (TENGs) are a recent technology compared to the triboelectric effect that is known for more than a thousand years. They were first conceived in 2012 by the group Z. L. Wang [18].

2.2.1 Operations modes

There are four operation modes for TENGs (Fig. 2.1): contact-separation, sliding, single electrode, and free standing modes. The contact-separation mode is the focus of this work and it will be discussed in detail next.

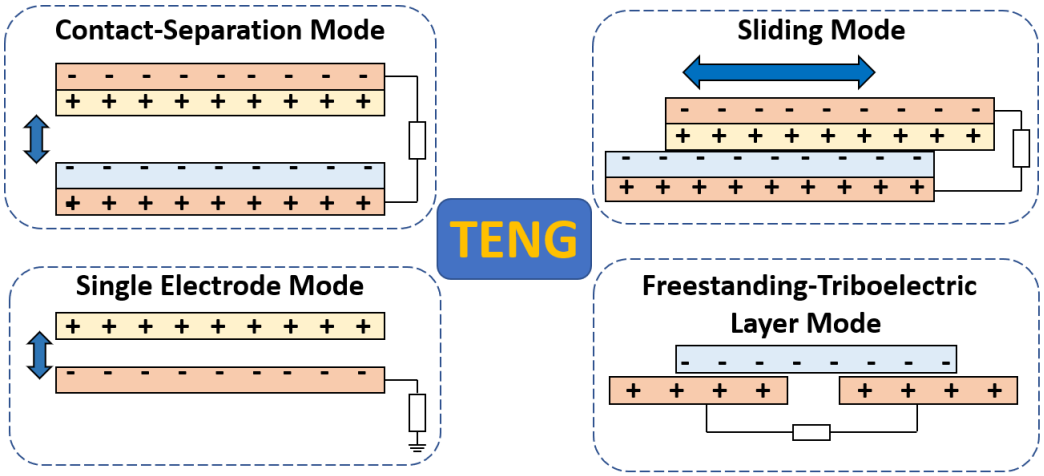

FIGURE 2.1: The four types of TENGs. The single electrode mode is in the contact-separation mode version, and the freestanding triboelectric layer mode is in the sliding mode version. The triboelectric materials are represented in light blue and light yellow, and the electrodes in orange.

The sliding mode TENG consists of one material sliding against a fixed material, varying the quantity of surface in contact throughout the work cycle. By operating this way, charges circulate between electrodes by asymmetry of charge between the parts of the materials that are in contact and the parts that are not in contact, producing a current to compensate for that charge difference, leading toward electrostatic equilibrium. This TENG has a disadvantage compared to the contact-separation mode TENG because of the increased material wear [1, 22].

The single electrode TENG, also known as SETENG, is a simpler version of the contact-separation and sliding mode TENGs. The difference between the previous modes is that only one electrode exists that is fixed and connected to the ground, meaning there is only one triboelectric material that moves. This type is useful for cases where the electrode needs to be fixed and the material on the other side needs more freedom to accommodate the irregularities of the contact more easily to minimise the loss from energy harvested. The SETENG can be conceived in the contact-separation or in the sliding mode [1, 22, 23].

Both the sliding and single electrode TENGs, can have a metal-dielectric or a dielectric-dielectric configuration.

The freestanding-triboelectric layer mode, like the single electrode, can be conceived to operate in the contact-separation or in sliding modes. This type of TENG, as the name implies, has a layer with movement freedom. In the contact-separation mode version, there is a layer in the middle of two materials and it is this layer that moves between these two materials. The top and bottom electrodes and materials are fixed in position. In the

freestanding-triboelectric layer sliding mode, the electrodes are fixed and the triboelectric material slides laterally between both electrodes. The freestanding sliding mode has less wear, less heat production from friction and a higher energy efficiency than the sliding mode, making it more viable for applications [22, 24].

2.2.1.1 The contact-separation mode TENG

To explain the process behind the contact-separation mode TENG, Fig. 2.2 represents the complete cycle of this TENG. The TENG device is composed by two triboelectric materials (usually dielectrics) with opposite charge tendencies and two electrodes. One triboelectric material is fixed, while the other moves back and forth. At the beginning of the process [Fig. 2.2(a)], with the dielectrics separated, no charge is present on their surface, remaining in equilibrium with the electrode [25, 26]. When coming into contact, a charge transfer process occurs between the triboelectric materials to bring their Fermi levels of both dielectrics to the same energy [Fig. 2.2(b)]. This will cause one material to have a negative surface charge and the opposite material to have an equal positive value. Consequently, the electrodes are forced to have a neutral charge to respect the charge equilibrium of the dielectrics [25, 26].

When both surfaces are separated, the charges remain on the triboelectric materials, meaning that the electrodes need to have the opposite value of charge to achieve electrostatic equilibrium [Figs. 2.2(c),(d)]. If the triboelectric material has a positive surface charge density, the electrode must match the same value but with the opposite amount

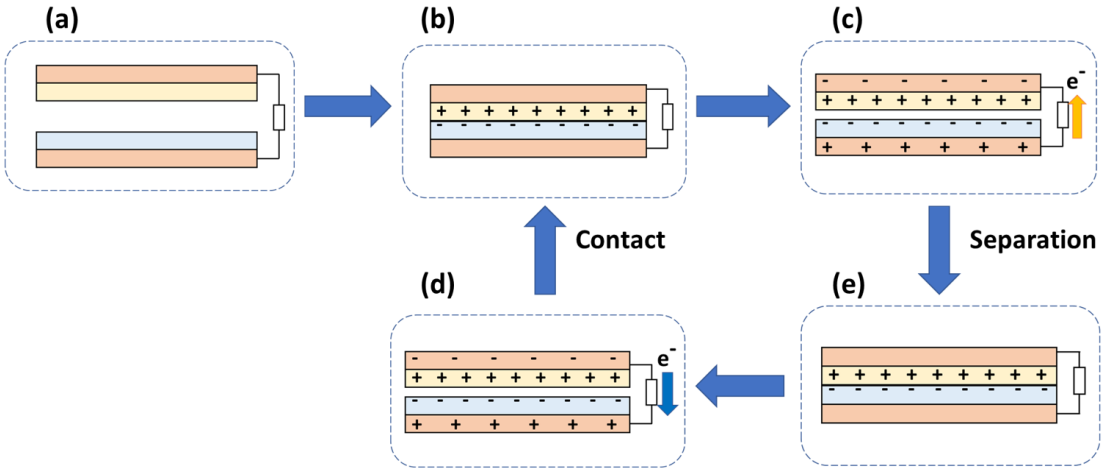

FIGURE 2.2: The working principle of the contact mode TENG dielectric-dielectric type. The triboelectric materials are represented by light blue and light yellow colors and the electrodes by an orange color.

and vice-versa. This is made possible by electrons flowing from the electrode of the negative triboelectric material to the other electrode, leaving one electrode positively and the other negatively charged [25, 26].

During the approximation motion between triboelectric materials, the charges on both surfaces induce movement of free electrons through an external circuit [Fig. 2.2(e)]. This occurs due to electrostatic induction because of the electrical potential difference, with the charges in the electrodes moving towards a charge equilibrium [25, 26].

Contrary to the dielectric-dielectric case, explained previously [Fig. 2.3(a)], in the metal-dielectric case, one of the electrodes acts as an electrode and also as the contact material, meaning it is in equilibrium with itself when the metal and dielectric are further apart and with the dielectric when they are in contact [Fig. 2.3(b)] [25, 26].

Thus, in the contact-separation cycle, the voltage and the current through the external circuit will display a minimum and a maximum value. The minimum corresponds to the contact phase of the cycle, while the maximum corresponds to the separation from the material in contact (Fig. 2.4).

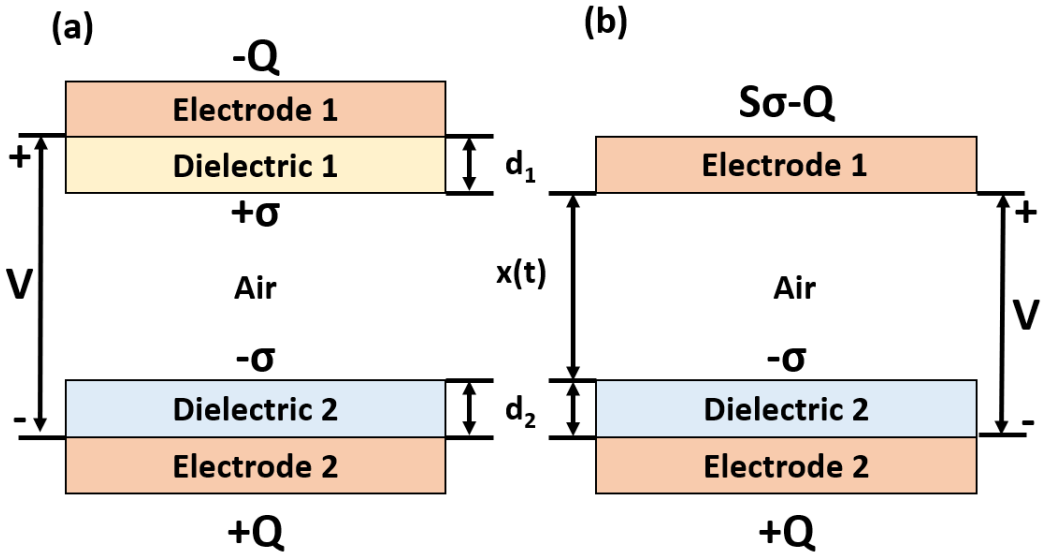

FIGURE 2.3: The scheme of the contact mode TENG with the two variants: **(a)** is the dielectric-dielectric and **(b)** the metal-dielectric types. In the materials, the surface charge density is σ, while in the electrodes, the charge is represented by Q or $S\sigma - Q$ in the metal-dielectric case for one of the electrodes. S is the area of the triboelectric material. (Adapted from Ref. [27].)

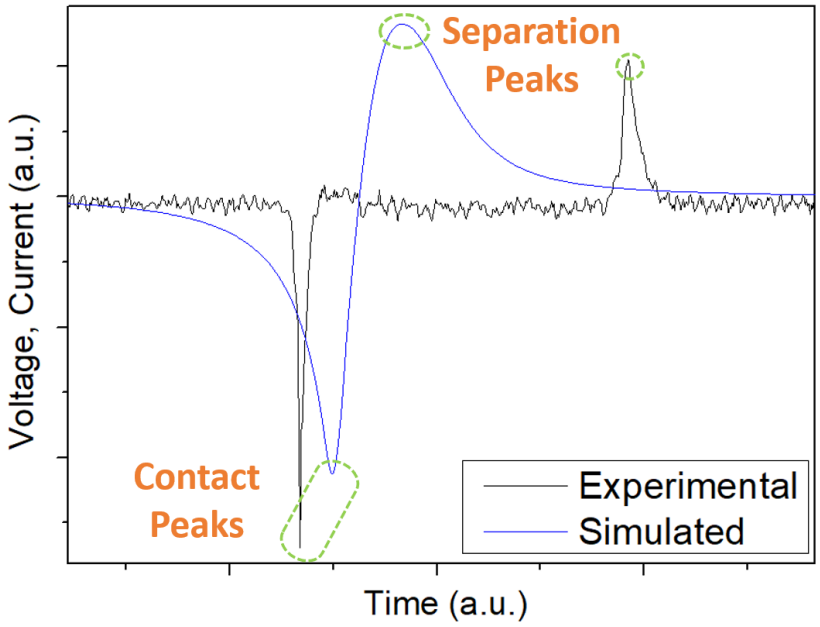

FIGURE 2.4: Simulated and measured peaks of current or voltage as a function of time for the contact-separation TENG.

To arrive at the equations explaining in depth the mechanisms behind the contact-separation mode TENG, Fig. 2.2 allows one to derive the V-Q-x relation through electrodynamics. Let us consider the model developed by Niu *et al.*[27], which sees the contact-separation mode TENG as a double-plate capacitor, implying that the area of electrodes and dielectrics is much larger than the thicknesses of both dielectrics and the distance between them. This assumption leads to two facts. One is that the charges in the electrode will be distributed in a uniform way and the other is that the electric field will be perpendicular to the electrodes and insulators [27].

So, with the Gauss theorem, the electrical field inside each material will have the expression:

$$E = -\frac{Q}{S\varepsilon_0\varepsilon_r}, \tag{2.3}$$

with Q being the charge in the electrodes, S the area of the TENG, and ε_r the relative permittivity of the dielectric. Between the dielectric, the electric field is:

$$E = \frac{-\frac{Q}{S} + \sigma(t)}{\varepsilon_0}, \tag{2.4}$$

with σ being the surface charge density and t the time variable. To achieve the voltage between the two electrodes, it is necessary to know the distance between the materials (x), and thickness of the materials (d_1, d_2) and the corresponding electrical field (E_1, E_2, E_{air}):

$$V = E_1 d_1 + E_2 d_2 + E_{air} x. \tag{2.5}$$

Substituting Eqs. (2.3) and (2.4) in Eq. (2.5) gives:

$$V = -\frac{Q}{S\varepsilon_0}\left(d_0 + x(t)\right) + \frac{\sigma x(t)}{\varepsilon_0}, \tag{2.6}$$

where $x(t)$ is the distance between triboelectric materials that vary over time, $d_0 = \sum_i \frac{d_i}{\varepsilon_{r_i}}$ in which d_i is the thickness of the material and ε_{r_i} the relative permittivity of the material. The extent of the sum in d_0 depends on how many dielectrics exist on the TENG. If it is a dielectric-dielectric case, d_0 has two components, while in the metal-dielectric case, d_0 only has one component. So for the dielectric-dielectric case, Eq. (2.6) can be written as [27]:

$$V = -\frac{Q}{S\varepsilon_0}\left(\frac{d_1}{\varepsilon_{r_1}} + \frac{d_2}{\varepsilon_{r_2}} + x(t)\right) + \frac{\sigma x(t)}{\varepsilon_0}, \tag{2.7}$$

and the V-Q-x relation has been obtained. With the metal-dielectric case, the maximum capacitance can be calculated when both materials touch [25]:

$$C_{max} = \frac{\varepsilon_0 \varepsilon_r S}{d_{dielectric}}, \tag{2.8}$$

where $d_{dielectric}$ is the thickness of the dielectric. To arrive at the dielectric-dielectric case, two capacitors in series can be considered to obtain the maximum capacitance.

2.3 Regions of operation of the TENG

The TENG harvests energy from an external source and delivers it into a load resistance. Since the TENG can be modelled as a parallel plate capacitor, the equivalent circuit as a whole is similar to the RC circuit (Fig. 2.5). Modifying Eq. (2.7) to substitute with $V = RI$ gives:

$$R\frac{dQ}{dt} = -\frac{Q}{S\varepsilon_0}\left(d_0 + x(t)\right) + \frac{\sigma x(t)}{\varepsilon_0}. \tag{2.9}$$

The load resistance, thus influences the values of the generated voltage, current, and power, with three possible regions emerging (Fig. 2.6).

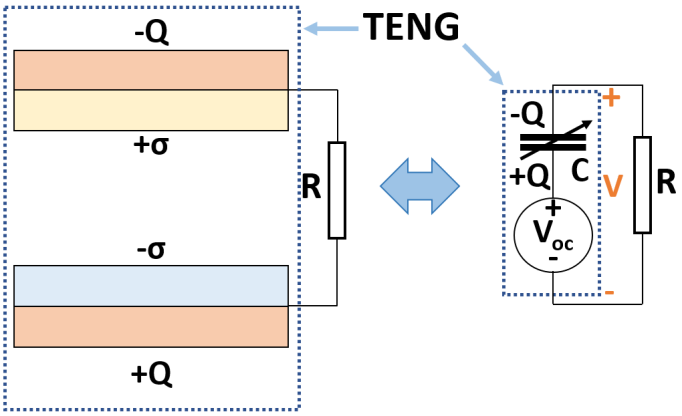

FIGURE 2.5: Representation of a TENG and how it can be modelled into a circuit. (Adapted from Ref. [22].)

The first region in Fig. 2.6 represents the results when the resistance is very low. It is a short-circuit case, meaning that the voltage is zero and the short-circuit current (I_{SC}) is determined by differentiating over time the short circuit charge transfer between electrodes:

$$Q_{SC} = \frac{S\sigma x(t)}{d_0 + x(t)}. \tag{2.10}$$

Differentiating over time Eq. (2.10) gives:

$$I_{SC} = \frac{S\sigma v(t) d_0}{(d_0 + x(t))^2}. \tag{2.11}$$

The third region represents the case when the resistance is very high and there is no charge transfer between the electrodes, leading to Q being zero [27]. Applying the previous statement to Eq. (2.7) gives the open circuit voltage (V_{OC}):

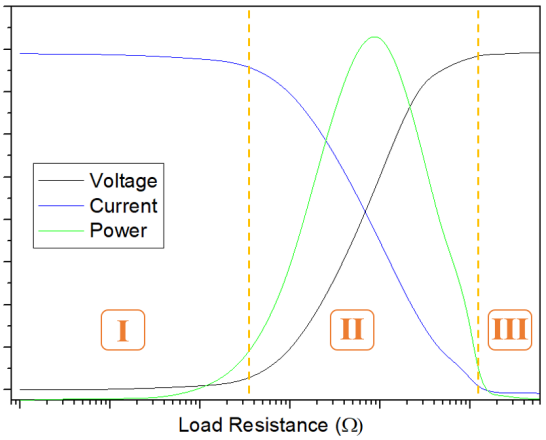

FIGURE 2.6: Conceptual graph showing the voltage, current, and power together on one graph to represent the expected outcome for a contact mode TENG. This graph can be divided into three sections.

$$V_{OC} = \frac{\sigma x(t)}{\varepsilon_0}. \tag{2.12}$$

Region two is the transition region where the voltage increases and the current decreases. At the crossing point between the voltage and current, the peak of the power output occurs. The power peak resistance is called the optimum resistance that can be approximated to [27]:

$$R_{opt} \approx \frac{(d_0 + x_{max})^2}{S v \varepsilon_0}. \tag{2.13}$$

Besides these three regions, there is an effect called the transient state that depends on the external resistance connected to the TENG [28]. This effect affects the response of the charge circulation, introducing a delay. The transient state is always present in all of the TENG modes and occurs when the maximum distance and the contact are made because in the previous phases of the cycle of the TENG, charge is flowing slowly, delaying the equilibrium of charge in the following phase [28, 29].

Let us consider a complete contact-separation cycle in this case. Under a low resistance, the voltage and current peaks occur at the same time of the contact. However, with increasing load resistance, the peaks occur with a delay that increases with the resistance until the open circuit case is reached, where the charge in the electrodes is zero, meaning that the voltage is described by the V_{OC} equation [Eq. (2.12)]. This implies that the maximum occurs at the maximum distance between materials [29].

This effect is more noticeable at higher resistances, way past the peak of power, and also affects how fast the decay of the voltage and current occurs after a peak [28, 29].

2.4 Materials and charge tendency

The materials used to generate the triboelectric effect can, depending on their charge tendency, turn their surface electrically positive or negative, with the charge transfer mechanisms mentioned previously. To maximise the triboelectric effect, in the dielectric-dielectric case, the ideal is to have two materials that have a strong opposite charge tendency to maximise the charge difference between surfaces. In Fig. 2.7, the charge tendency of selected materials is represented, with some materials present in this work, such as nylon, polytetrafluoroethylene (PTFE), and polydimethylsiloxane (PDMS).

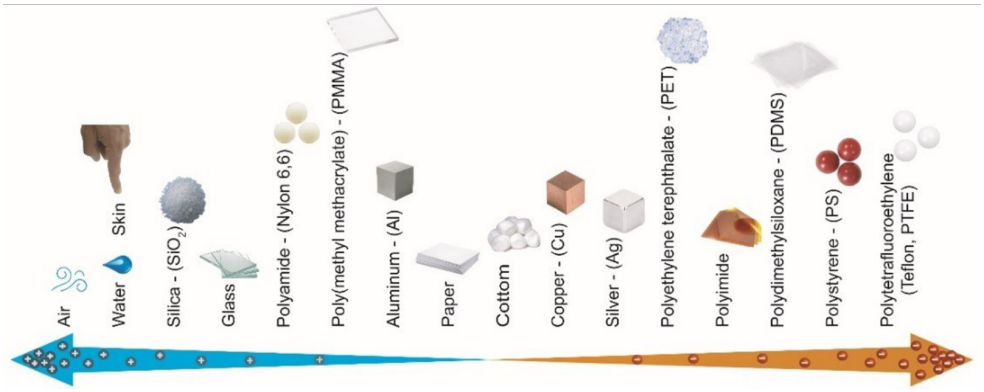

FIGURE 2.7: Charge tendency of selected materials. The blue arrow represents the positive charge tendency and the red arrow represents the negative charge tendency. (Adapted from Ref. [30].)

In terms of charge tendency, nylon has one of the strongest tendencies to become positively charged, while PTFE has the opposite tendency. PDMS has a tendency to become negative, but it is not as strong as PTFE. However, PDMS is an interesting material because it is easy to manufacture, cheap, flexible, non-toxic, and easy to control its air pore size and dope with nanoparticles to enhance its performance [31, 32]. Hence, it is widely used. Despite the order of materials listed here being true for most cases, there are some exceptions.

One of them is the cyclic triboelectric series that an example is given in Fig. 2.8. Each material inside the cycle can become negatively or positively charged towards specific materials that a cycle is formed with a set of materials. For example, silk is positively charged towards paper that is negatively charged. However, silk becomes negatively charged towards Zinc that is positively charged [20].

FIGURE 2.8: Cyclic triboelectric series example. (Image taken from Ref. [20].)

Another mechanism case is the use of two identical materials in TENGs. This should not be possible at first glance, but there are materials that make it possible to perform this reproducibly [20]. In this case, asymmetric contact leads to a non-equilibrium of charges in the surfaces and the probability to occur charge transfer is proportional to the charge surface density difference. Thus, if different areas of the same material come into contact, a charging process can occur. Hence, the areas and roughness of the surfaces of the materials are important for this effect [20].

2.5 Electrical permittivity and polarisation

A material is composed of atoms and molecules that can be polar or nonpolar. If this material is placed in an electric field, each molecule will have a dipole moment ($\mathbf{p} = Q\mathbf{d}$, where Q is the charge and $\mathbf{d}$ the distance between charges) that will point toward the direction of the electric field, concluding that the material has a polarisation. The sum of the dipole moments in a unit volume is the definition of polarisation. To relate the polarisation to the relative permittivity, the displacement field is defined by [33, 34]:

$$\mathbf{D} = \varepsilon_0 \mathbf{E} + \mathbf{P}, \tag{2.14}$$

where $\mathbf{P}$ is the polarisation and $\mathbf{E}$ the electrical field. Knowing that the polarisation can be defined by [33]:

$$\mathbf{P} = \varepsilon_0 \chi_e \mathbf{E}, \tag{2.15}$$

where χ_e is the electrical susceptibility that can be related to the relative permittivity by [34]:

$$\varepsilon_r = \frac{\varepsilon}{\varepsilon_0} = 1 + \chi_e, \tag{2.16}$$

where ε is the electrical permittivity of the material. Using Eq. (2.16) on Eq. (2.15), one obtains:

$$\mathbf{P} = \varepsilon_0 (\varepsilon_r - 1)\mathbf{E}. \tag{2.17}$$

One thus concludes that the polarisation is directly proportional to the electrical field and that increasing the polarisation increases the relative permittivity and vice-versa. The surface charge density can be related to the relative permittivity [35]:

$$\sigma = \frac{Q}{S} = \varepsilon_0 \varepsilon_r \mathbf{E}. \tag{2.18}$$

In conclusion, the surface charge density, the polarisation, the electrical field, and the relative permittivity are all related to each other. This is important for the TENG performance because it will have an indirect impact on the final result.

2.6 Bulk methods for TENG performance improvement

There are other alternatives to improve TENG performance besides varying the area, thickness, maximum distance, speed of the moving layer or load stress directly. These alternatives include changing the surface of the material chemically, ion injection, dipole moment control or surface morphology control [26, 36]. Here we will focus on bulk methods that change the triboelectric material bulk constitution by controlling the size of air pores inside or by doping with nano or microparticles. Both bulk methods can be combined together for further optimisation.

A common aspect that both methods alter is the effective relative permittivity ($\varepsilon_{r_{eff}}$) of the material. This parameter not only takes into consideration the main material but also the other components altered or added to the material, such as the size of the pore or nanoparticles. The equation for this parameter is [25]:

$$\varepsilon_{r_{eff}} = \varepsilon_{r_a} f_a + \varepsilon_{r_b} f_b, \tag{2.19}$$

where ε_{r_a} and ε_{r_b} are the relative permittivities of the main material and nanoparticles or air pores, and f_a and f_b are the fractions of concentration of the main material and air pores or nanoparticles.

The main point here is to understand the physics of the doping of nanoparticles and the control of air pores. What are the reasons for the improvement in performance with nanoparticles or with air pore size control? Is there a limit in the concentration where the performance starts to decrease and why?

Combining both air pore control and adding nanoparticles can yield the best results at the optimal concentration of both parameters. We will see how each method increases the performance of the material.

2.6.1 Controlling the size of the air pore

Controlling the size of the air pores can be seen as an increase in the concentration of air inside the material. At first glance, it decreases the effective relative permittivity, which, according to the V-Q-x relation presented in Eq. (2.7), translates into an increase in the generated voltage. However, in terms of the TENG as a capacitor, in theory, with a constant thickness, the overall performance of the TENG should be lower. That is not the case because the increase in air pores turns the PDMS more compressible when it collides with another material [25]. This leads to the thickness of the compressed PDMS decreasing, and the increase in the size of the pores will help to increase the contact surface area with the opposing material due to the ease of compressing, which aids the adjustment to the opposing material [25]. The increase in contact area also increases the charge transfer between materials [25]. Decreasing the thickness and increasing the area, raises the overall performance of the contact-separation TENG, since the maximum capacity increases, completely outweighing the decrease in the relative permittivity.

However, increasing in the size of the pore beyond the optimum value can lead to an even lower effective relative permittivity and the contact area starts not to be consistent because the pores are large enough for the PDMS to have consistency in covering the whole area of the opposing material [25]. The tendencies explained previously can be observed in Fig. 2.9(b).

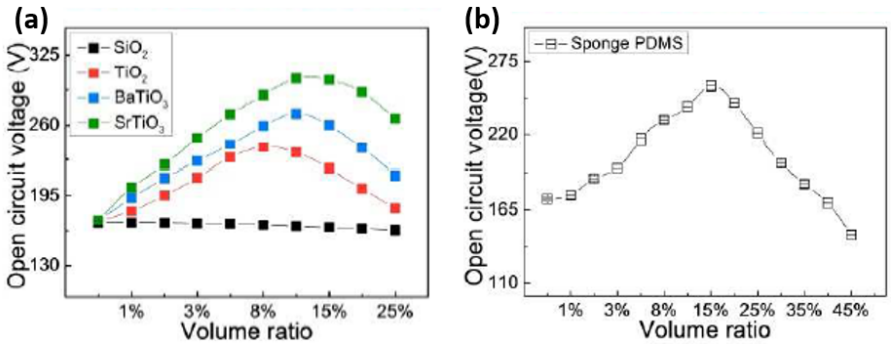

FIGURE 2.9: **(a)** V_{OC} of PDMS samples as a function of the concentration of nanoparticles. **(b)** Concentration of air with pore size control. The results for the I_{SC} and charge transfer have a similar tendency. (Taken from Ref. [25].)

Methods that can lead to the formation and control of air pores inside PDMS use deionised water [37], NaCl [25, 38], or sugar [39, 40]. If NaCl and sugar are used, the quantity and grain size are important to vary the pore size [25, 38, 40]. Either of them is mixed with the PDMS and are removed after the curing by submersing the films into a stirred water bath and dried. If deionised water is used instead, only the dried up process is needed [37].

2.6.2 Nanoparticle doping

Doping with nanoparticles causes an increase in the internal polarisation that increases the effective relative permittivity, leading to a rise in the surface charge density and improving the charge induction on the electrode [41]. According to the double parallel plate capacitor modelled by the Gauss law, if one medium increases the effective relative permittivity, the total capacitance of the TENG rises [25]. The ideal situation is to use nanoparticles with the highest possible relative permittivity to maximise the effective relative permittivity of triboelectric material for the maximum possible enhancement to be achieved.

However, the available literature [25, 41, 42] shows that the results have a peak of performance and increasing the concentration of nanoparticles past that value leads to a drop in the performance of the TENG [Fig. 2.9(a)]. The reasons will be listed below.

Firstly, there is a limit to the concentration of nanoparticles that, once exceeded, will result in the surface of the triboelectric material being overfilled with nanoparticles, reducing the contact area and the surface charge density transferred, outweighing the effective relative permittivity increase [25].

The previous effect is also affected by nanoparticles size. Smaller nanoparticles lead to the performance peak being increased and also enables the surface to have a higher quantity of nanoparticles before the contact area starts to decrease [25].

The third reason is related with the agglomeration of nanoparticles as the dispersion is not perfect [25].

Furthermore, the agglomerations of nanoparticles can cause current leakages between both electrodes, reducing the triboelectric effect [41]. Beyond the performance peak of the TENG, the increase in concentration of the nanoparticles leads to an increased agglomeration of nanoparticles, increasing the leakage current.

There are interesting nanoparticles to use, such as $SrTiO_3$ [25], $BaTiO_3$ [37, 43] and $CaCu_3Ti_4O_{12}$ (CCTO) [41, 44]. Since PDMS has a high viscosity, a mixer is needed to disperse nanoparticles [37], or alternatively, a solvent could be used to disperse nanoparticles by using magnetic steering.

2.7 Environmental factors

Environmental factors, such as temperature, humidity, acidity, contact force, and air pressure, have an impact on the TENG's performance. The effect of temperature on TENGs will be described in detail in this section, while the effects of humidity, contact force and air pressure on the TENG performance will be briefly discussed.

2.7.1 Temperature

The effect of temperature on TENG can be researched with both samples at the same temperature or at different temperatures. Studies in the latter case search for the ideal temperature gradient between both samples while maintaining one sample at a stable temperature with a cooling device to maximise the performance. The increase of the temperature gradient makes the hotter sample have a larger tendency to release electrons, becoming more positive, while the cooler sample will have to neutralise with the opposing charge when they touch, becoming more negative [45, 46]. This boosts the charge transfer between samples. Hence, the V_{OC} and I_{SC} increase. A surface state model was developed to explain the behaviour of the charges on the materials at different temperatures [45]. Optimal gradient temperatures between samples were of around 145 K, with one sample at room temperature [46].

When both materials are at the same temperature and the temperature increases, there is typically a decrease in performance. The reason for this is the thermionic effect. Due to the increase in temperature, electrons become more energised and are able to overcome the work function and be released from the material, leading to a larger emission of electrons and also a lower charge storage capacity on the material [47–49]. This motivates an increase in the backward mechanism of charge transfer, which is affected by thermal fluctuations in the environment [50, 51]. For a better understanding, let us consider nylon and PTFE. Nylon has a strong tendency to turn positive, and PTFE has a strong tendency to turn negative. The obvious charge transfer (forward) is that nylon releases electrons for

PTFE to capture them when contact occurs [50–52]. However, with the increase in temperature, the release of electrons increases and motivates the rise of the backward charge transfer from PTFE to nylon, which competes with the forward charge transfer, leading to a decrease in V_{OC} and I_{SC} of the TENG [47, 51, 52].

The occurrences in the charge transfer process as temperature rises are explained by two models. The first is the surface state model that can be applied to metal-dielectric cases and some dielectric-dielectric cases [47–49]. The second model is the cloud well potential that covers materials with a crystal structure that is not well defined [47, 48, 53].

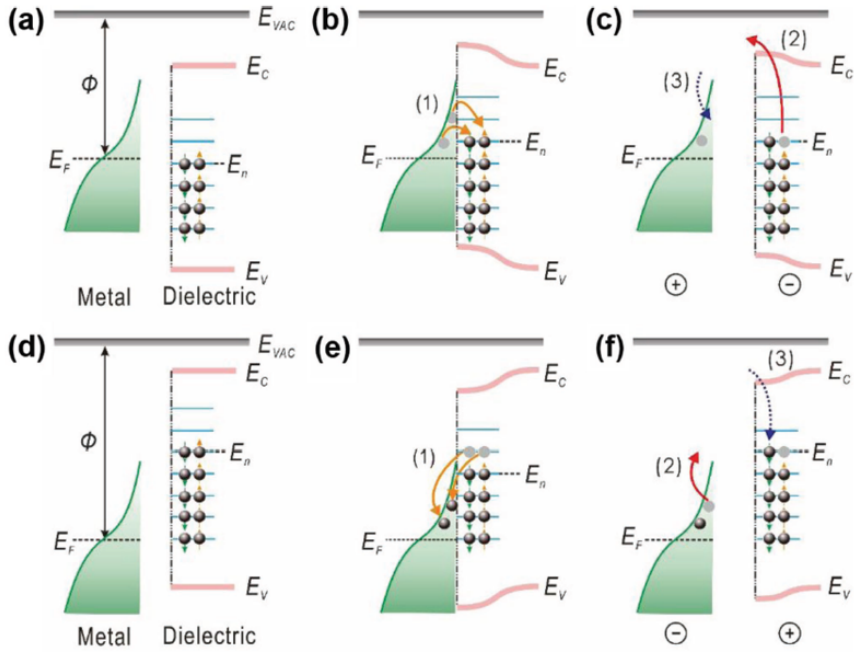

FIGURE 2.10: Illustrations of the surface state model for metal-dielectric case before contact **(a)**,**(d)**, during contact **(b)**,**(e)** and after contact **(c)**,**(f)** for the cases where the metal has a positive charge tendency and the dielectric a negative charge tendency (**(a)-(c)**) and the opposite case (**(d)-(f)**). (Adapted from Ref. [48].)

In Fig. 2.10, the surface state model for the metal-dielectric case is displayed. For the electrons to pass from one material to the other, the work function must be overcome [49]. There are two cases. One is when the metal has a higher Fermi energy (E_f) than the neutral energy state of the dielectric (E_n), meaning that the metal will become positive and the dielectric negative. The other case is the opposite. Starting with the first one, from Figs. 2.10(a)-(c), the metal will donate electrons to the dielectric before and during contact, raising E_n above the Fermi energy of the metal. This increases the work function by the difference between E_f and E_n to receive new electrons [47, 49]. When both materials are separating and distancing from each other, [Fig. 2.10(c)] and with increasing temperature,

due to the electrons' having high energy, it increases the number of electrons that escape from the dielectric, because it is easier for them to overcome the work function in a higher temperature environment by thermionic emission [47, 48]. Some of the escaped electrons may be recaptured by the metal because of the positive charge its the surface. In the case where the metal becomes negative and the dielectric becomes positive [Figs. 2.10(d)-(f)], it is E_n that decreases compared to E_f and, when both materials are separated [Fig. 2.10(f)], the metal releases electrons by thermionic emission [47–49].

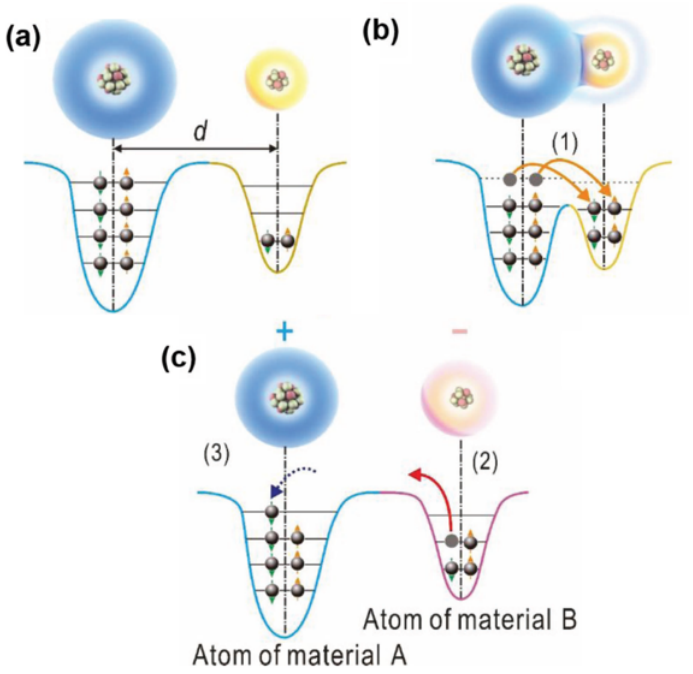

FIGURE 2.11: Illustrations of the cloud well potential for the contact electrification effect before **(a)**, during **(b)** and after contact **(c)**. (Adapted from Ref. [48].)

The cloud well potential model, present in Fig. 2.11, is described with the materials being atoms in a potential well with an electronic cloud and what happens during the contact-separation of the materials [47, 48]. In Fig. 2.11(a), the atom on the left possesses electrons in higher energy levels than the atom on the right, indicating that these electrons have more energy but are unable to overcome the potential well.

The potential barrier between atoms is only lowered when both materials come into contact, causing the electronic clouds to overlap and allow electrons from the atom on the left to depart to the atom on the right to lower energy states [Fig. 2.11(b)] [48, 53]. When both materials are further apart, the potential barrier rises to the previous state and some electrons on the right atom escape due to thermionic emission to the atom on the left or

are simply emitted into the air [Fig. 2.11(c)]. As the thermionic emission increases with the temperature, so does the emission of electrons [48, 53].

The temperature dependence of the mechanical properties and relative permittivity of materials also affect the performance of the dielectric [51]. Decreasing the relative permittivity will decrease the storage capacity of the material to retain charge, leading to a drop in performance [34, 51]. Studies are being conducted to strengthen the mechanical properties of materials, such as PDMS and PTFE due to the high degradation of their mechanical properties at higher temperatures [54–56].

2.7.2 Humidity

The TENG performance is influenced by air humidity, with electron transfer serving as the main charge transfer mechanism in the solid-to-solid TENG [21]. There are two mechanisms that humidity affects in the TENG. One is the reduction in charge transfer during the contact electrification of the materials. This occurs because a conductive layer forms on top of the material's surface upon the absorption of water molecules, lowering the material's surface charge density and reducing TENG performance [57, 58]. In Ref. [58], an experiment was conducted showing that the increase in humidity leads to a charge transfer decrease. The other process involves a very thin water layer, no thicker than 2 nm [58], which improves ion transfer across materials and boosts TENG performance [57].

Water may also change the triboelectric series. For example, in Ref. [57], in zero or very low humidity, aluminium has a tendency to turn positive, while polyethylene tends towards the negative value of surface charge density. However, when the humidity is high, both aluminium and polyethylene start to capture electrons.

2.7.3 Air pressure

The variation of air pressure is important for the performance of TENGs. Experiments performed from high vacuum (10^1 Pa) to above ambient atmospheric pressure (10^5 Pa) [59], showed that the performance of the TENG drops largely between 10^2 Pa and 10^3 Pa, depending on the composition of the atmosphere (air, O_2, or N_2) [59, 60]. Above ambient pressure, studies state an increase in the performance of the TENG [Fig. 2.12(a)] [58, 61, 62].

The drop in performance occurs because of electrostatic breakdown that is dependent of the atmospheric composition. As the surface charge density decreases abruptly when

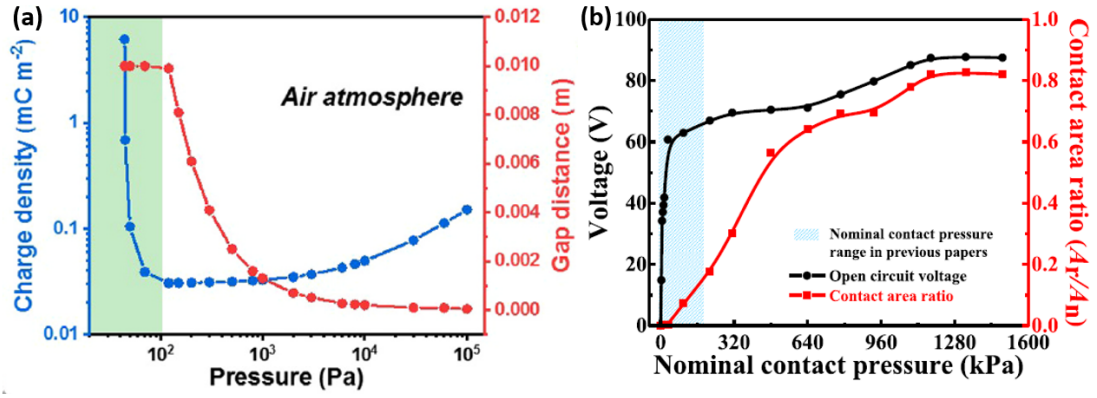

FIGURE 2.12: **(a)** Surface charge density as a function of atmospheric pressure. **(b)** Force exerted in a contact-separation mode TENG as a function of the voltage and ratio of real and nominal area. (Image adapted from Refs. [59, 63].)

breakdown occurs, this affects the other parameters that define the performance of the TENG. When the voltage reaches the breakdown voltage, the electric field is high enough that electrons are sent through the air from one material to the other, colliding with gas particles more frequently. This originates an ionisation collision that causes a chain of collisions, with the kinetic energy of the ionised electrons being superior to the ionisation energy of the gas in the atmosphere [59, 61]. However, when increasing the pressure past the electrostatic breakdown pressure, the performance of the TENG starts to increase due to an improvement in the surface charge density, although the increase does not reach the values prior to the breakdown. The reason behind this is that, as the pressure rises, the mean free path of electrons shortens, diminishing the effects of the electrostatic breakdown [59, 61].

2.7.4 Contact force

In the contact-separation mode TENG, the force exerted by the moving sample needs to be maximised to extract more performance from the TENG. Niu's model [27] predicts that the charge is uniformly distributed throughout the material (nominal area), not taking into account the surface roughness. However, in reality, the surface roughness alters the charge distribution, making some zones more concentrated than others [63, 64]. Taking into account the surface roughness, the triboelectric materials, when coming into contact, deformation occurs, maximising the ratio between the real area in contact and the nominal area of the material, increasing the real contact area as the contact force increase [63, 64]. The increase in the ratio of the real and nominal area then increases the electrical field [64], the charges present on the surface of the materials, improving the performance

of the TENG [63]. The ideal case is to have such a strong force that the ratio between the areas is one. The generated voltage and current increases linearly with the applied force, while the ratio of the real area and the nominal area is smaller than one and saturates at values close to one [Fig. 2.12(b)] [23, 63].

2.8 TENG's applications

Despite this work not being focused on a TENG application, it is important to have a very brief overview of some potential interesting applications. In medicine, TENGs still have a long way to reach the market because of their reliability in performance and their reaction to the contact of the human body to parameters such as temperature, sweat, and wear of the material. Interesting prototypes were conceived mainly using PDMS and PTFE due to their high flexibility and non-toxicity. One interesting prototype used, present in Fig. 2.13(a), was a PDMS device inserted on the wrist [32]. This device measured the pulse with such precision that it could distinguish between a healthy pulse and a pregnant pulse. For further reading on the applications of the TENG in medicine, Ref. [32] presents a related state of art.

Another of the main applications is harvesting the energy of motion of the human being. For example, implementing the TENG on shoes [Fig. 2.13(b)] [65]. This device does not solely rely on a TENG but also on a piezoelectric nanogenerator and an electromagnetic generator to solve the limitation on the current TENG outputs. This shows that TENGs can work with other nanogenerators [65].

TENGs can also be applied to harvest the energy of ocean waves. Navigation floating buoys typically use a photovoltaic panel (PV) to produce energy stored in a battery to power their sensors and the light they use to signal their presence. Because of the oscillations caused by ocean waves, floating buoys cannot always maintain the same orientation and are highly dependent on the weather and panel inclination. Thus, the PV is not always in the optimal orientation and the weather can be cloudy sometimes, reducing the energy produced. There are types of floating buoys to study weather conditions and water salinity, where they only rely on a battery to work and it needs to be replaced periodically [30].

The TENG can address all types of floating buoys by being able to always produce energy from the waves' oscillations without needing much maintenance. Since the TENG is implemented inside the floating buoy, it can endure the harsh conditions of the sea and

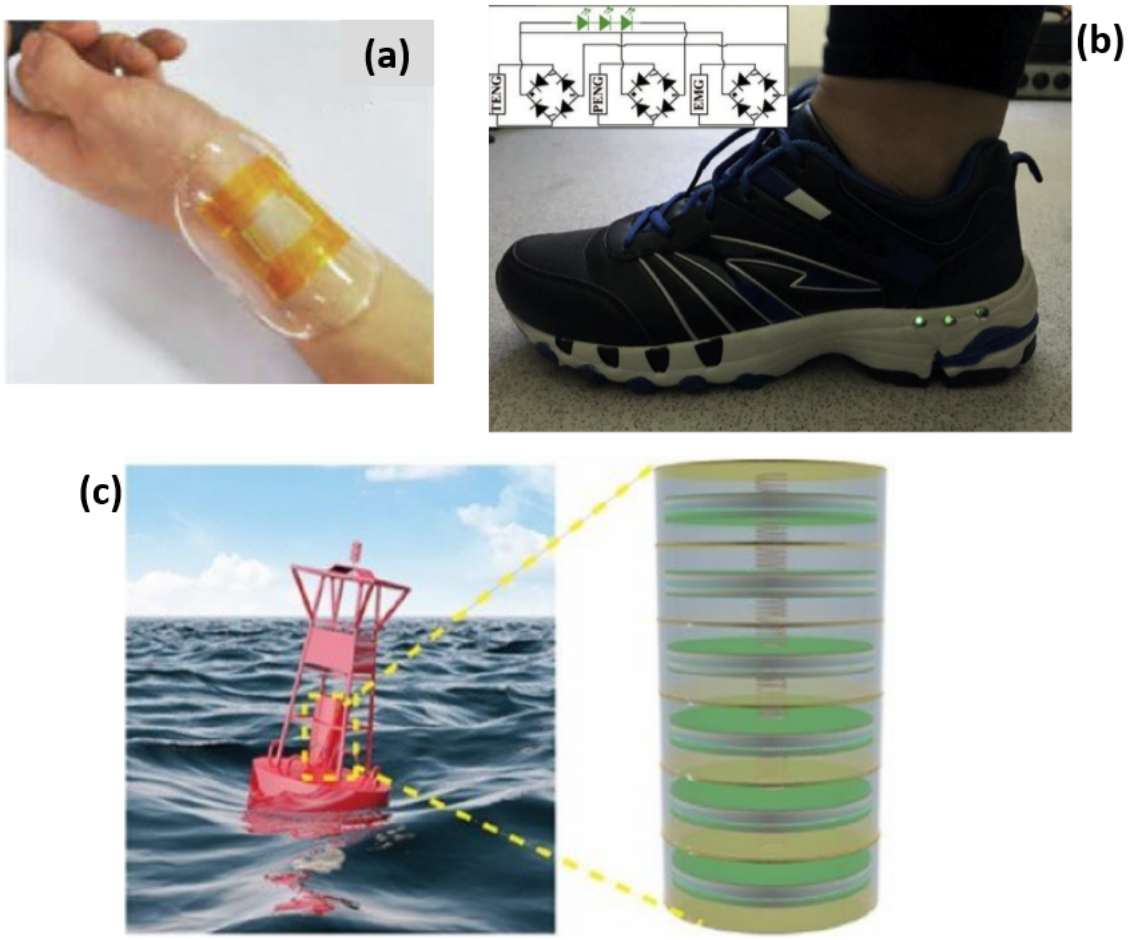

FIGURE 2.13: **(a)** PDMS device to measure the current on a person's wrist. **(b)** A shoe with a TENG, a piezoelectric nanogenerator, and an electromagnetic nanogenerator combined to generate energy through walking. **(c)** A floating buoy with a multilayered contact mode TENG. (Images adapted from Refs. [30, 32, 65].)

resist corrosion. Despite the ocean waves having abroad set of amplitude and frequency (below 5 Hz), TENGs are still able to produce energy in an efficient manner. In Fig. 2.13(c), a multilayered contact mode TENG used to produce energy is applied to a floating buoy [30].

Chapter 3

Numerical and experimental procedures

This chapter is divided into two parts. First, we will present the basis of simulating TENGs in COMSOL and the important considerations that were taken due to simulation time constrains and solution convergence. In the second part, the experimental component of this thesis is discussed, in which the output properties (voltage, current, and power) of TENGs were measured as a function of temperature using a specially developed setup.

3.1 Simulating TENG properties using COMSOL

Various properties of the contact mode TENG can be simulated with the help of COMSOL using a finite element method. To model a TENG in COMSOL, the two triboelectric materials and the two electrodes can be seen as an AC voltage source and a capacitor with variable capacitance with charges $+Q$ and $-Q$ in the electrodes (Fig. 2.5). The voltage and current are measured while passing through an external load resistance.

3.1.1 Important remarks

Regarding our COMSOL simulations, several considerations must be first stated. The first is that the simulations were performed in two dimensions due to time constraints. Thus, the system consisted of a rectangular or square boundary to set the surroundings of the TENG as air, and the TENG was built with two copper electrodes and one insulating layer on each. For most simulations, the bottom triboelectric layer is nylon, while the

top one is PTFE. The only exception is the study of the effect of the relative permittivity of the triboelectric layers on the corresponding output properties, where the top material is nylon and the bottom material is PDMS. With the aid of the moving mesh module, the top electrode and material can be moved closer or further apart from the bottom electrode and material. COMSOL has a list of values for most of the parameters of materials, including the relative permittivity for nylon, PTFE, and PDMS. However, it does not have the relative permittivity of copper since it is a conductor. Nevertheless, it needs this value to perform the simulation, and a value of 1×10^{10} was used. Connected to each electrode is a load resistance with a defined value.

Even if the simulation is in two dimensions, COMSOL still performs calculations in three dimensions. A parameter called out-of-plane thickness in the electrostatic module must be defined and, to be consistent with the size of the sample, the value defined was the same as the length of the sample to have a square shape. COMSOL makes the assumption that the voltage value will remain constant throughout the third dimension of a 2D simulation. An important remark that was taken into account was that if the out-of-plane thickness is smaller than 1 µm, the simulations would take too long to simulate.

The top triboelectric material performs a linear movement with a velocity (v) defined:

$$v = \frac{2(x_{max} - x_{min})}{T}, \tag{3.1}$$

where x_{max} and x_{min} are the maximum and minimum distance between materials that represent the distance covered and T is the duration of a TENG's cycle, which only half is necessary for the distance covered. A small (but not zero) minimum distance had to be defined due to the blocks' inability to come into contact in COMSOL. The function defined to execute the linear movement in Fig. 3.1(a) has a smoothing factor, rounding the function when the velocity sign changes. This is important because abrupt changes in the velocity sign can cause the calculations of the simulation to diverge and return a singularity error. The cost is that, the larger the smoothing factor, the further from the minimum distance one will be in the simulator [Fig. 3.1(b)]. So, if a 100 nm minimum distance is defined, this is valid only for a smoothing factor of 0. A study was conducted, prior to all the studies, to evaluate the optimal value of the smoothing factor since it has an impact on the results. A value of 0.019 was then fixed for all simulations, with the minimum distance being 21.38 µm. The smoothing factor also decreased the maximum distance between materials from 3 to 2.9786 mm. The base values set for the simulations

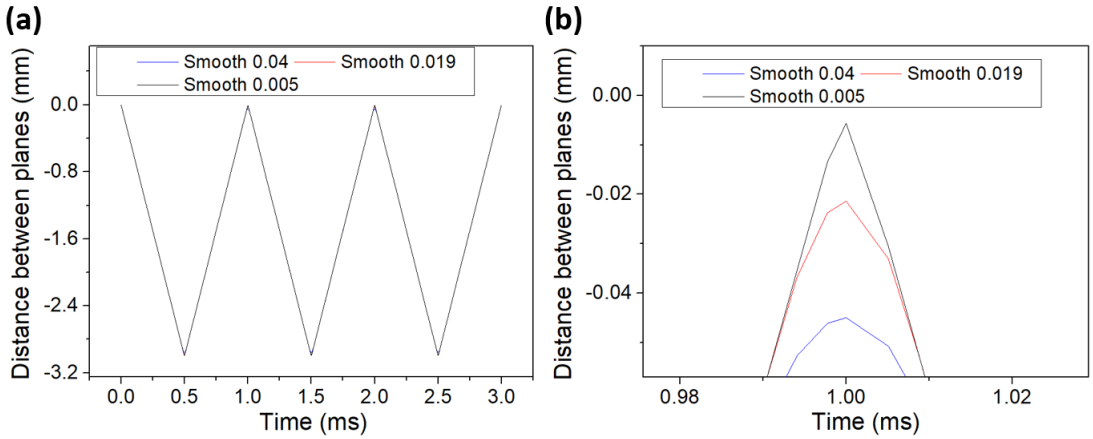

FIGURE 3.1: **(a)** Motion of the top electrode and PTFE with smoothing edges in the regions of velocity sign changes. The x axis represents the time and the y axis represents the distance of the PTFE surface towards the initial position in the y direction, at a distance of 3 mm from the nylon surface. **(b)** Zoom in the velocity sign change region with different smoothing factors.

are present in Table 3.1.

With this base values defined, one parameter was varied at a time for a given list of load resistances.

Parameter	value
Velocity	5.999 m/s
Period	1×10^{-3} s
Number of periods (cycles)	3
Time per step	1×10^{-6} s
Surface charge density of nylon	6×10^{-4} C/m^2
Surface charge density of PTFE	-6×10^{-4} C/m^2
Relative permittivity of nylon	4
Relative permittivity of PTFE	2
Relative permittivity of PDMS	2.75
Width of the border	0.1 m
Height of the border	0.1 m
Height/thickness of nylon/PTFE/electrodes of cooper	1×10^{-4} m
Width of nylon/PTFE/electrodes of cooper	1×10^{-3} m.
Maximum distance between nylon and PTFE surfaces	3×10^{-3} m
Minimum distance between materials (without smoothing factor)	1×10^{-7} m
Minimum distance between materials (with smoothing factor)	2.1×10^{-5} m
Smoothing factor	0.019

TABLE 3.1: List of parameters and the defined base value of each one. The value of the out-of-plane thickness is the same of the width of the materials, giving a TENG area of 1×10^{-6} m^2.

3.1.2 The TENG assembled and simulated in COMSOL in detail

To present an example how the program was conceived, a study varying the charge densities of the materials was used. The base values in Table 3.1 were used with the charge density of the materials varying during the study. The modules in COMSOL required are the electrostatic, electrical circuit, and moving mesh.

To start, the geometry and materials modules are used to make the TENG and its border. This is achieved by using a rectangle and defining the position, width and height of each one (Fig. 3.2). It is important to unite the geometries for COMSOL to treat them as a whole and set interior boundaries between materials. In fact, when COMSOL constructs the mesh and remakes it to perform the movement of the top tribopair, it will take into consideration the boundaries of each geometry. The topic about the mesh and moving the materials will be explain further ahead. After each geometry is built, each area has a number attributed to it, and the materials can be associated with each area using the numbers. In each material, it is important to give, if necessary, the remaining data that the numerical simulation needs. In this case, the relative permittivity of copper was provided, as explained previously.

The next step is to configure the electrostatic module. Firstly, the out-of-plane thickness is provided and then the terminals and surface charge density are associated with the respective sides of each rectangle of the materials and electrodes. The creation of the terminals is important to create the electrical circuit by selecting the option "Circuit" in

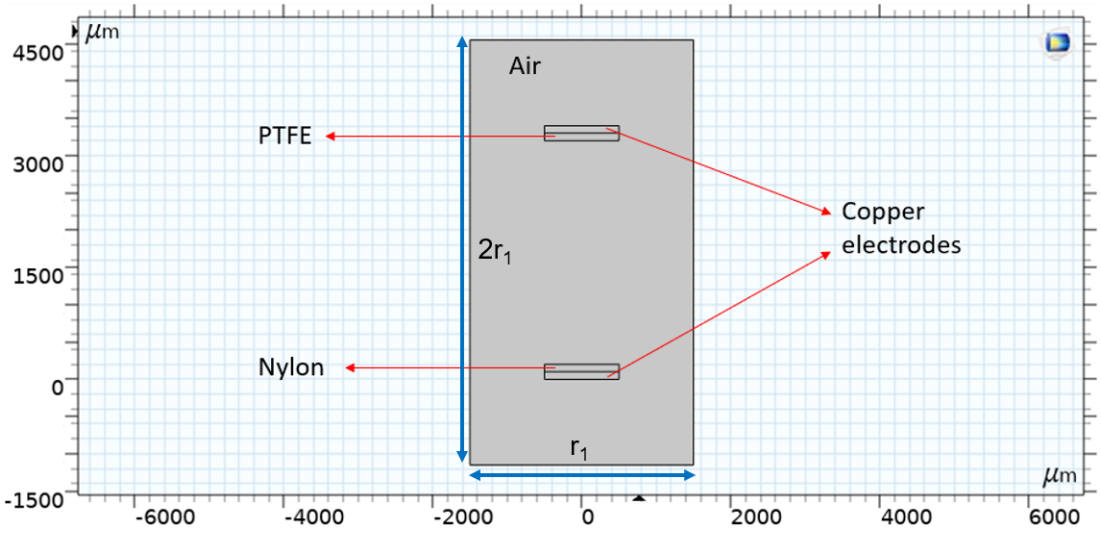

FIGURE 3.2: TENG built with the geometry module in COMSOL with a rectangular border and r_1=3 mm.

the terminal types. The two terminals were located between each electrode and the corresponding triboelectric material. Since they are closer together, COMSOL reckons that they are touching and there is only one border line separating the electrode from the material. The surface charge density was defined with a fixed value throughout the simulation at the surface of nylon and PTFE, respectively. This fixed value assumes that the surface of the triboelectric materials is already saturated with charge. This is not the case in a real experiment, because the surface of the material is rough and the charge in the materials is not saturated at the beginning and the charge distribution can concentrate in specific areas.

The electrical circuit module part enables the connection between the terminals and the resistance. Defining the ground as the sides of the air border to simulate the ground in the infinite is important to solve problems with errors that can occur with COMSOL. Except for the ground, which only requires one node, each component must have two nodes defined. To implement the terminals, an "External I vs U" for each terminal must be created with one node connected to the ground and the other node to resistance.

To set the top electrode and PTFE to move with time, the module "moving mesh" is used alongside the "mesh" module. There are three steps to make the movement possible. The first step is to create a mesh for the whole TENG. Defining the size of the mesh is to define the maximum size of the mesh segments because COMSOL can make smaller sizes of mesh segments in regions around the materials or when the materials are closing in on each other. The histogram in Fig. 3.3 shows that the quality of most mesh segments is superior to 0.7 and the minimum element quality was 0.6. The "finer" mesh size was the best choice considering simulation time and results because a smaller mesh would yield similar results while taking more time to finish. Nevertheless, if the majority of the values of the segments of the mesh were below 0.4 a finer mesh would be required.

The second step is to select movement area of the top materials. This is achieved using the "Prescribed deformation" and then selecting the boundaries of the top electrode and PTFE using the "Prescribed mesh displacement". Both are essential for the correct movement of the materials. The function used for the movement is present in Fig. 3.1(a) and the function should be represented, such as "$function(t[1/s])$" in the y direction. The reason for the function representation $t[1/s]$ is that COMSOL recognises t as a parameter of time, and the function only accepts a non-dimensional parameters. The previous two steps will deform the surrounding area of the top electrode and PTFE in each time step to

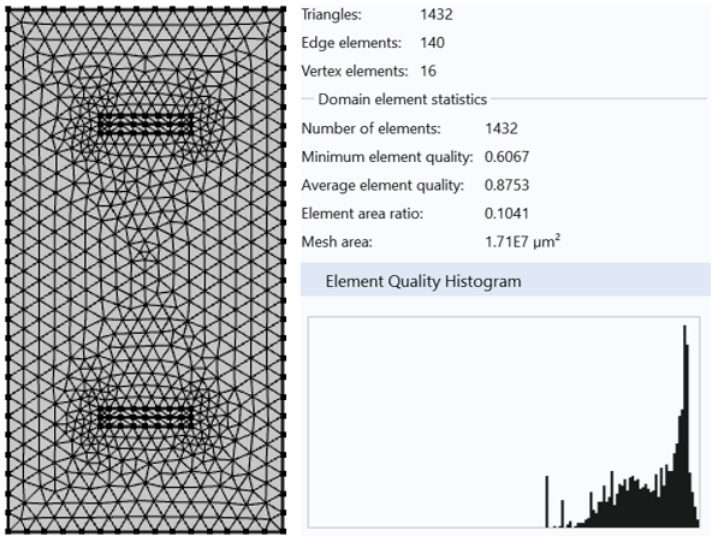

FIGURE 3.3: (Left) the TENG with a finer mesh applied, and (right) the mesh quality.

simulate a movement with an error. The deformation of the mesh occurs only in the area that has air because the mesh inside the objects that have borders, such as the electrodes, nylon, and PTFE, will not be altered [66]. The last step is to enable the surrounding air fill the gap left behind by the top electrode and the PTFE. This is achieved by applying the "free deformation" option to the air region.

With the contact-separation mode TENG prepared, it remains only to set the conditions of the simulations in the study section. The module selected is the time-dependent study, in which the convergence can be adjusted. The relative tolerance is one of the most crucial variables because, although a higher value increases the likelihood of the solution converging, a lower value decreases computation error. In these numerical simulations, the value used was 0.16, but the value could be increased to a maximum of 0.24 if needed to help with the convergence of the solution. Comparing this value with lower values of relative tolerance, the error was not significant, although more "noise" could be seen if a zoom towards the peaks was done.

Other parameters that help convergence are included inside the time-dependent solver in the fully coupled section. This program used a direct solver and, in the method and termination section, the non linear method chosen was the "automatic Newton", due its ability to deal better with highly non-linear cases. This increased the chance of convergence of the simulation, at the expense of using more computational resources, making it slower compared with the "constant Newton" method that is selected by default [67]. Below the non-linear method, there is the number of iterations that can be increased from

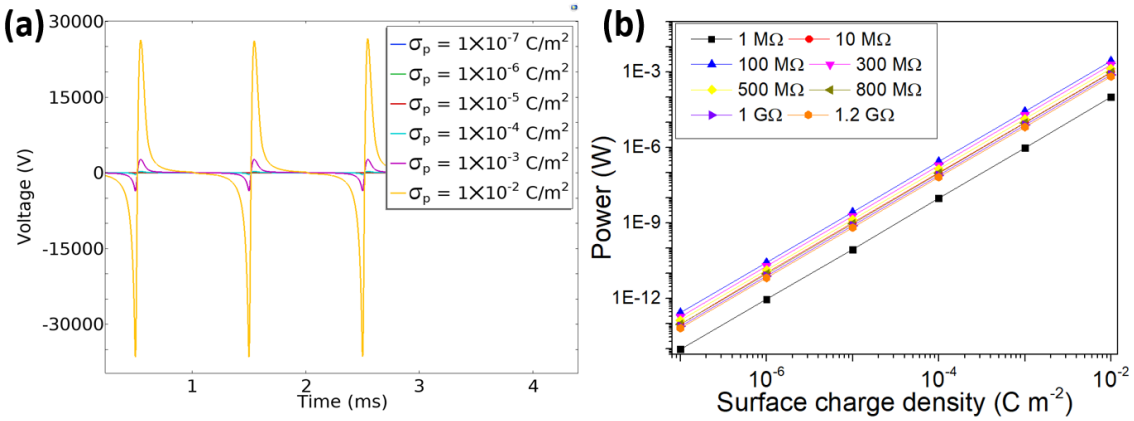

FIGURE 3.4: **(a)** An example of the voltage result produced by the TENG on COMSOL as a function of time. **(b)** Power output as a function of the surface charge density absolute value (positive for nylon and negative for PTFE).

4 to 25 and the tolerance decreased from 1 to 0.1. This increases the solution convergence, despite increasing the numerical simulation execution time.

To finish the time-dependent solver part, the creation of an automatic remeshing is needed to instruct the program to form a new mesh from the last step when the solver stopped when the previous mesh was formed beyond the limit parameter "distortion". The values used were between 1.3 and 1.6 and the higher the value, the more it allowed the mesh to distort. Varying this parameter between these values helped the convergence of the solution.

Lastly, the list for values of the surface charge density and the load resistance must be introduced in the parametric sweep. For the load resistance, 8 values were used that ranged from 1 MΩ to 1.2 GΩ. These are the load resistance values used to study the transition region. The value used for the I_{SC} was 100 Ω and for the V_{OC} was 100 TΩ. For the surface charge density, the values used ranged from 1×10^{-7} to 1×10^{-2} C m^{-2}, increasing one order of magnitude in between.

This gives a total of 60 simulations.

Figure 3.4(a) shows an example of the results obtained on COMSOL for the 500 MΩ of load resistance of the contact and separation peaks. In Fig. 3.4(b), the power output of the TENG increases linearly with the surface charge density. Since this was a case that serves as an example, only the power is represented as a function of the surface charge density. The current and the voltage also increase linearly with the increase of the surface charge density. In the studies performed in this work, the graphs of the voltage, current, and power as a function of the load resistance are relevant to observe the TENG

performance in the transition region and in the short circuit region, while the graphs of the voltage, current, and power as a function of the varying parameter are more appropriate to observe the evolution of tendencies of these parameters with a certain load resistance. This last type of graphs is always used for the I_{SC}, maximum power output, and V_{OC}.

3.2 Temperature dependent TENG measurements

This section is broken down into four sections: the developed experimental setup, the procedure to make the samples used on the experimental setup, the experience itself, and the experience's analysis of the results gathered.

3.2.1 The experimental setup

The experimental setup to test the triboelectric effect in the room temperature - 120 $^{\circ}C$ temperature range consisted in a chamber with infrared lights on top and a plate of steel where the TENG was placed (Figs. 3.5 and 3.6).

In Fig. 3.6, the linear motor LDZBL3M-200A3L is attached to a stainless steel tube that goes inside the box. At the other end of the tube, the moving TENG sample is fastened

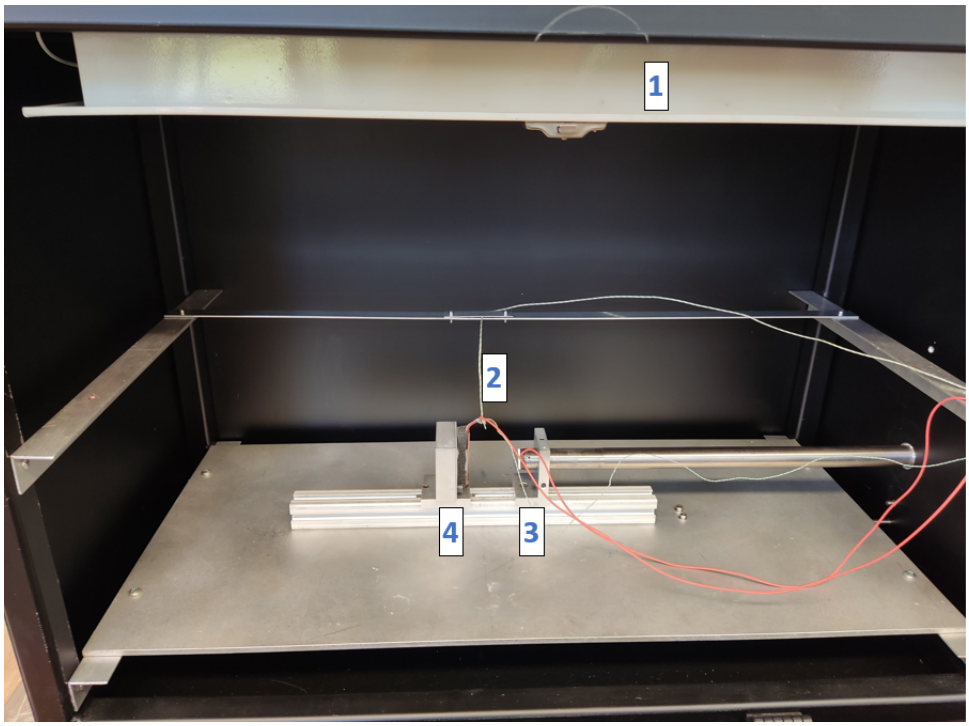

FIGURE 3.5: Temperature controlled chamber. 1-Infrared lights; 2-Thermocouple controlling the chamber temperature; 3-Support of the stainless steel tube with the moving sample; 4-Support of the fixed sample and foam.

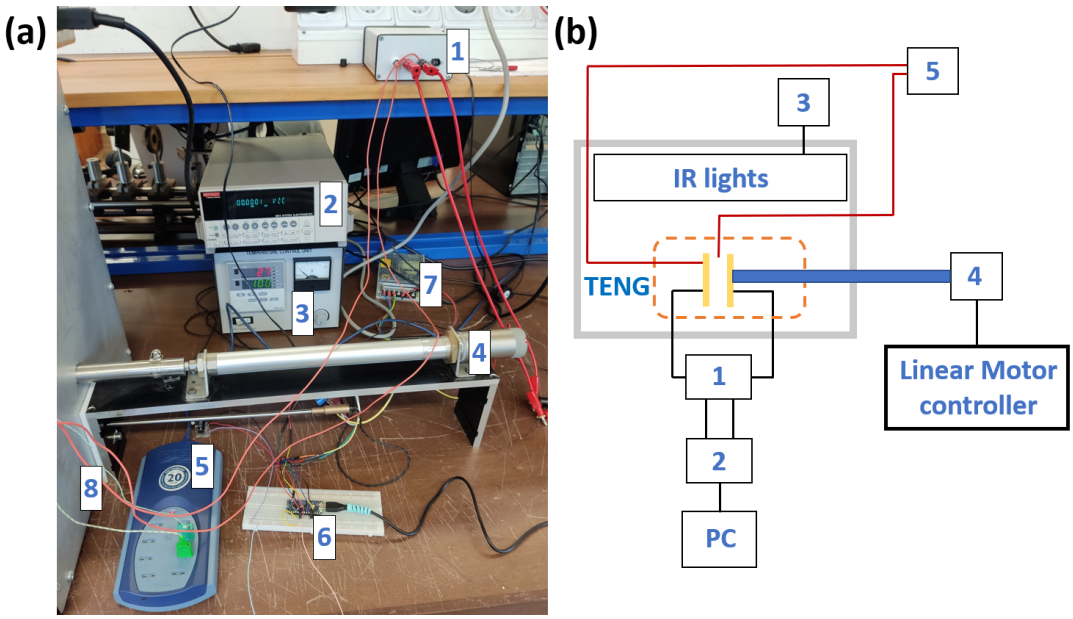

FIGURE 3.6: **(a)** Measurement setup and **(b)** scheme of the whole setup. 1-Box of resistances; 2-Electrometer; 3-Power supply of the infrared lights; 4-Linear motor; 5-Picolog; 6-Arduino that operates the linear motor; 7-Power supply (SRS-150-24) for the linear motor; 8-Acrylic plate between the chamber wall and the support of the linear motor. In **(b)**, the black lines are electrical connections, the red lines are the two thermocouple connections, the yellow lines are the TENG materials and the blue rectangle is the stainless steel tube that connects the linear motor to the TENG's moving sample, passing through a opening in the chamber.

to the tube (Fig. 3.5). The stainless steel tube was chosen for this application because it has a low thermal conductivity compared to other metals, allowing for the linear motor to operate below the limit operation temperature specified in the datasheet (40 °C). Despite this, stainless steel is still a good conductor of electricity and suffers from significant electrical losses. This issue was fixed by adding a small piece of phenolic between the stainless steel and the sample and gluing it with epoxy. The maximum distance between the fixed sample and the moving sample was 5 cm.

On the left side [Fig. 3.5(a)], there is the fixed sample and the foam. The foam is glued with double-sided duct tape to the support and the sample is glued in the same way but to the foam. The foam serves as an electrical insulator from the steel supports and also distributes the force that the moving sample applies to the fixed sample, lessening the damage done to both samples. The foam used was a polyurethane foam with 9 mm of thickness that is able to withstand temperatures close to 70 °C for long periods of time and 180 °C for short periods. Because of the better results obtained on the TENG using a foam compared to the case without it, the use of this foam led to improved distribution of force throughout the fixed sample.

To control temperature on both samples, we placed thermocouples on the samples and another one suspended in the air, near the collision region of the samples [Figs. 3.5 and 3.6(b)]. The thermocouples are connected to a picolog 6 TC-08. The linear motor temperature cannot exceed 40 $^{\circ}C$, so a thermocouple was also placed close to one of the supports of the linear motor outside of the chamber during the optimisation of the setup for measurement.

After optimisation, only the thermocouples suspended in the air and the one at the fixed sample remained, because they affected the triboelectric results by reducing the measured voltage by one to two orders of magnitude. The thermocouple of the fixed sample was glued with copper duct tape to the back of the fixed sample. A thermocouple attached to the moving sample was used on occasions to measure the temperature gradient between samples when voltage and current measurements were not being performed.

The infrared lights were used with a controller to set the temperature (Fig. 3.6) by varying the intensity of the infrared lights.

The linear motor is mounted on top of a stainless steel support that is fixed to the box. During the tests, the temperature of this steel support began to rise and eventually surpassed the operating temperature of the linear motor. A 5 mm acrylic plate was affixed between the linear motor and the box to solve this issue (Fig. 3.6).

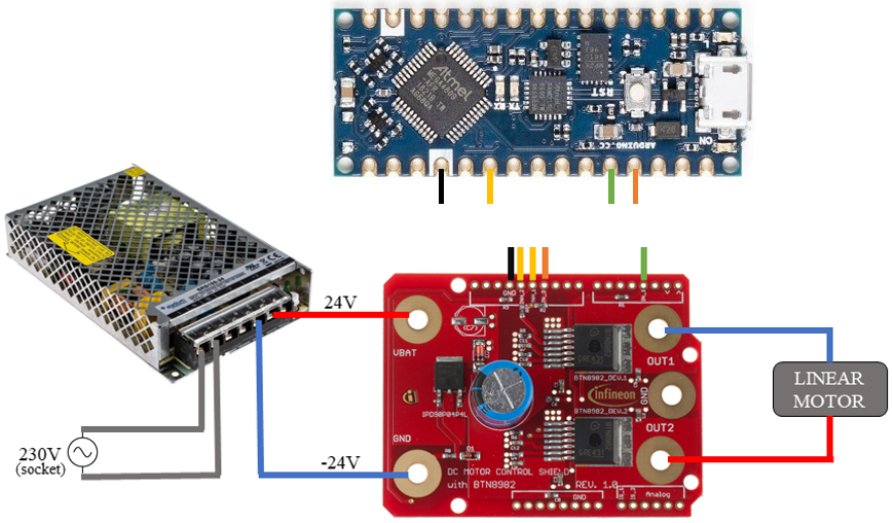

FIGURE 3.7: Diagram showing how the Arduino and associated components work with the linear motor.

The linear motor setup (assembled by Patricia Soares for a different project) can be

seen in Fig. 3.7. This setup uses an Arduino Nano to control the linear motor's collision to adjust the movement's velocity and direction. An H bridge (DCMOTORCONTRBN8982TOBO1) was used to connect the Arduino and a device power source of 24V DC (SRS-150-24) to supply the voltage required for the linear motor to function. The Arduino program allows to be controlled by changing the duty cycle of 8 bits. A value between 0 and 255 (from 0% to 100% of duty cycle) can be used to set the velocity of the linear motor, although in practice these values should be kept within the range of 100 - 190 range, because smaller values would prevent the motor from moving, and higher values would risk damaging the engine. 140 was the preferred value for the entire experience.

With the previously specified value and a sample separation of 5 cm, the TENG runs at a frequency of collision of (0.52 ± 0.03) Hz. The velocity of the linear motor was 5.2 cm/s, fast enough to maximise the force made by the moving sample to reach the performance saturation through the collision force.

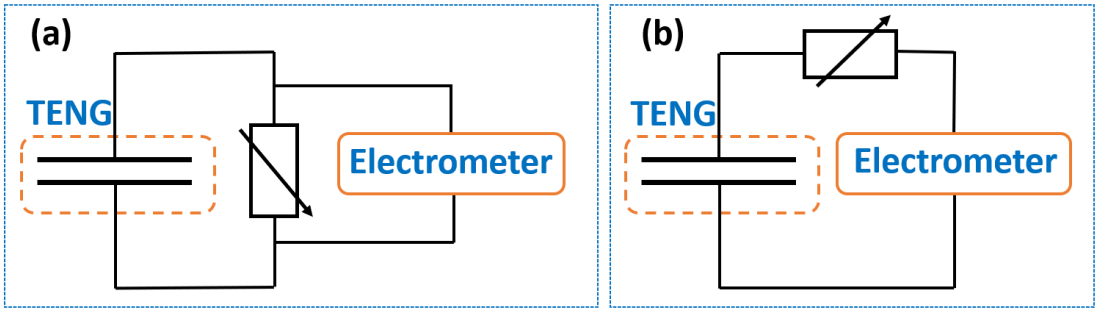

FIGURE 3.8: The ammeter-voltmeter technique to measure **(a)** the voltage and **(b)** current.

In Fig. 3.8, the scheme of the circuits to acquire data from the TENG is shown. A Keithley 6514 electrometer was used to acquire data from the TENG. The samples of the TENG were connected in parallel with the box of resistances if voltage was to be measured [Fig. 3.8(a)] or in series if current was to be measured [Fig. 3.8(b)]. The box of resistances is powered by a 9 V power supply, and has 12 resistances ranging from 100 Ω to 470 MΩ. To switch between resistances, and acquire data with the electrometer, a labview program was used. The resistance used to measure the V_{OC} was 470 MΩ and for the I_{SC} was 100 Ω.

3.2.2 Sample preparation

During this thesis, different samples were prepared and measured, including PDMS mixed with nanoparticles (Table 3.2). Sylgard 184 from Dow Corning was used to create

Sample	Electrode	Area size (cm)	Thickness	Support
Copper	Copper	2×6	2 mm	moving
Aluminium	Aluminium	2×6	2 mm	moving
PDMS (220B)	Copper	3×4	220 µm	fixed
PDMS (220C)	Copper	3×4	220 µm	fixed
PDMS (220A)	Copper	2×6	220 µm	fixed
PDMS (77A)	Copper	2×6	77 µm	fixed
PDMS (52A)	Copper	2×6	52 µm	fixed
$SrTiO_3$ (Nano A)	Copper	2×6	220 µm	fixed

TABLE 3.2: List of samples used and their dimensions. The code in parenthesis are the names attributed to the fixed samples to distinguish them.

the PDMS films, and a 1:10 ratio of curing agent and elastomer was poured into the beaker. Both ingredients were combined by hand stirring with a spatula for two to three minutes, until numerous little air bubbles began to form. Next, the removal of the air bubbles inside the PDMS was done by inserting the beaker into a vacuum chamber for 30 to 60 minutes, depending on the quantity. To deposit the PDMS on the electrode, a spin coating setup was used with the aid of a vacuum pump to hold the sample in place. Table 3.3 shows the thickness dependence on the spin coating angular velocity applied for 30 seconds (according to Ref. [68]). After the samples were deposited on the copper electrodes, they were placed in an oven at 100 $^{\circ}C$ for 35 minutes.

Spin coating velocity (rpm)	500	1000	1500
PDMS Thickness (µm)	220	77	52

TABLE 3.3: Spin coating angular velocity required for the PDMS to have a specific thickness [68].

For the nanoparticle-doped PDMS samples, we chose Strontium Titanate ($SrTiO_3$) nanoparticles from Sigma Aldrich with a diameter smaller than 2 µm and relative permittivity of 300 [25]. Since there was no established method for creating these samples, existing methods were modified and optimised [43]. Toluene was utilised as the solvent for PDMS since it is less toxic than hexane, although extreme caution must be taken by wearing a filtering FFP3 mask, safety glasses, gloves, and a lab coat, as well as doing the mixing inside a hotte.

The first step is to put the elastomer into the beaker at a ratio of 10:1 to the curing agent, which will be added later in the manufacturing process. Next, the nanoparticles of $SrTiO_3$ are added at a ratio of 1:10 to the elastomer, following a hand stirring mixing with a spatula for 2 to 3 minutes. With the beaker inside the hotte, the toluene is added.

Since the quantity of elastomer used was around 5 g, the quantity of toluene added was 13.5 ml. A magnet was added with the length a little smaller than the diameter of the beaker to guarantee a more uniform dispersion by preventing the magnet to stay on one side of the beaker. Magnetic stirring was performed at 40 $^{\circ}C$ and 400 rpm for 30 minutes with the beaker on a hot plate, supported by a claw to keep it from moving, and another beaker filled with water to further manage the hot plate's temperature. The parameters were then modified to 50 $^{\circ}C$ and 300 rpm for the following two hours. The hot plate's velocity was then reduced to 100 rpm for 45 minutes while it cooled and reached room temperature.

The curing agent was added and the mixture manually stirred for 2 to 3 minutes after the beaker reached room temperature and the toluene evaporated. After that, the solution was degassed by placing the beaker in a vacuum chamber for an hour to eliminate any air bubbles and leftover toluene. The samples were deposited with a spin coating process with a rotation velocity of 500 rpm, during 30 seconds to aim for a thickness of 220 µm. Finally, the samples were inserted into the oven at a temperature of 110 $^{\circ}C$ for 20 minutes.

3.2.3 Experimental procedure

During the experiments, the first 16 minutes of operation of the contact-separation mode TENG was to charge both tribopairs at room temperature, since they were not in their saturate state of surface charge density. This charging until saturation was measured using the V_{OC}. The temperature measurements started only after the charging process was concluded.

One of the key concerns was that the experience needed to be made quickly enough because PDMS would start curing significantly above a temperature of 50 $^{\circ}C$ if it lasted for more than three hours. The solution to this issue was to do a slow heating between 20 $^{\circ}C$ and 50 $^{\circ}C$ that lasted for about an hour, followed by a rapid heating to 100 $^{\circ}C$ that lasted for an hour at maximum. The measurements of the current or voltage for each load resistance took 30 seconds.

The infrared light current was gradually increased in order to raise the chamber's temperature taking into account the intended experiment's duration. The temperature variation during each 30 seconds measurement did not exceed 1 $^{\circ}C$ and the gradient of temperatures between samples was inferior to 2 $^{\circ}C$ or 3 $^{\circ}C$ depending on if the moving sample was copper or aluminium.

One thing to note is that the thermocouple in the fixed sample is between the copper electrode of the sample and the foam. Since copper and PDMS have very different thermal conductivities, and the moving sample is a metal sample of aluminium or copper, the temperature measured in the fixed sample might not correspond to the true temperature of the PDMS. However, constant collisions between samples are occurring, the measured gradient between samples is between 1 $^{\circ}C$ to 3 $^{\circ}C$ and the maximum PDMS thickness is 220 µm, making it safe to assume that the temperature of the PDMS falls into this range.

After the experiment, the box was opened to cool down to room temperature, making the cooling process faster. This aided in addressing the PDMS curing issue. A new experiment started when the temperature of the samples reached 30 $^{\circ}C$.

3.2.4 Data analysis procedures

The data acquired from the setup consists of data files for each temperature measured for the voltage or the current. The graph of this data consists in positive and negative peaks that are written into a file for each temperature. A python program (written by Rita Bugalhão) was used and adapted for this case to obtain the maximums and minimums for each file (Fig. 3.9). The program had upper and lower thresholds and a periodic limiter to prevent values that are not the real maximums or minimums from being considered,

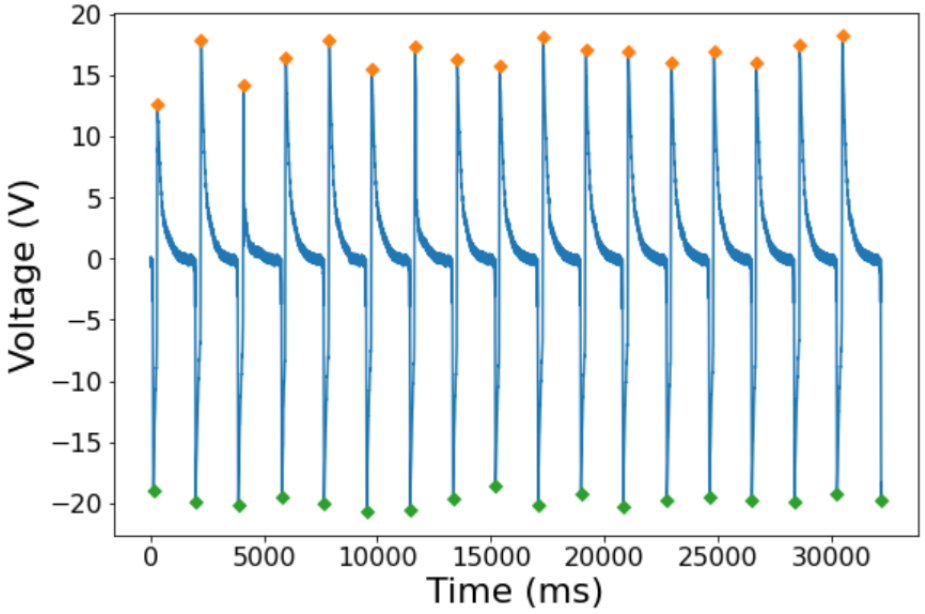

FIGURE 3.9: V_{OC} from a TENG in 30 seconds of data acquisition. The python program was used and, with the right values for the limiters, the maximums (in yellow) and the minimums (in green) were obtained.

being especially useful at higher temperatures where the voltage and current drop considerably. The upper (lower) threshold limited the detection values below (above) the threshold, while the periodic limiter sets a time value after each peak before detecting the next one. With the maximums and minimums found the program then calculated their average and standard deviation, the frequency of collision and the period between maximum and between minimum peaks. The previous values were all joined together in one file with their corresponding temperature at which they were measured.

Chapter 4

Numerical simulations results

In this chapter, it is important to study the parameter variation tendencies of the area, nylon thickness, and relative permittivity. Before proceeding to these studies, it is important to understand the effect of the border on numerical simulation results; to determine a suitable resistance to measure the V_{OC} and the effect of a smaller resistance used that leads to peak decay. The values used to simulate the TENG are present in Table 3.1. This is valid for all simulations, unless other values are used that are specified in the respective study.

4.1 The influence of the border size on the numerical simulations

The study of the influence of the border size on the obtained results is a critical first step on any numerical simulation. Therefore, a study with different border sizes was conducted to better understand the resultant effects. It is important to keep in mind that if the border is increased in size, the gigabytes (Gb) amount of computer memory used increases. This can make a Gb difference for simulations with only 3 cycles of TENG.

With this statement, it is important to optimise the size of the border for the study in question without shrinking the area of the border. A rectangular border shape with the bigger side being double of the smaller one (r_1) was used (Fig. 3.2) and a resistance of 100 TΩ was used to measure the V_{OC}. Analysing the data [Figs. 4.1 and 4.2(b)] that had a TENG area of 1 mm^2, the r_1 used in Fig. 3.2 simulations was 3 mm, and it is clearly observed that this is a low value to use because the peaks have a rounder shape and a lower value that it could achieve. Further reducing r_1 causes the peaks to split in two and have a minimum between them, while with r_1 larger than 0.1 m, the border's size

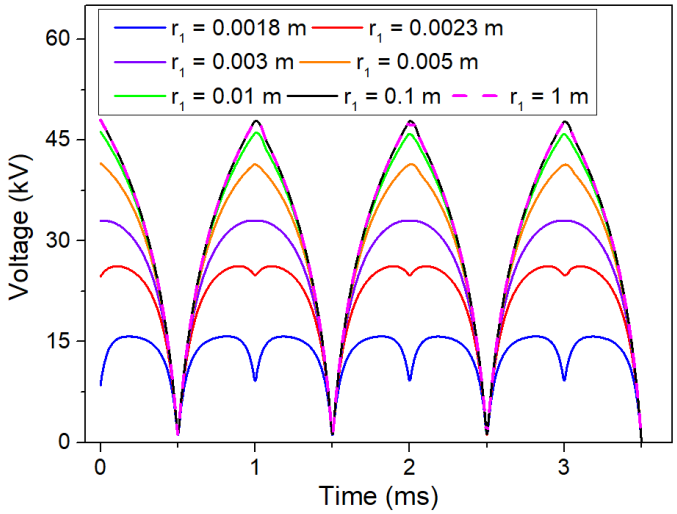

FIGURE 4.1: Graph of the voltage measured while varying the size of a rectangular border. In the legend, the length of the smaller side is indicated (r_1).

increases become irrelevant for output outcomes. This value is important, but it should be adjusted according to the situation, such as the area variation of the TENG or the increase in the thickness of the material.

For transition region studies, the power peak is between 100 MΩ and 500 MΩ. With this in mind, the border effects on the numerical simulation with a load resistance of 300 MΩ [Fig. 4.2(a)] show a significant decrease in the current and the voltage for the two lower values of border size values. However, for higher values, the simulated values are relatively constant with the observed differences being related with the high relative tolerance of 0.22 - 0.24 used.

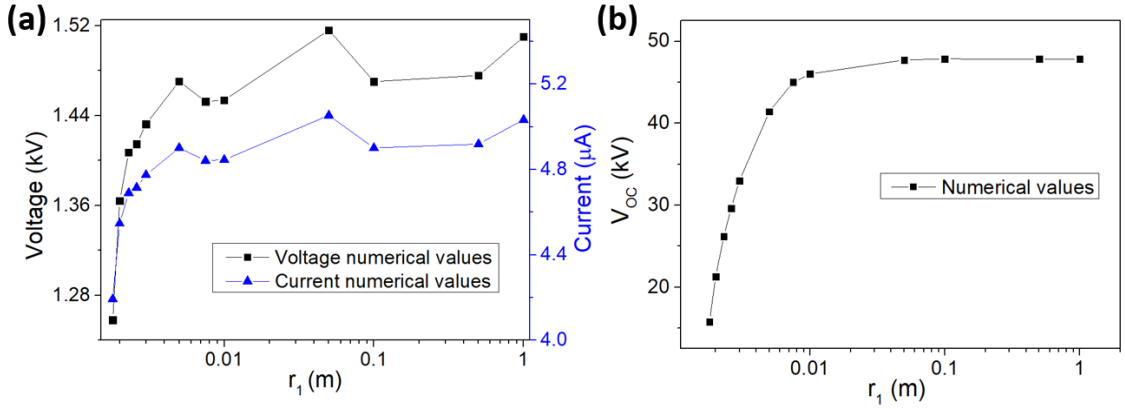

FIGURE 4.2: **(a)** Voltage and current variation as a function of the border size (r_1) for a load resistance of 300 MΩ. **(b)** V_{OC} with a load resistance of 100TΩ as a function of r_1.

In conclusion, the V_{OC} is the parameter most affected by the border size, and the border smaller side should be at least 34 times larger than the TENG system.

4.2 Open circuit conditions

An important first step to take is to define the numerical conditions giving the actual V_{OC} load resistance and how it is affected by changing the geometrical parameters.

In the open circuit conditions there is no charge transfer and this is achieved with a high load resistance value. The search for the ideal load resistance to measure the V_{OC} is motivated by the fact that, with the increase of the load resistance used in the simulations, the results start to show non-uniform peaks and the amplitude of the peak decreases from peak to peak, as seen in Figs. 4.3(a),(b) and the voltage decay displayed in more detail in Fig. 4.3(c). This is the transient state, and there are two ways to perform this study.

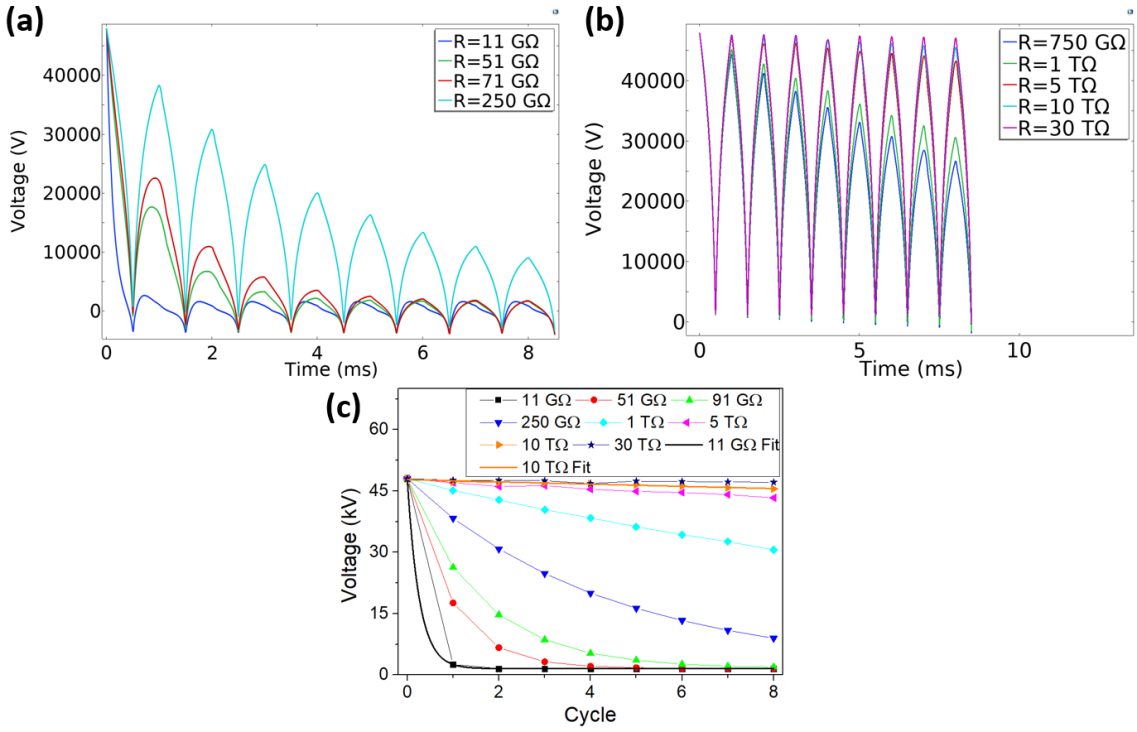

FIGURE 4.3: The non uniform peaks that form after the transition region for **(a)** GΩ load resistances and **(b)** TΩ load resistances. **(c)** Voltage as a function of the cycle for the peaks values displayed in **(a)** and **(b)**.

One is to compare the results of the various load resistances with the results of a multimeter with the voltage option that has a very high load resistance. To do this in COMSOL, the component voltmeter is inserted into the TENG circuit instead of a load resistance. Since the graph using a voltmeter is similar to the numeric values of the load resistance 10 TΩ in Fig. 4.3(b), it should be enough to study the tendencies of V_{OC} with the parameters specified previously due to the decay between cycles being less than 1%. Nevertheless, one has to point that for both the voltmeter and 10 TΩ, the results show a difference of

3% compared with the 30 TΩ case in the eighth cycle, confirming that one is already in a transient state, so that the V_{OC} values do not correspond to the real value that should be measured. The second option is to let the voltage stabilise, meaning more cycles are needed. That can also be observed in Fig. 4.3(a), with the results for 51 and 71 GΩ being stabilised after the fifth cycle. The downside of this method is that there is a risk that the charge of the electrodes is not zero and instead of a small number of cycles, more are required. If eight cycles are used in the case of these load resistances, simulations take at least 3 times the time to finish and use three times the memory. Another drawback is the requirement to adjust the load resistance used to obtain V_{OC} for parameters that vary significantly with the optimum resistance, such as the area of TENGs. The possible advantages are that the values measured are more realistic and the parameter variation is more accurate.

Therefore, the first method will be the one used primarily, and the second one will be used in specific occasions.

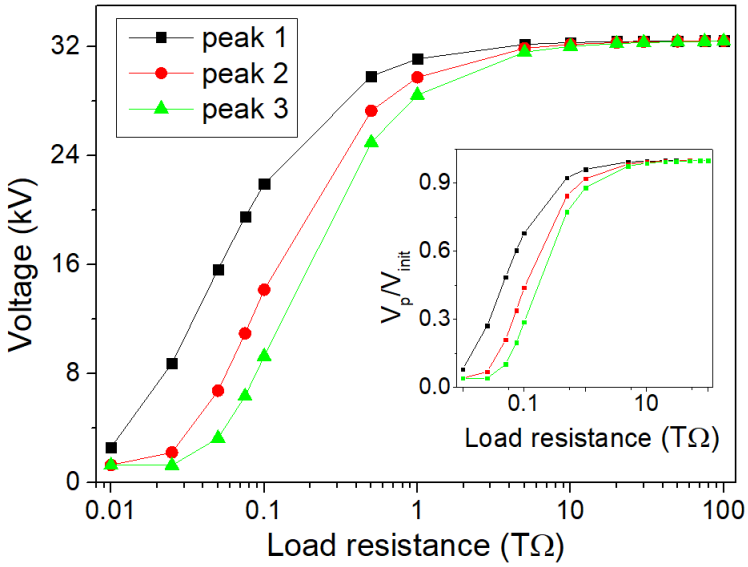

FIGURE 4.4: Voltage as a function of the resistance for the three peaks. Inset: ratio between each voltage peak (V_p, where p=1, 2, 3) and the initial peak (V_{init}) at 0 seconds instant.

To find the ideal resistance to obtain V_{OC}, in the numerical simulations, we varied the load resistance between 100 GΩ and 100 TΩ for three contact-separation cycles. The objective is to find a value of load resistance such that the voltage drop between peaks is negligible and the graph obtained for a given load resistance is similar to the one obtained when a voltmeter is used.

Analysing Fig. 4.4, the voltage drop between peaks steadily decrease with the load resistance increase, becoming negligible (smaller than 1%) above 10 TΩ , with the ratios V_p/V_{init} being close to one, matching the result obtained using the COMSOL voltmeter. The value chosen to measure the V_{OC} was 100 TΩ. This choice will be further validated in the area study due to the high variation of the optimum resistance with the area.

4.2.1 The transient state

The objective in this section is to study how the amplitude from peak to peak decays using different resistance values to better understand the transient state. For this study, a maximum of eight cycles was used to obtain better fitting curves (Fig. 4.3). This study will be concluded with lower values of load resistance where a delay in the peak is observed.

The fit expression to characterise the voltage decay from cycle to cycle is:

$$V = V_0 + C \times \exp\left(-\frac{p}{R_0}\right), \tag{4.1}$$

with V_0, C and R_0 being fitting constants and p the number of the cycle. To validate the fit, the R^2 is represented along with other important fit constants.

The graph in Fig. 4.5 shows that the R_0 decreases towards zero for high load resistances. The C and V_0 fitting remain constant (4.6×10^4 V and 1.6×10^3 V) up to 1 TΩ, with the quality of the fit decreasing for higher resistances.

As seen previously in Fig. 4.3(c), load resistances above 5 TΩ, the cycle-to-cycle decay becomes negligible, which makes the fitting curve unreliable, as seen in the decrease of

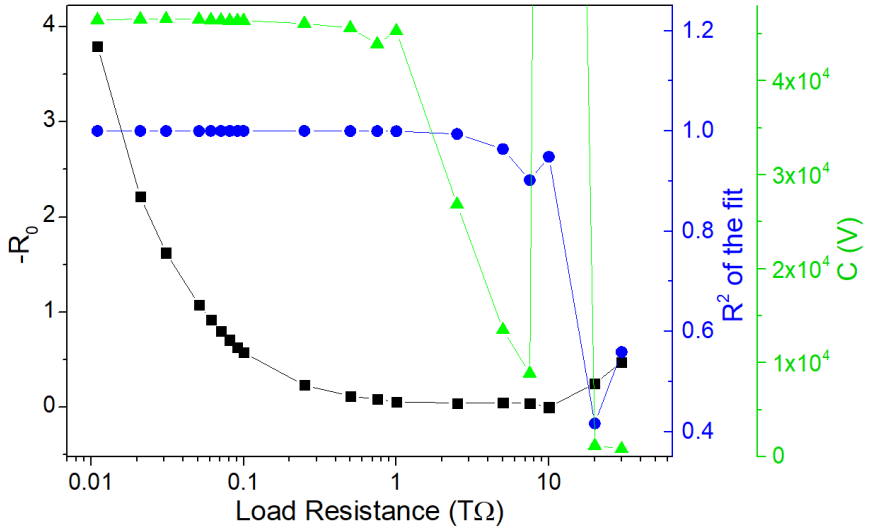

FIGURE 4.5: Evolution of the fitting parameters of Eq. (4.1) with load resistance.

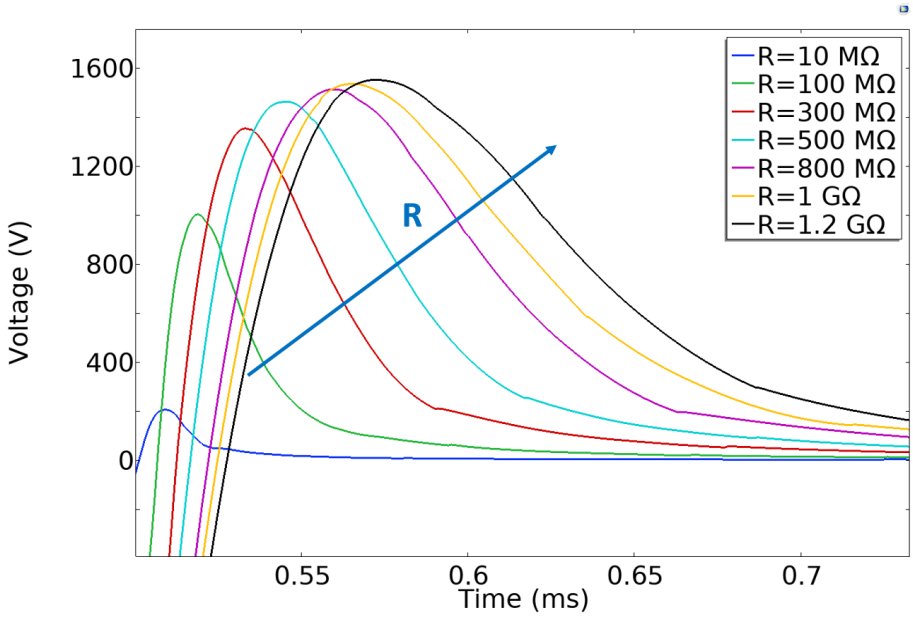

FIGURE 4.6: Voltage as a function of time showing the shift of the peaks with the increase of the load resistance.

R^2 and the deviation of V_0, C and R_0 parameters. For higher load resistances, more cycles would be required to have a better fit, but at the expense of a longer computation time.

In Fig. 4.6, the other effect seen during of the transient regime is displayed. As the load resistance increases, the slower movement of the charge induces a shift to the right on the separation peaks, deviating their maximum from the point where the minimum distance between planes occurs (0.5 ms). With the increase of the load resistance, the minimum charge value increases and time delay in the minimum peak occurs, contributing to a shift to the right and a slower decay of the voltage is observed. The results obtained in this section were also obtained in Ref. [29].

4.3 Influence of TENG area

This section is dedicated to the area variation study in the performance of the TENG, starting with the open circuit and short circuit regions and then the optimum resistance region.

4.3.1 Open circuit and short circuit regions

Adding the TENG area as a variable to the previous simulations and changing the border size to support larger area values, we started by showing how the area influences

the load resistance for which V_{OC} is achieved. This can be performed in two ways; the first is calculating V_p / V_{init} as a function of the resistance (where V_p is the obtained voltage in the p-th cycle, and V_{init} is the voltage at 0 seconds instant). Alternatively, one can plot the V_p / V_{init} as a function of the area.

For V_{OC}(S) determination, a square border 5 m of length was used. On the other hand, I_{SC} was obtained for a resistance of 1 kΩ and borders of 0.151×0.00207 m^2.

Despite the graphs in Fig. 4.7 only having two values for each case, in the numerical simulations performed there are a minimum of three different values of load resistance or area between them and there are results above and below the values displayed. It is important to notice the difference between the peaks for each value of load resistance or area. To avoid overloading the graphs with information, only two values for each case were displayed. As can be seen in Fig. 4.7(a), the voltage for 750 GΩ does not have a negligible decay per cycle until 10 mm^2, having a decrease in voltage drop per cycle with the increase of the area, while the voltage for 15 TΩ, the voltage drop per cycle for area above 0.1 mm^2 is negligible. In Fig. 4.7(b), it is seen that the smaller area has a higher voltage drop per cycle across the load resistance spectrum than the higher value, and with the increase of the load resistance, the voltage drop per cycle decreases.

The conclusion reached is that the smaller the area, the higher the load resistance has to be to reach the point of V_{OC}. This is in agreement with Niu's model of the contact-separation TENG, where the area is inversely proportional to the load resistance. This relation has not been verified here, only that the load resistance increases with the decrease of the area.

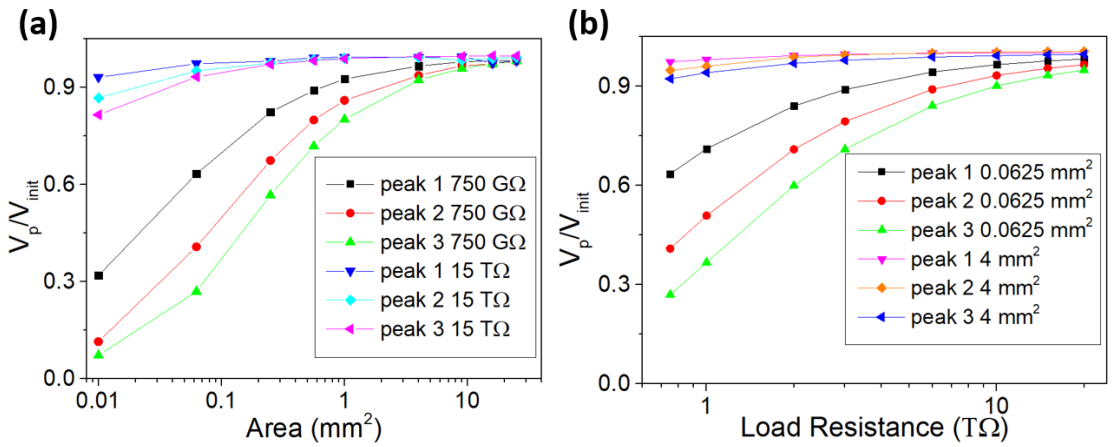

FIGURE 4.7: V_p / V_{init} as a function of **(a)** the area of the TENG, **(b)** the load resistance.

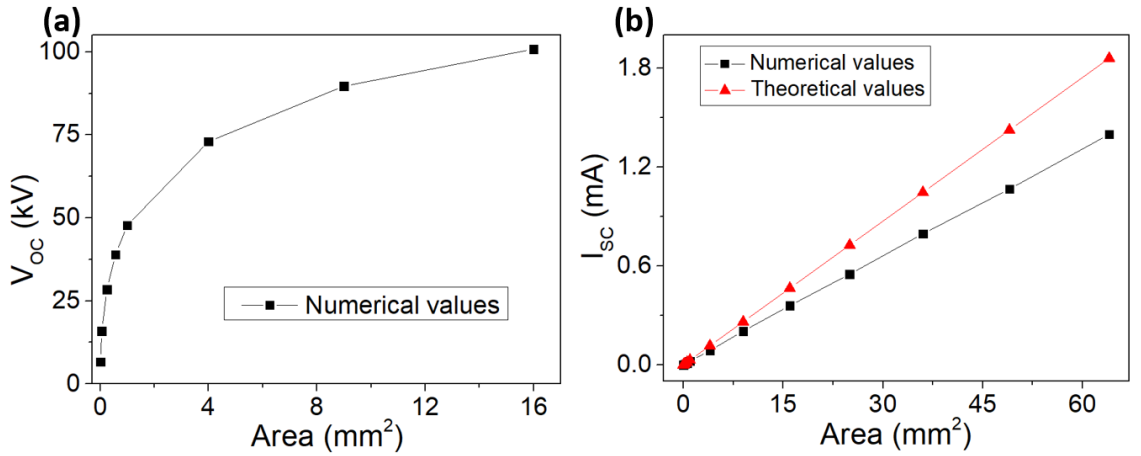

FIGURE 4.8: **(a)** V_{OC} and **(b)** I_{SC} as a function of the TENG's area.

The results of the V_{OC} and the I_{SC} are present in Fig. 4.8. Figure 4.8(a) show that V_{OC} increases non-linearly with the area. These results do not match Niu's model predictions because the model predicts a constant V_{OC} with the area variation. The reason for this is that the value of the area is not considerably larger than the maximum distance between tribopairs. With this, Gauss's law, which is the basis of Niu's model, is not valid. The consequence is that, as the area decreases, the local electrical fields deviate from the perpendicular direction with respect to the plane of the TENG, causing the V_{OC} decrease observed. A possible explanation for the increase of the V_{OC} with the area in a shape that is converging to a value is that the requirements for the Gauss law to be met are increasing with the area, where more local electrical fields are perpendicular to the TENG, as seen in Fig. 4.9.

In Fig. 4.8(b), the results show that the I_{SC} is directly proportional to the area. Compared with Eq. (2.11), the results obtained are in agreement with the V-Q-x relation of the TENG.

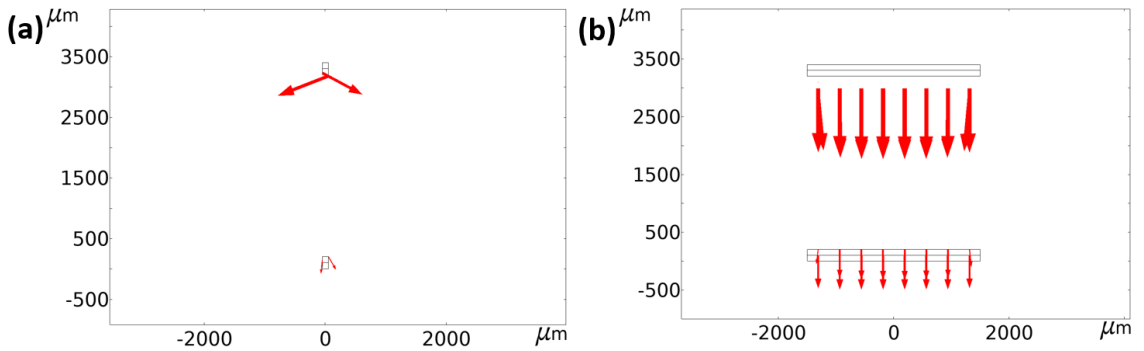

FIGURE 4.9: Electrical field for two different areas when both plates are the furthest apart. [**(a)** 0.01 mm^2 and **(b)** 9 mm^2].

4.3.2 Optimum resistance region

Studying the effect of the area for a range of resistance covering the three main regions (Fig. 4.10), we observe an increase of the voltage and decrease of the current with the increase of the load resistance. The three regions of operation of the TENG operation regions are in agreement with Niu's model, with the voltage having a low value at low load resistance and a high value and constant at high load resistance (and vice-versa for the current).

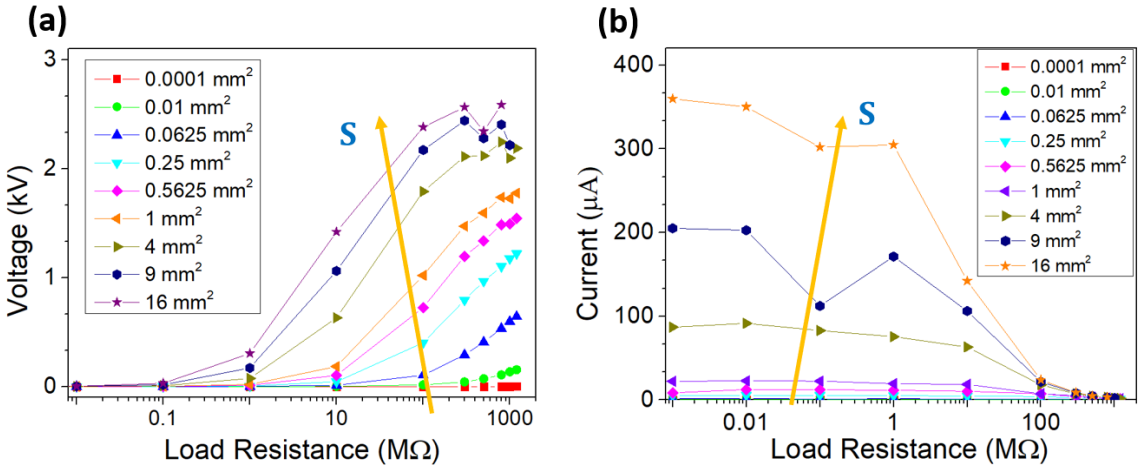

FIGURE 4.10: **(a)** Voltage and **(b)** current as a function of the load resistance for different areas (S).

From Fig. 4.10, it is also observed that the voltage and the current increase with the TENG area.

Figure 4.11(a) shows the power density (power-to-area ratio) for an easier comparison between area values. As predicted by the Niu's model of the contact-separation TENG, the power density increases with the area. Furthermore, we observe a shift to the left (lower load resistances) of the power maximums as the area increases, indicating that the optimum resistance decreases with the area.

Figure 4.11(b) further confirms the inverse relation between area and optimum resistance. Furthermore, the power density increases with the TENG, with a maximum output of 12 mW/mm^2 for the areas values of 9 and 16 mm^2. An important remark is that the minimum distance was used for the calculations of the theoretical values of the optimum resistance and not the maximum as indicated in Eq. (2.13) due to the latter being two orders of magnitude higher than the numerical values. Still, in terms of tendencies, both sets of values are in agreement.

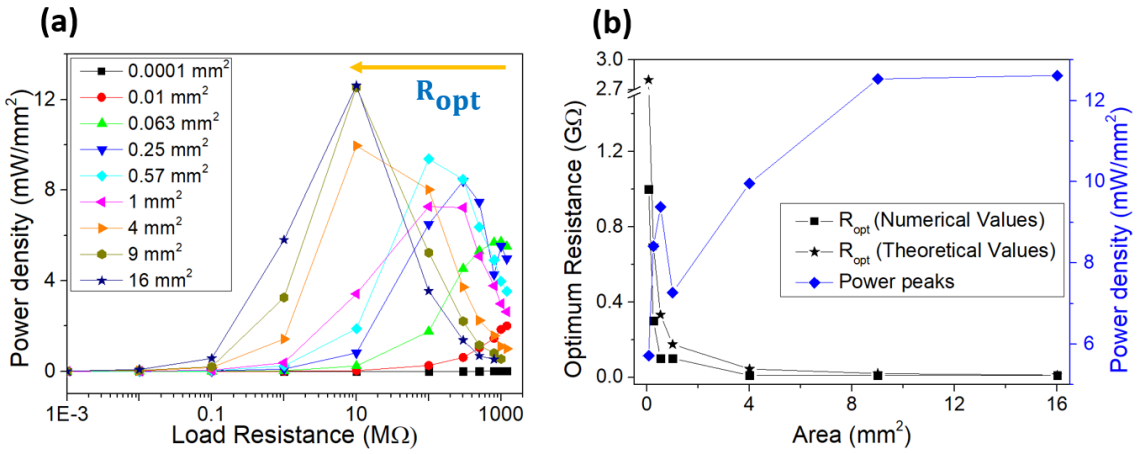

FIGURE 4.11: **(a)** Power density as a function of the load resistance for different areas. **(b)** Optimum resistance as a function of the area.

4.4 Effect of nylon thickness

In this study, we varied the nylon thickness from 25 µm to 1.5 mm. The load resistance values were the same as used previously, except for the 1 and 1.2 GΩ due to a divergence in the COMSOL results.

4.4.1 Open circuit and short circuit regions

A load resistance of 100 Ω was used to conduct the I_{SC} study, while a 100 TΩ was used to study the V_{OC}.

In Fig. 4.12, the increase of nylon thickness causes a decrease in the I_{SC} numerical values, which agrees with the theoretical values for the current that were obtained with Eq. (2.11) with a x(t) of 21.38 µm. By comparing the numerical and theoretical values, the good agreement with the TENG model is confirmed. The larger difference between both sets of values for smaller values of thickness is related with the relatively large relative tolerance used (0.22).

The V_{OC} was found to decrease with the nylon thickness (Fig. 4.12), while Niu's model predicts that it should remain constant. As in the study of variation of the area, one believes that the Gauss law is not valid during these simulations due to the area being of the same order of magnitude as the distance between planes. This implies that, with the increase of the thickness, the local electrical fields deviate from the perpendicular direction of the tribopair plane in the exterior regions (Fig. 4.13), because the maximum distance between materials is maintained with the increase of the thickness, but the distance between electrodes increases, causing the decrease in V_{OC}.

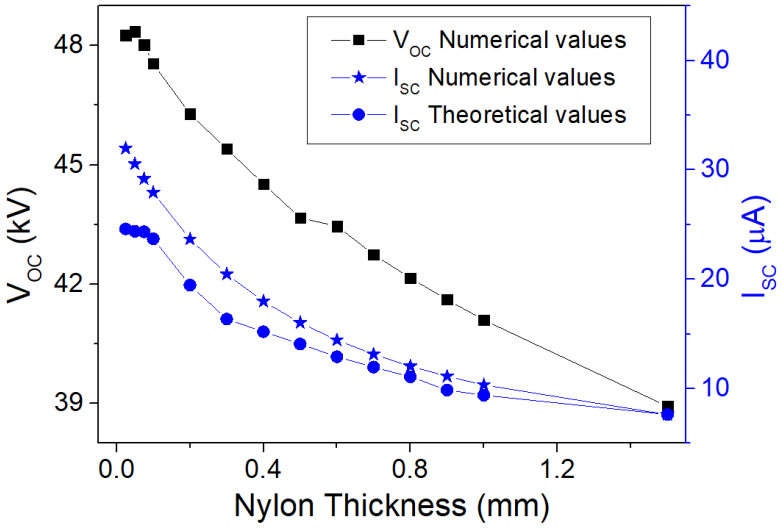

FIGURE 4.12: V_{OC} and I_{SC} as a function of the nylon thickness.

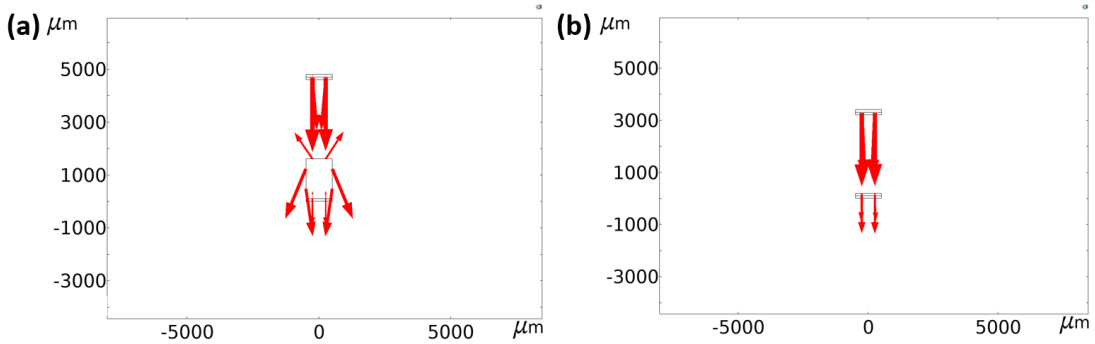

FIGURE 4.13: Electrical field for nylon thicknesses of **(a)** 1.5 mm and **(b)** 0.1 mm.

4.4.2 Optimum resistance region

Figure 4.14 shows the results for the voltage and current as a function of the load resistance. Both graphs are in agreement with Niu's model of the contact-separation TENG for the three regions. One notes that the current increases with the decrease of the nylon thickness, while the voltage increases with the increase of the nylon thickness.

With a maximum output of 10.69 mW/mm^2 at a thickness value of 0.2 mm, the maximum of power [Fig. 4.15(a)] diminishes as the nylon thickness increases. There is a shift to the right on the peaks [Fig. 4.15(b)], indicating that, the optimum resistance increases with the increase of the thickness, which, in therms of tendency, is also in agreement with Niu's model. An important thing to note in Fig. 4.15(b) is that the theoretical [calculated using Eq. (2.13) in section 2.3] use the minimum and not the maximum distance between materials planes, as the Niu's model for the contact-separation mode TENG indicates. If the maximum distance was used, the theoretical values would differ by two orders of

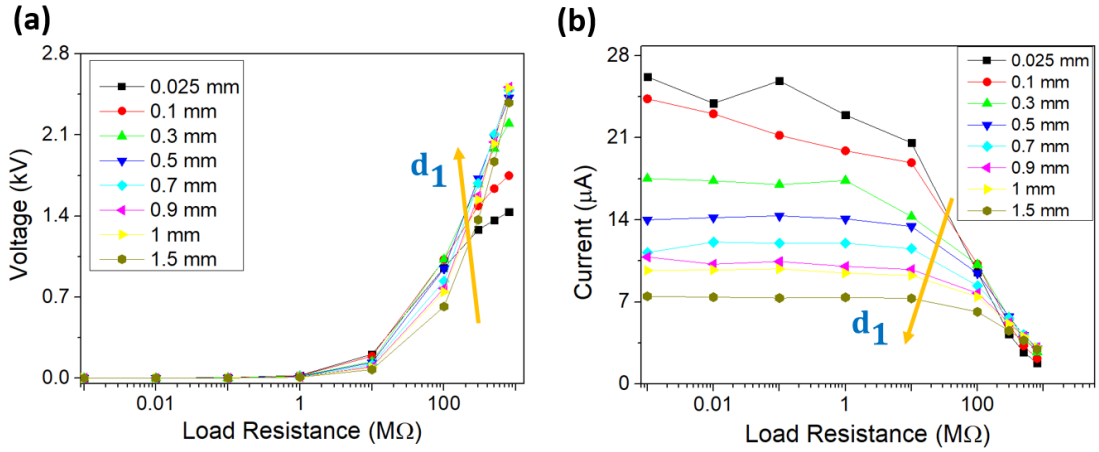

FIGURE 4.14: **(a)** Voltage and **(b)** current as a function of the load resistance for different nylon thicknesses (d_1).

magnitudes of the numerical values. Still, the same tendency of the results can be observed, despite the characterization of the load resistance being discrete on the numerical simulations, with a low quantity of values used.

The maximum power obtained [Fig. 4.15(b)] starts by increasing with the nylon thickness but decreasing afterwards.

The initial increase is due to the lower values of thickness not having the precision needed in the numerical simulations because of the relative tolerance. The drop in power is the expected outcome due to the current decreasing, which outweighs the increase in voltage, as predicted by Niu's model.

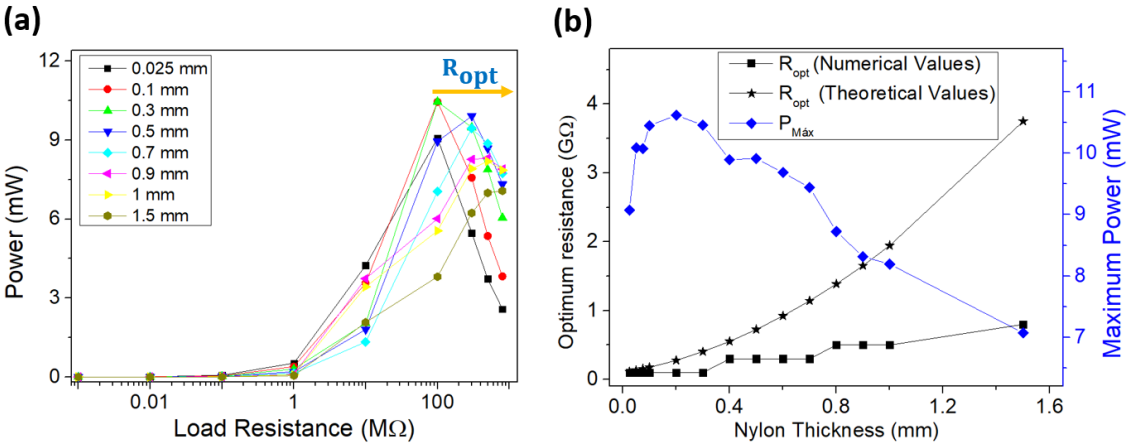

FIGURE 4.15: **(a)** Power as a function of the load resistance. **(b)** Optimum resistance as a function of the nylon thickness.

4.5 Impact of relative permittivity

The study of the evolution of the effect of the relative permittivity on the TENG output is divided into four parts. Firstly, the parameters for the concentration of nanoparticles and the equivalent effective relative permittivity ($\varepsilon_{r_{eff}}$) as well the radius of the nanoparticles are described. Secondly, the comparison of a PDMS doped with nanoparticles (that will be here referred with subscript NP) ($PDMS_{NP}$) and a "PDMS" with the equivalent effective relative permittivity ($PDMS_{\varepsilon_{eff}}$) [with Eq. (2.19)] is performed. As the results will do not match, we then introduced a charge correction dependence on the ε_r. Finally, the V_{OC} and the I_{SC} will be studied with and without the proposed charge correction.

4.5.1 Relative permittivity numerical simulations

In the numerical simulations, it was determined whether the results and tendencies with increasing concentration of NP or $\varepsilon_{r_{eff}}$ were the same for $PDMS_{NP}$ and $PDMS_{\varepsilon_{eff}}$ samples. Two materials were selected for NP and they are: Strontium Titanate ($SrTiO_3$) with a ε_r of 300 [25] and Barium Titanate ($BaTiO_3$) with a ε_r of 1976 (COMSOL). To simulate the concentration of particles, two sizes of particles were used. The particle size used for the Strontium Titanate, and the Barium Titanate had a radius of 15 µm.

Concentration $SrTiO_3/BaTiO_3$	$SrTiO_3$ $\varepsilon_{r_{eff}}$	$BaTiO_3$ $\varepsilon_{r_{eff}}$
0.7%	4.9	16.7
1.4%	7.0	30.7
2.8%	11.1	58.6
4.2%	15.4	86.5
5.7%	19.6	114.3
7.1%	23.8	142.3
8.5%	28.0	170.2

TABLE 4.1: List of the $\varepsilon_{r_{eff}}$ according to the concentration of NP of the respective material.

On Table 4.1, the values for the $\varepsilon_{r_{eff}}$ and nanoparticle concentration are represented.

4.5.2 Open circuit and short circuit regions

The I_{SC} (Fig. 4.16) and V_{OC} (Fig. 4.17) results obtained with a constant surface charge density show that the difference between $PDMS_{NP}$ and $PDMS_{\varepsilon_{eff}}$ samples is not significant (note the scales) because the relative tolerance (0.22) is high enough to make the variation of the results within the variability range. Still, the results show practically no

variation for the V_{OC} and I_{SC}, which is in agreement with Niu's model [see Eqs. (2.11) and (2.12) in section 2.3].

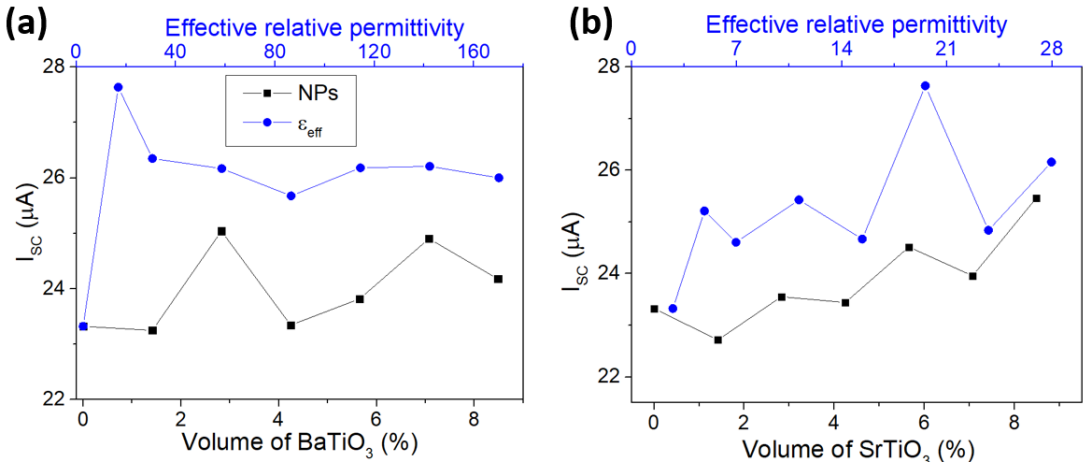

FIGURE 4.16: I_{SC} as a function of the concentration of NP on the PDMS (black) and $\varepsilon_{r_{eff}}$ (blue) for **(a)** Barium Titanate and **(b)** Strontium Titanate.

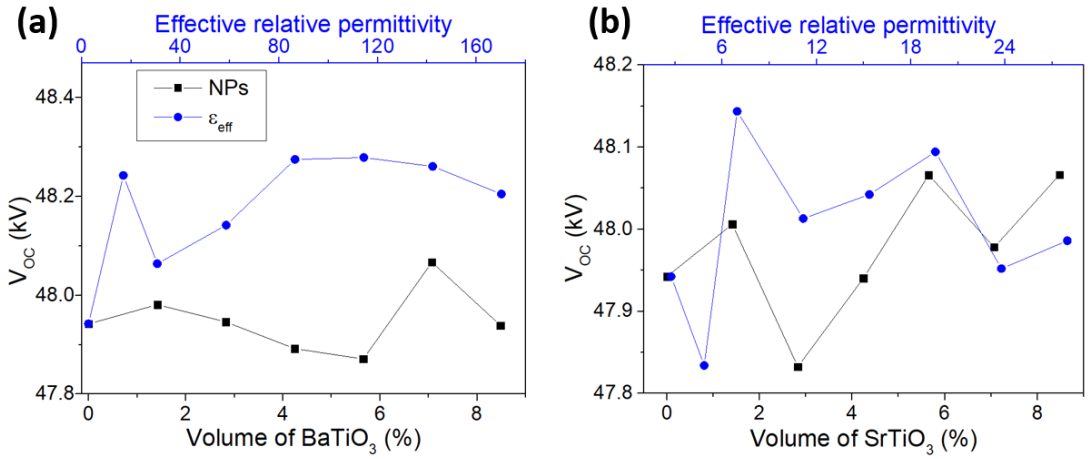

FIGURE 4.17: V_{OC} as a function of the concentration of NP on the PDMS (black) and $\varepsilon_{r_{eff}}$ (blue) for **(a)** Barium Titanate and **(b)** Strontium Titanate.

4.5.3 Comparison of both processes in the transition region

Starting with Barium Titanate NP [Fig. 4.18(a),(b)], the voltage increases with the load resistance while the current decreases, which is in agreement with Niu's model. As the concentration of NP and ε_r increase, both studies do not match because the voltage decreases, with both studies having different tendencies, while the current decreases for $PDMS_{\varepsilon_{eff}}$ samples and increases for $PDMS_{NP}$ samples.

In Fig. 4.19, we observe that the power tends to decrease with the increase in concentration or ε_r and the comparison between NP and $\varepsilon_{r_{eff}}$ does not match.

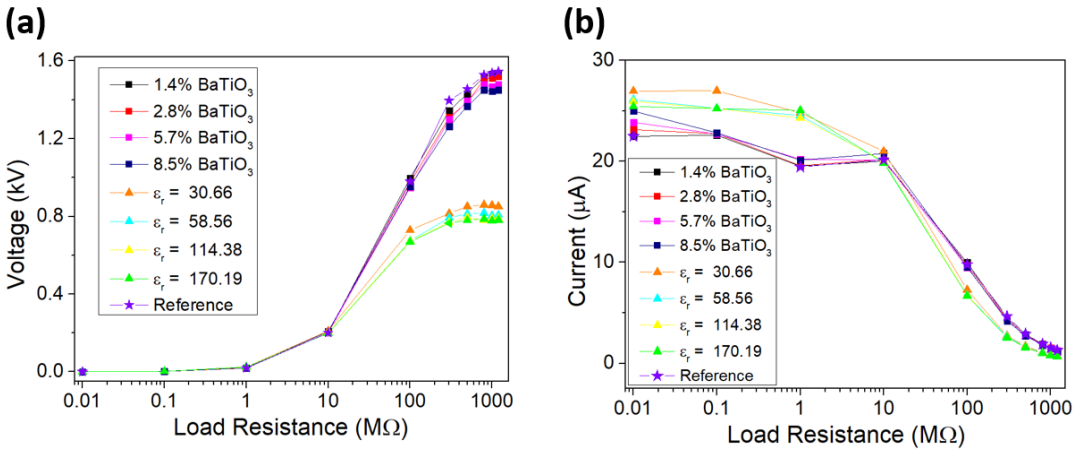

FIGURE 4.18: **(a)** Voltage and **(b)** current as a function of the load resistance. Both graphs compare the results for PDMS_{NP} and $\text{PDMS}_{\varepsilon_{eff}}$ samples.

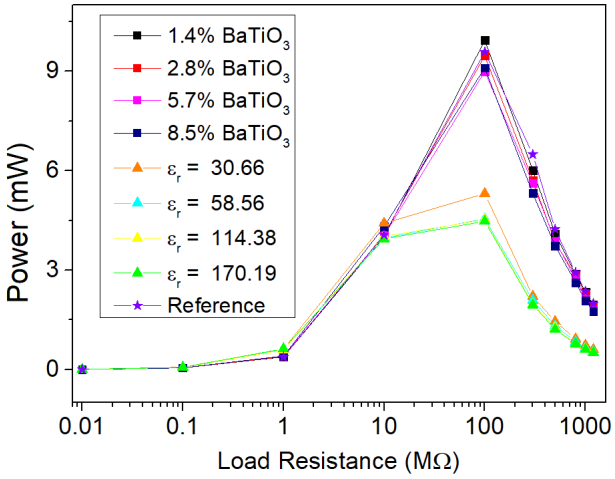

FIGURE 4.19: Power as a function of the load resistance for the PDMS_{NP} and $\text{PDMS}_{\varepsilon_{eff}}$ samples.

For higher ε_r, the voltage, current, and power tend to stabilise. However, at lower ε_r there is an abrupt change in the obtained values, so, to study that region, NP with a smaller ε_r ($SrTiO_3$) were used.

One can observe that the voltage for PDMS_{NP} and $\text{PDMS}_{\varepsilon_{eff}}$ samples differ [Fig. 4.20(a)]. However, with a lower ε_r compared with $BaTiO_3$ NP, the $\text{PDMS}_{\varepsilon_{eff}}$ results show a clearer decrease compared with Fig. 4.18(a) of the voltage is observed with the ε_r increase, which agrees with Niu's model predictions. As for the current [Fig. 4.20(b)], the same behaviour seen in Fig. 4.18(b) is observed.

The slower decrease in power is also observed in the power graphics (Fig. 4.21). Figures 4.20(a) and 4.21 show that with a lower ε_r, one is able to observe the decay of the voltage and power with the $\varepsilon_{r_{eff}}$ increase before that value is high enough that it becomes

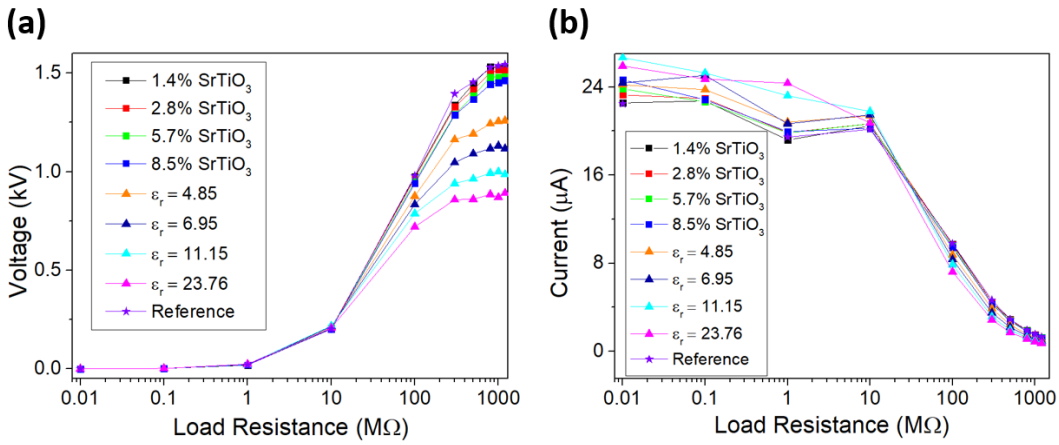

FIGURE 4.20: **(a)** Voltage and **(b)** current as a function of the load resistance. Both graphs compare the results for PDMS_{NP} and $\text{PDMS}_{\varepsilon_{eff}}$ samples.

negligible compared with nylon ε_r (4), according to Niu's model V-Q-x relation Eq. (2.7).

In conclusion, the results of the PDMS_{NP} do not match those of the $\text{PDMS}_{\varepsilon_{eff}}$ sample. Regardless, the $\varepsilon_{r_{eff}}$ tendencies for $\text{PDMS}_{\varepsilon_{eff}}$ sample agrees with the theoretical predictions. Since experiments (Ref. [25]) show a clear relation between voltage, current, and power with the increase of the ε_r, the surface charge density has an indirect relationship with the ε_r, so that a charge correction will be proposed in the next subsection.

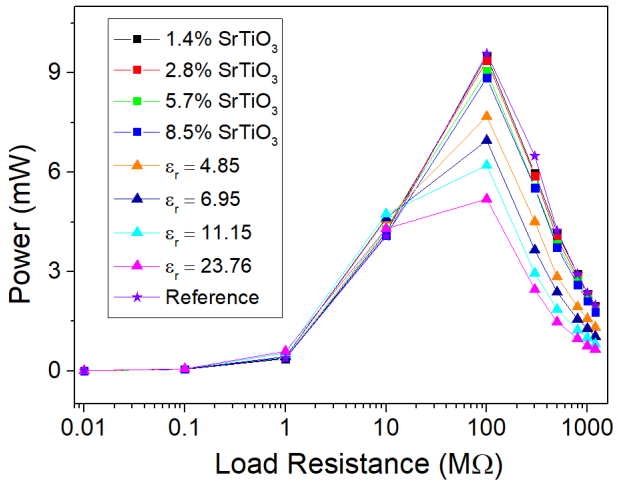

FIGURE 4.21: Power as a function of the load resistance for the PDMS_{NP} and $\text{PDMS}_{\varepsilon_{eff}}$ samples.

4.5.4 Inserting a charge density correction dependent on the relative permittivity

To perform a charge correction based on results in the Ref. [25], we modelled the TENG as a parallel plate capacitor with one or two dielectric mediums in between. Since

we change the ε_r of only one of the materials, let us consider only that one, represented in Fig. 4.22.

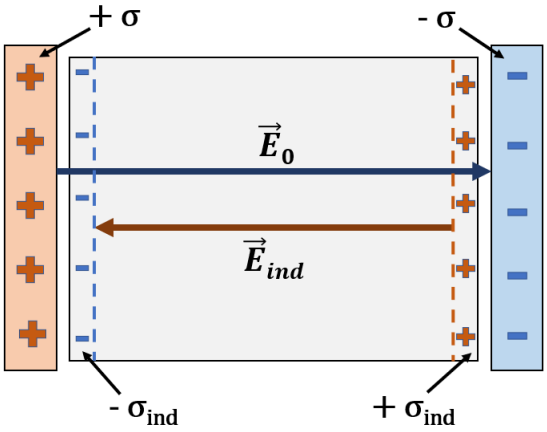

FIGURE 4.22: Two electrodes with opposing total surface charge density and the dielectric medium. The induced surface charge density varies with the ε_r. At the borders of the dielectric with the electrodes, the dielectric material reaches a charge equilibrium with each electrode.

The electrodes produce a field in one direction, and the dielectric medium creates an opposing electric field due to the induced charges on the surface being the opposite of the electrode in contact. Thus, the total electrical field (E_{total}) is given by[69]:

$$E_{total} = E_0 - E_{ind}, \tag{4.2}$$

with E_0 the electric field in vacuum and E_{ind} the induced electric field of the PDMS. The electric fields can be replaced as:

$$\frac{\sigma}{\varepsilon_0 \varepsilon_{r_{eff}}} = \frac{\sigma}{\varepsilon_0} - \frac{\sigma_{ind}}{\varepsilon_0}, \tag{4.3}$$

where σ is the total surface charge density and σ_{ind} the surface charge density induced on the materials. And this can be rearranged as [69]:

$$\sigma_{ind} = \sigma \left(\frac{\varepsilon_{r_{eff}} - 1}{\varepsilon_{r_{eff}}} \right). \tag{4.4}$$

If $\varepsilon_{r_{eff}}$ tends to infinite, Eq. (4.4) tends to the charge reference value of 6×10^{-4} Cm^{-2}, which is the same value used in the reference sample simulation. Since we want σ_{ind} of the reference sample to give 6×10^{-4} Cm^{-2}, using Eq. (4.4) with $\varepsilon_{r_{eff}}$ = 2.75 gives σ_{ind} = 3.82×10^{-4} Cm^{-2}, which has a difference of 2.18×10^{-4} Cm^{-2} (σ_{diff}) to the charge reference value. Adding this to Eq. (4.4) gives:

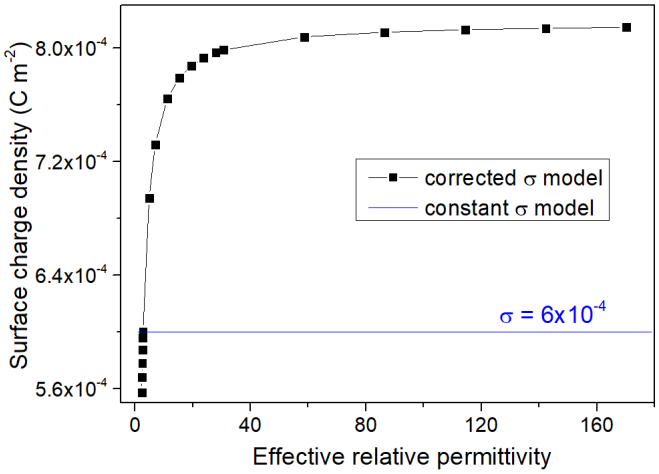

FIGURE 4.23: Surface charge density as a function of $\varepsilon_{r_{eff}}$.

$$\sigma_{ind} = \sigma\left(\frac{\varepsilon_{r_{eff}} - 1}{\varepsilon_{r_{eff}}}\right) + \sigma_{diff}. \tag{4.5}$$

Figure 4.23 shows the difference between a constant charge value and the corrected value, according to Eq. (4.5). It is observed that below PDMS ε_r (2.75), the corrected charge is inferior to the constant one and vice-versa above PDMS ε_r.

Let us now analyse how this correction affects our results In Fig. 4.24(a), the voltage increases at low $\varepsilon_{r_{eff}}$ values and low load resistances and we see that decreases at high load resistances. As for the current in Fig. 4.24(b), a large increase is observed at lower load resistances and lower $\varepsilon_{r_{eff}}$. For both graphs, at higher $\varepsilon_{r_{eff}}$, the values stabilise.

The charge correction improved the power results (Fig. 4.25), particularly at higher $\varepsilon_{r_{eff}}$, raising them well above the constant charge cases in the preceding subsection. An

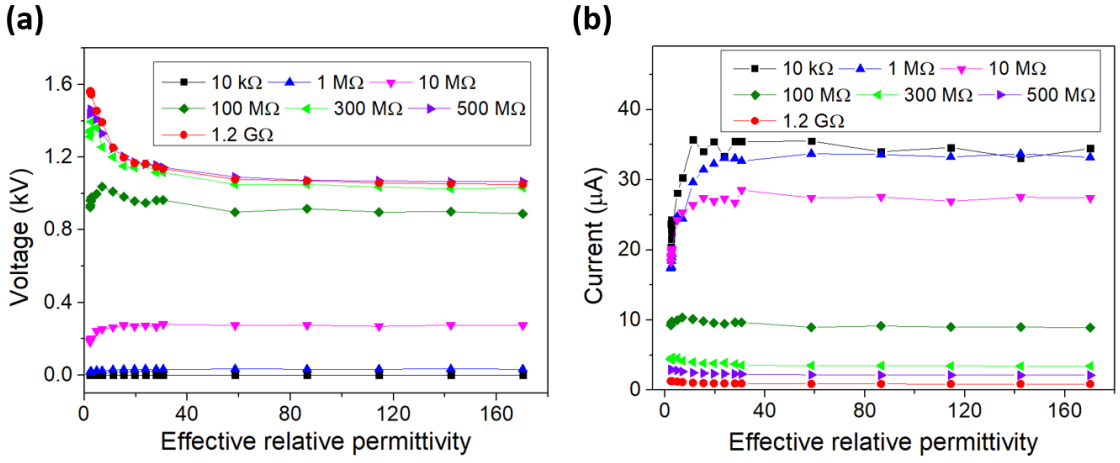

FIGURE 4.24: **(a)** Voltage and **(b)** current as a function of the $\varepsilon_{r_{eff}}$ for a set of values of load resistance.

interesting occurrence to notice is that the power for the 10 MΩ load resistance in Fig. 4.25(b) has a significant increase with the ε_r compared with Figs. 4.19 and 4.21.

To understand this, we must take a particular look at voltage, current and power figures. For when the contact-separation mode comes into contact, the V-Q-x relation [Eq. (2.7) in section 2.2.1.1] could be written as:

$$V = -\frac{Q}{S\varepsilon_0} d_0. \tag{4.6}$$

However, since the minimum distance between the triboelectric materials is only one order of magnitude below the corresponding thicknesses, the parameter x(t) cannot be neglected. This means that Eq. (4.6) is not valid for this case. If the current is calculated through Eq. (2.7):

$$I = -\frac{Q}{RS\varepsilon_0}\Big(d_0 + x(t)\Big) + \frac{\sigma x(t)}{R\varepsilon_0}. \tag{4.7}$$

Equation (4.7) illustrates the dependence on the load resistance on both terms of the equation, one with the charge on the electrode (Q) and the other with the surface charge density (σ). Having two terms on the equation, two behaviours will occur, one at low load resistances and one at high load resistances. In Fig. 4.26, the charge variation on the nylon's electrode can be observed. As expected, the charge decreases when the minimum distance is reached, not achieving zero because there is no actual contact. With the increasing load resistance, the current decreases and the electrode that is charge saturated will have more difficulty getting out of this state.

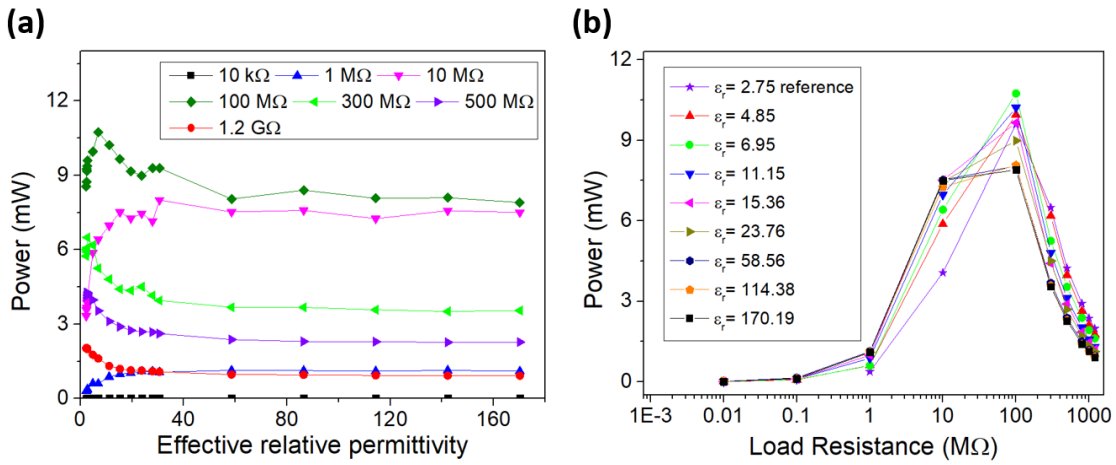

FIGURE 4.25: Power as a function **(a)** of the $\varepsilon_{r_{eff}}$ and **(b)** the load resistance.

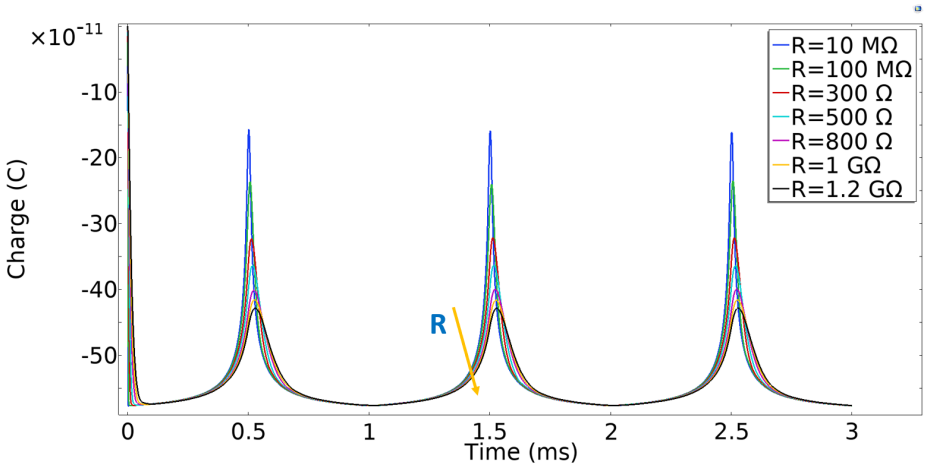

FIGURE 4.26: Charge at the nylon's electrode as a function of the time. The various curves are the different load resistances used.

Observing Eq. (4.7), with a low load resistance and at the minimum distance between surfaces, the surface charge density outweighs the charge in the electrodes because the charge transfer in the electrodes brings the electrode charge closer to zero, making that term of the equation negligible. At a load resistance above the maximum power output (100 MΩ), the electrodes barely get out of the saturated state, meaning the charge on the electrodes term of the Eq. (4.7) will outweigh the surface charge density term. The previous statements explain the power increase for a 10 MΩ in Fig. 4.25.

This effect also happens in all simulations where the surface charge density is constant. However, it is more noticeable in this study due to the surface charge density term varying on Eq. (2.7) that has a large impact for lower load resistances.

4.5.5 Comparison with and without the charge correction

Figure 4.27 presents both numerical and theoretical values for the corrected and constant σ methods. We observed that I_{SC} increases with the introduction of the charge correction. At higher ε_r values, both theoretical and numerical values stabilise. The tendencies of both corrected and constant charge models are in in agreement. At lower ε_r, the I_{SC} increase is larger both surface charge density corrected models compared with the constant surface charge density models. This is expected, since Eq. (4.4) has a larger variation on the charge value at lower ε_r.

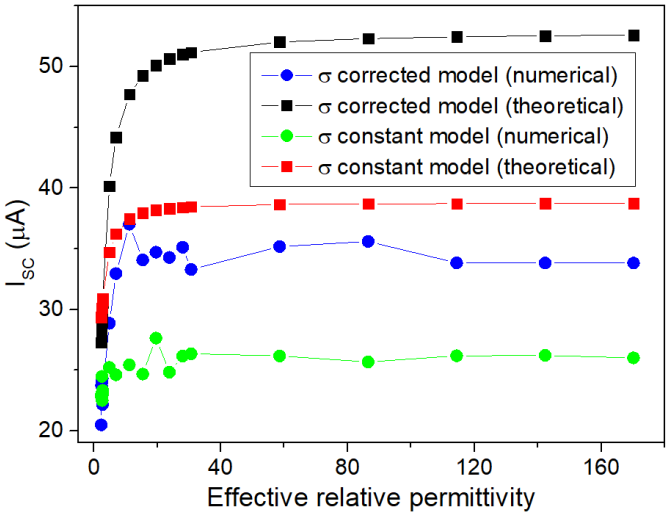

FIGURE 4.27: I_{SC} as a function of $\varepsilon_{r_{eff}}$.

Analysing Fig. 4.28, the maximum power is enhanced if the surface charge density is higher than the reference value. Since the power decreases with the increase of the ε_r (for a constant charge), adding the charge correction, one must consider two factors. The first is that the surface charge density increases with the ε_r and this increases the power. The other is that with the increase in the ε_r, the power decreases. These different tendencies result in: until around 10 ε_r, the increase in the surface charge density surpasses the decrease in power caused by the increase in the ε_r. Between ε_r of 10 and 60, the decrease of the power with ε_r outweighs the surface charge density increase, causing the overall decrease of power. At a ε_r higher than 60, the value is too high compared to the nylon's ε_r

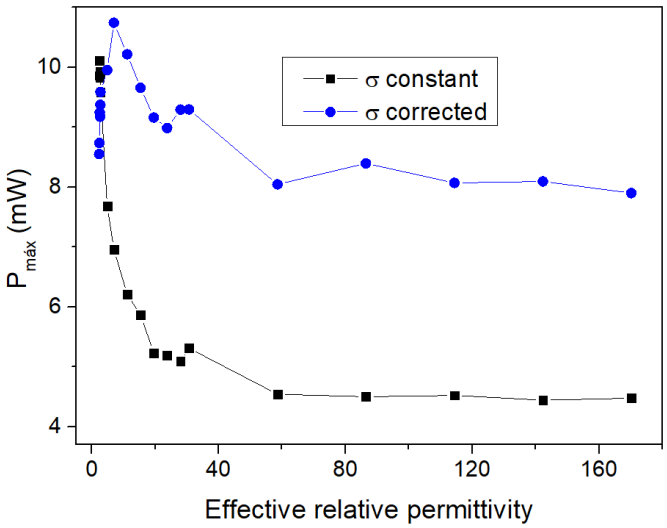

FIGURE 4.28: Maximum power as a function of $\varepsilon_{r_{eff}}$.

(4), meaning that the PDMS$_{\varepsilon_{eff}}$'s ε_r is negligible. Also, the charge correction equation [Eq. (4.4)] gives a constant maximum power for high values of ε_r.

The study of the optimum resistance was not conducted here because the numerical simulations were only performed for 10 load resistance values to characterise the three regions of the TENG. In fact, according to Eq. (2.13), the variation of the optimum resistance with the ε_r is small. Thus, values of load resistance very close apart would be needed to execute this study.

In Fig. 4.29, the theoretical and numerical values for the V_{OC} do not match in terms of values; nevertheless, they are in agreement in terms of tendencies. Since V_{OC} is directly proportional to the surface charge density, meaning that the voltage will follow the same trend as the charge.

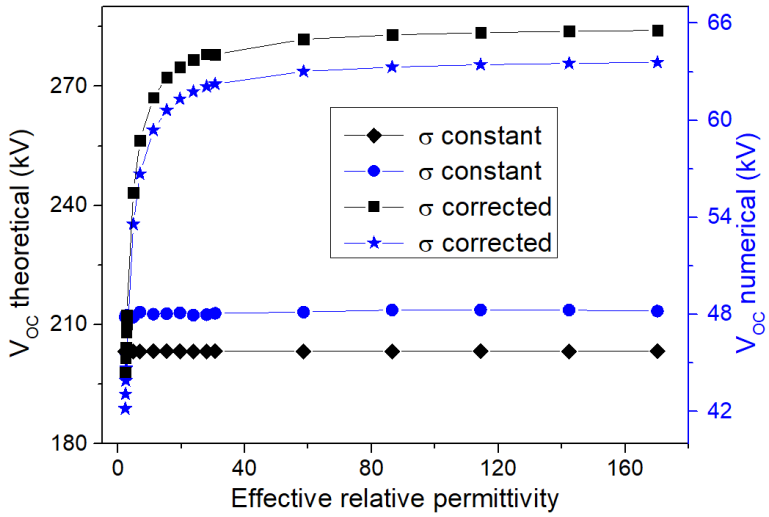

FIGURE 4.29: V_{OC} as a function of $\varepsilon_{r_{eff}}$.

Considering the second method of measuring the V_{OC} in which we use a load resistance of 55 GΩ and perform 8 cycles to guarantee a stable value. This is observed in Fig. 4.30, where the seventh and eighth peaks show that the V_{OC} is stabilised. As expected, there is an increase in the V_{OC} with the charge correction applied. However, V_{OC} decreases in both cases of charge with the increase of the ε_r, which is in disagreement with the tendency of the 100 TΩ V_{OC} study (Fig. 4.29) .

This disagreement is due to the electrodes' being slowly saturating and not being close to zero charge, as should be verified. Figure 4.31 represents the evolution of the charge in one of the electrodes. This saturation and stabilisation of the charge value makes the charge Q parameter completely outweigh the surface charge density σ parameter in Eq.

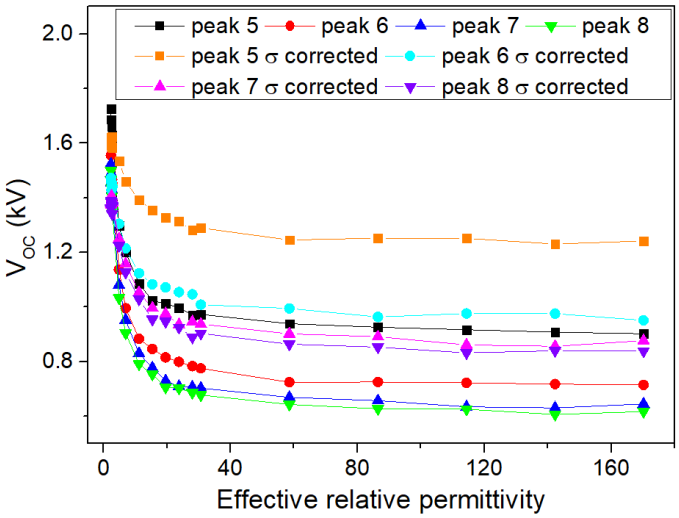

FIGURE 4.30: V_{OC} as a function of the $\varepsilon_{r_{eff}}$. The peaks represented are the ones for which V_{OC} seems to stabilise.

(2.7). Therefore, a decrease in the voltage is expected with the increase of the ε_r, which agrees with the numerical values. For the 100 TΩ load resistance, the charge measured is around 10^{-13} C which is negligible compared to the saturation values of around 10^{-10} C seen in Fig. 4.31.

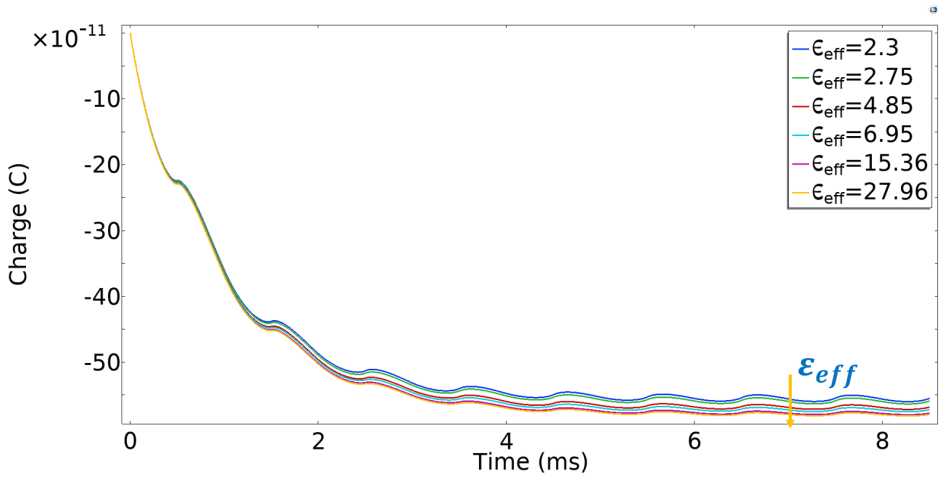

FIGURE 4.31: Charge in the electrode with nylon on top for different $\varepsilon_{r_{eff}}$.

In conclusion, a higher load resistance would be needed to make the charge negligible compared to the saturation value. However, more cycles would then be necessary for the stabilisation to occur, which means a larger time simulation and memory occupancy, making this method not viable.

Chapter 5

TENG's temperature study

This chapter will be split into four sections. In the first section, the process prior to the temperature study, the charging process of a sample is discussed and compared between different thicknesses of PDMS samples and also a PDMS nanoparticle-doped sample. Next, the analysis of a single 30-second acquisition for voltage and current at room temperature is performed. The study of the increase in temperature with the acquisition of the voltage and current is discussed and compared for the previously mentioned samples. Finally, a discussion about potential issues or changes that worsen or improved TENGs performance. In all these experiments, copper and aluminium samples were used. Since the aluminium sample was used in most of the results compared with the copper one, the results with the copper sample are identified in the graph itself.

5.1 Charging process

Charging a sample's surface to saturation leads to a large initial increase of the V_{OC}, followed by a progressive slowing down until saturation, as seen in Fig. 5.1. The difference between the minimum and maximum voltage values will be explained in the next section.

To observe if the charging process is reproducible, in Fig. 5.2, three data acquisitions were made, with the first and second data collections occurring in the morning and afternoon of the same day, respectively, and the third occurring in the morning of the following day. The variation of TENG performance with temperature was made after each charging process, and the foam was not changed during the entire study, nor was the sample adjusted. The increase from the first acquisition to the following ones is likely due to the

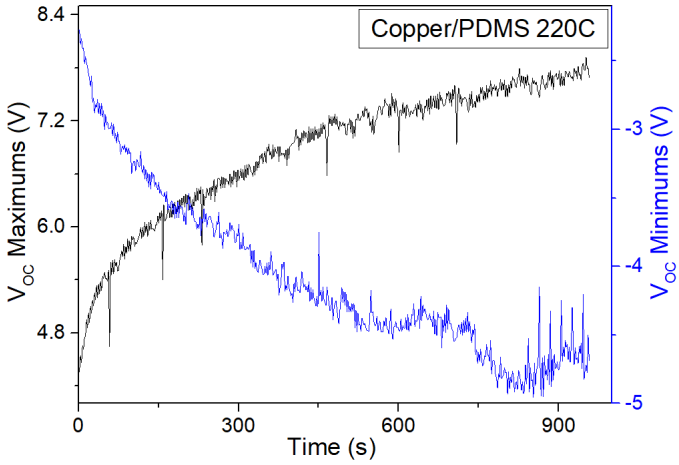

FIGURE 5.1: TENG charging phase at room temperature using PDMS 220C and copper samples.

fact that, at higher temperatures (60 - 110 °C), the PDMS has a curing process and its surface is already charged up for the following experiments. Since PDMS is an insulator, it tends to hold the charge longer, and in the following acquisitions, its charge might not be zero. Also, the second and third data acquisitions are similar, meaning the process is reproducible. To simplify, in the following graphs, only the separation peaks (positive) will be displayed.

The same study was performed for PDMS 220A, PDMS 77A, PDMS 52A, and Nano A samples (Fig. 5.3), all showing two things in common: (i) the performance improves from the first to the second data acquisition, but (ii) it declines from the second to the third. The former is likely due to the fact that the curing and pressing contact in the PDMS may restructure the surface because the mechanical properties of PDMS vary easily with heating. The temperature study in the first acquisition only reaches 60 °C while in

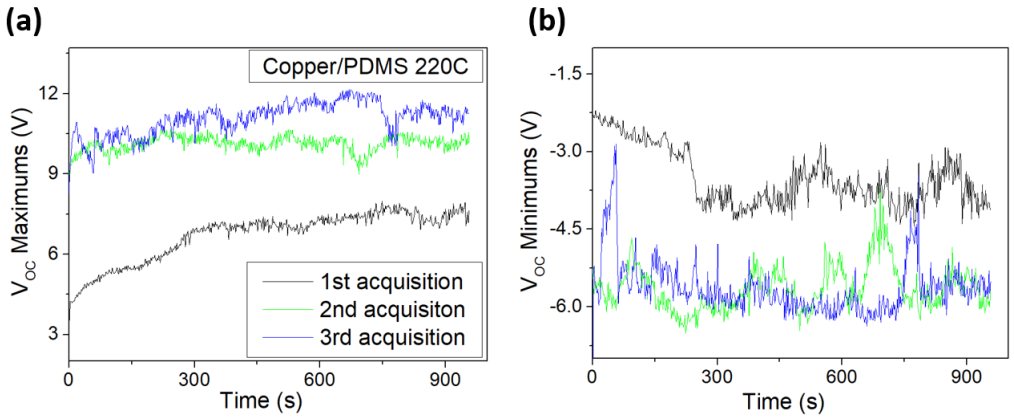

FIGURE 5.2: **(a)** Maximums and **(b)** minimums of TENG charging at room temperature, with PDMS 220C and copper samples carried out at different moments.

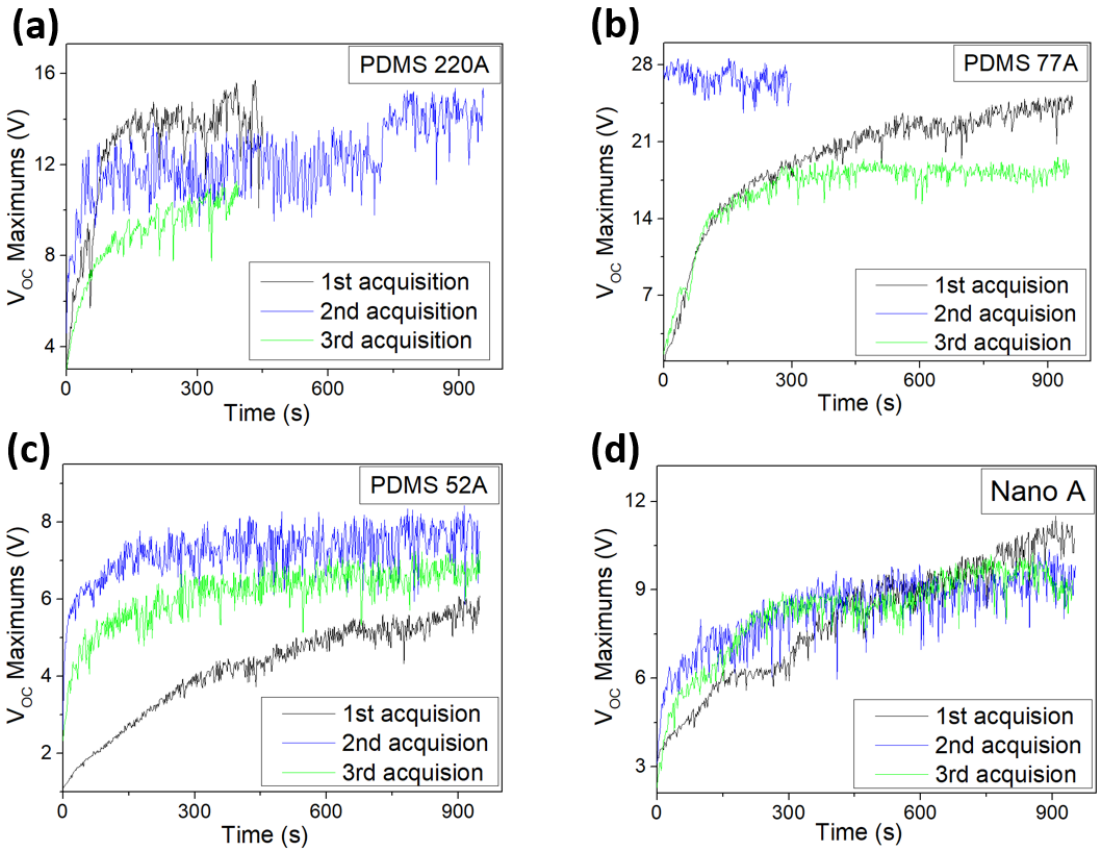

FIGURE 5.3: Three charging operations performed at different times at room temperature using aluminium against PDMS 220A **(a)**, PDMS 77A **(b)**, PDMS 52A **(c)**, and Nano A **(d)** samples.

the second acquisition it reaches 100 $^{\circ}C$, which can translate into higher sample wear. Furthermore, the third acquisition occurs only the next morning, with a larger time gap than between the first to second acquisition, implying that more charge can leave the surface of the sample. All of these factors contribute to the drop in performance of the TENG. According to Niu's model, one would expect an increase in performance from PDMS 220A to PDMS 77A samples and PDMS 77A to PDMS 52A [Figs. 5.3(a)-(c)] since the decrease in thickness should increase the voltage. While the increase from PDMS 220A to PDMS 77A samples was verified, the other one was not.

A remark regarding the results for PDMS 220A and PDMS 77A samples [Figs. 5.3 (a),(b)] that had smaller acquisitions due to the sample falling off (sample PDMS 220A) or the resistance box's power supply not being connected (sample PDMS 77A).

The difference between acquisitions on sample Nano A [Fig. 5.3(d)] is minimal when compared to the other samples, indicating that the mechanical characteristics of $SrTiO_3$

doped PDMS vary less with temperature when compared to simple PDMS samples. Furthermore, it was believed that Nano A would perform better than PDMS 220A, but the opposite occurred.

5.2 Analysing the maximums and minimums obtained

In Fig. 5.4, there is a considerable discrepancy between the current and voltage graphs. The current graphs exhibit sharp peaks, whereas the voltage graphs have contact and separation peaks that decay slowly. The different load resistances used for the I_{SC} (100 Ω) and the V_{OC} (470 MΩ) explain this discrepancy in behaviour. The peaks occur just before the moving sample makes contact with the fixed sample and just after the moving sample separates from the fixed sample. This is where the charge moving is at its peak and when the samples come into contact, the voltage and current should be zero. With this in mind, the decays shown in the voltage graph in Fig. 5.4(a) represent the TENG's transient state, caused by slower charge movement, which leads to a slower decay [29]. Compared to what was observed of the transient state in section 4.2.1, in the experimental setup only the difference between decays is observed, with no difference between instants of contact and peaks. For future experiments, it would be interesting to perform them with higher values of load resistance (for example 10 GΩ) to see if the decay is slower and, despite being much harder to detect if it happens compared to the numerical simulations, the shift of the peaks that would indicate that the instant of contact and of the peak maximums occur do not match.

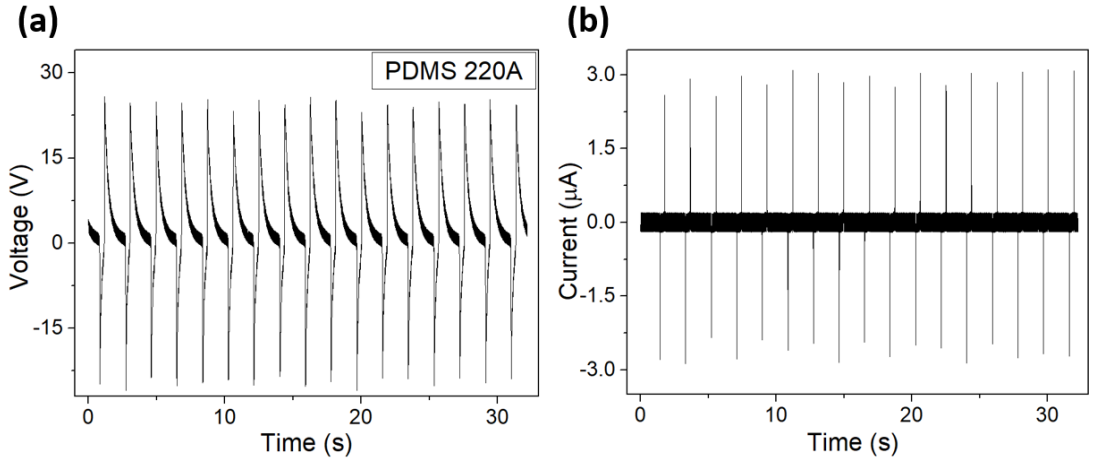

FIGURE 5.4: **(a)** V_{OC} and **(b)** I_{SC} measurements (30 s) of PDMS 220A/aluminium tribopairs at room temperature.

Another important thing to discuss is the peak value asymmetry between maximums and minimums. There are reasons for such asymmetry. According to Ref. [70], there is a difference between the contact and the separation situations, with the contact being affected by the material thickness and the separation affected by the separation distance between materials. Furthermore, Ref. [71] confirmed this asymmetry and discovered that, in addition to the compressing force, there is a distinct separation force. The explanation given was that adhesion between the materials develops during contact and compression due to opposite electrostatic charges on opposing surfaces. This adhesion force is much smaller than the linear motor's force. When the materials separate, they remain adhered to each other, and the PDMS, being more elastic than a metal, is pushed away from its electrode until the adhesion force is outweighed by the separation distance generated between the materials. The sudden separation of materials, which creates the positive force detected by Ref. [71], forces the stretched material to return to its equilibrium shape, influencing the acquired separation peak. In the case of this work's experiment, a foam is employed, which is also a factor to consider in the peak asymmetry.

5.3 Temperature influence on the performance of the TENG

We will start by considering the results comparing the performance of using aluminium or copper as the moving samples against the PDMS 220B sample (Fig. 5.5). Measurements were taken on the same day, using the copper sample in the morning and the aluminium sample in the afternoon.

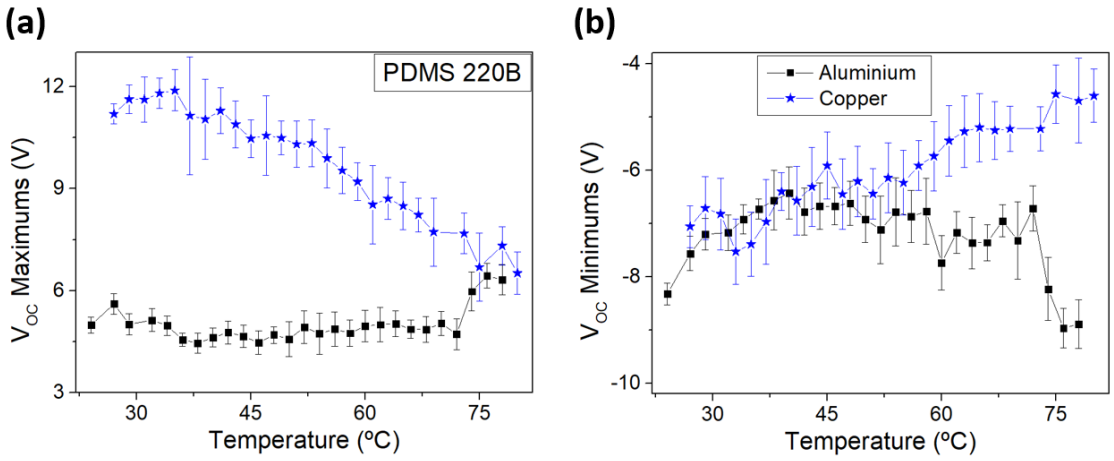

FIGURE 5.5: Voltage **(a)** maximums and **(b)** minimums as a function of the temperature to compare aluminium and copper samples against sample PDMS 220B.

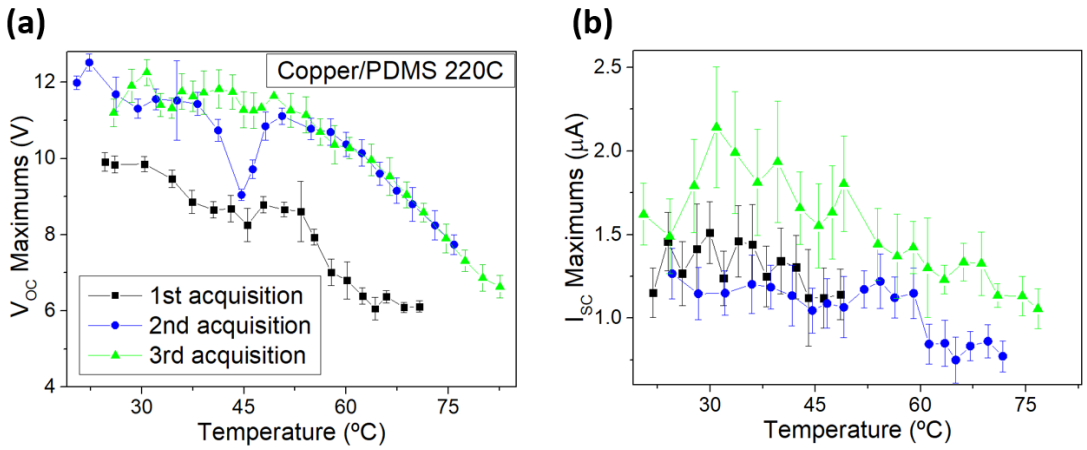

FIGURE 5.6: Average maximums for **(a)** V_{OC} and **(b)** I_{SC} for each temperature value from three acquisitions made for copper and PDMS 220C samples.

The obtained V_{OC} trends with increasing temperature are shown in Fig. 5.5. Both materials have different tendencies. While the aluminium sample maintains the voltage values and rises slightly as temperature rises, the copper sample's performance decreases as temperature increases.

In Fig. 5.6 (for copper/PDMS samples), the voltage and current decrease with increasing temperature with the heating causing a restructuring in the PDMS surface, enhancing the voltage performance, while the current only increased after the third acquisition.

The copper sample was damaged with the break of the wire in the weld region of the sample after the previous data was gathered. Despite the wire being welded again, the performance was poorer following that incident. The aluminium sample was then used for the remainder of the studies. It would be interesting to understand more about the differences in behaviour of copper and aluminium samples.

Starting with PDMS 220A sample, and to emphasise the peak's asymmetry, the maximums and minimums of voltage and current are shown in Fig. 5.7, with both acquisitions made on the same day, one in the morning and one in the afternoon. This acquisition method is valid for the following samples of this section. The maximums and minimums for both voltage and current do not have the same value, and their decrease with temperature differs from each other. V_{OC} and I_{SC} decrease with temperature, however, as shown in Fig. 5.7, V_{OC} increases with temperature in the region of 50 $^{\circ}C$ to 60 $^{\circ}C$. In the first acquisition, the current remained stable until 60 $^{\circ}C$ to 70 $^{\circ}C$ and then increased. The minimums and maximums of the current have a larger value on the second acquisition than on the first. Since it was a new sample, the PDMS started to modify its surface near 60 $^{\circ}C$,

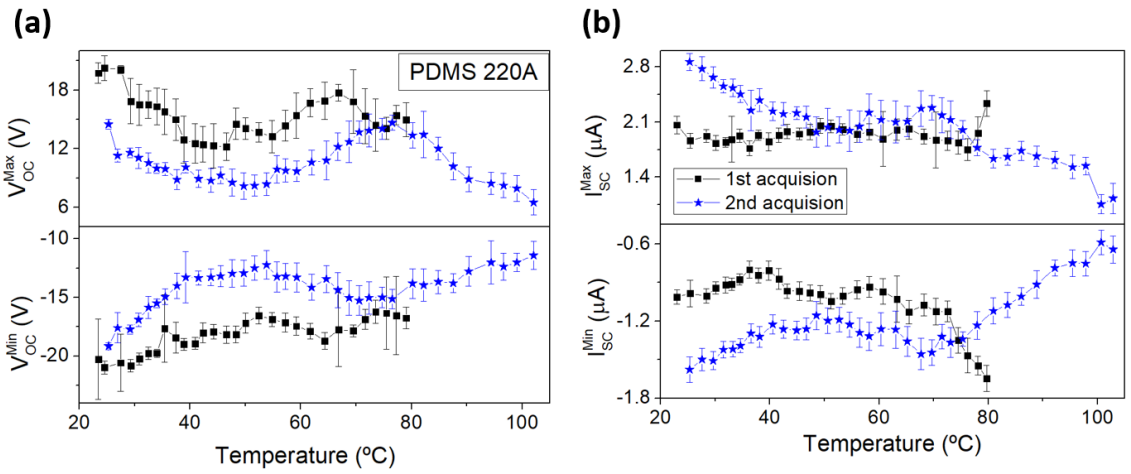

FIGURE 5.7: Average maximums for **(a)** V_{OC} and **(b)** I_{SC} for each temperature value from two acquisitions made for aluminium and PDMS 220A samples.

making it more flexible by having better coverage of the moving sample area, resulting in an increase in performance. The increased current value at low temperatures of the second acquisition compared to the prior one indicates that the PDMS surface properties have altered. However, as the temperature rises, the current values gradually decrease and match the first acquisition at 50 $°C$ to 60 $°C$. Past these values, the current and voltage decrease. The thermal degradation of this sample is seen in Fig. 5.3(a) of section 5.1 by the decrease in performance from the second to the third acquisition.

In the case of the PDMS 77A sample, it is also relevant to see both maximums and minimums due to different behaviours of both. The asymmetry between maximums and minimums peaks is seen in Fig. 5.8, and when compared to PDMS 220A sample, the decrease in PDMS thickness increases the current and voltage, as predicted by Niu's model. Temperatures above 60 $°C$ cause a drop in voltage and current, which is expected because the thermionic effect decreases the available charge in the samples, resulting in a decrease in performance. In Fig. 5.8(b), below 60 $°C$, the current increases in the first acquisition until 50 $°C$ and then drops, but in the second acquisition, the values decrease to levels comparable to the first acquisition at 40 $°C$. This tendency and the fact that there is a significant difference between the first and second acquisitions from room temperature to 40 $°C$ indicate that the PDMS surface has been restructured and could have become more flexible to perform a better coverage of the aluminium sample on impact, maximising the TENG's performance. The improvement in performance from the first to the second acquisition on the voltage [Fig. 5.8(a)] is less than that on the current, but it confirms the prior assertion about the PDMS being restructured for greater coverage of the aluminium

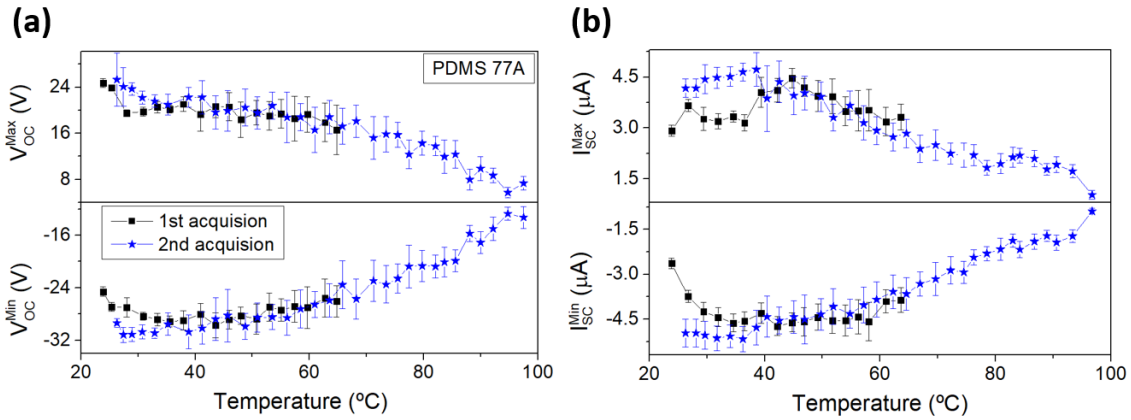

FIGURE 5.8: Average maximums for **(a)** V_{OC} and **(b)** I_{SC} for each temperature value from two acquisitions made for aluminium and PDMS 77A samples.

sample. The slower decay of the minimums relative to the maximums for the voltage from room temperature, as shown in Fig. 5.8(a), could imply that in that temperature range, because PDMS becomes more compressible, the PDMS thickness in compression may decrease sufficiently enough to slow the decay.

For the following samples, only the maximums values will be shown for simplicity, since the tendencies of the maximums and minimums are similar.

In Fig. 5.9, the results for PDMS 52A sample are displayed, and when compared with PDMS 220A and PDMS 77A samples, the results are inferior to both samples. According to Niu's model, the inverse should have occurred. Analysing the tendencies, both the current and voltage maintain a constant value until they reach 55 $^{\circ}C$ to 60 $^{\circ}C$, at which point they begin to drop. In addition, there is no difference between the first and second acquisitions for each parameter. One explanation for this behaviour could be that the

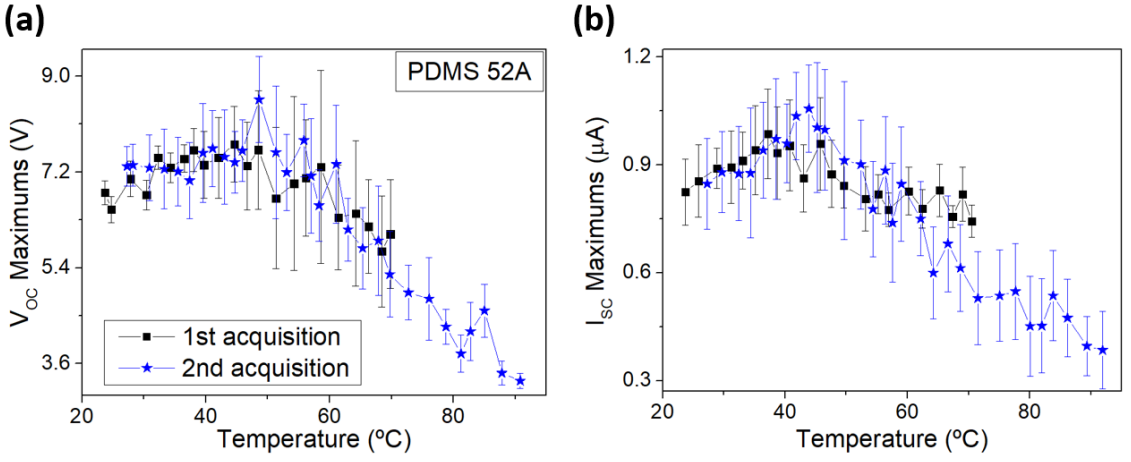

FIGURE 5.9: Average maximums for **(a)** V_{OC} and **(b)** I_{SC} for each temperature value from two acquisitions made for aluminium and PDMS 52A samples.

PDMS's flexibility improves when the temperature rises towards 60 $^{\circ}C$ degrees Celsius, increasing performance. This may be balanced by the thermionic effect, which reduces the TENG's performance.

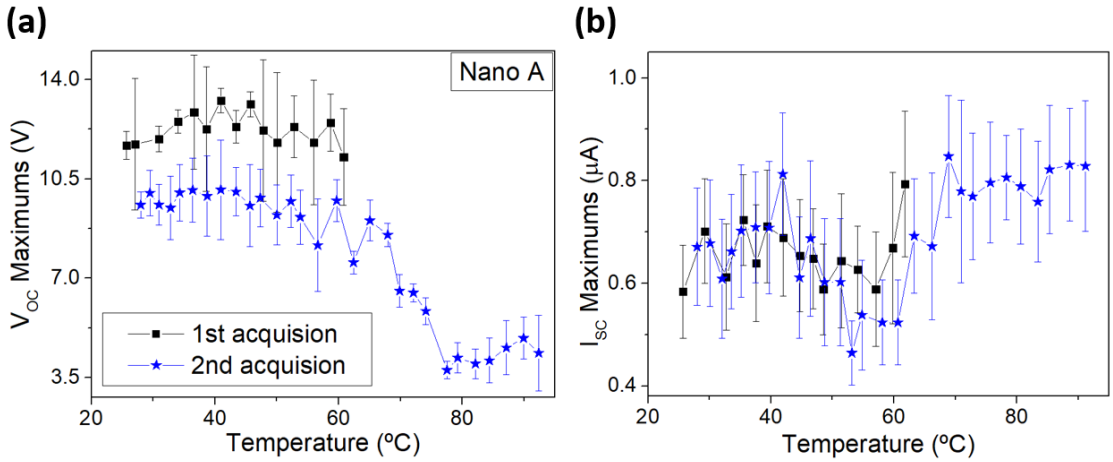

FIGURE 5.10: Average maximums for **(a)** V_{OC} and **(b)** I_{SC} for each temperature value from two acquisitions made for aluminium and Nano A samples.

Comparing Nano A (Fig. 5.10) and PDMS 220A (Fig. 5.7) samples, PDMS 220A outperformed Nano A, which was unexpected. The purpose of the nanoparticle doping was to raise the relative permittivity of the material, hence improving its charge storage capacity and performance. Not only are the results poor, but the voltage performance worsens and the current does not increase from the first to second acquisitions at low temperatures. In terms of tendencies, the voltage decreases while the current remains constant. Because the current value is low, the electrometer is more susceptible to measurement errors. Nonetheless, these findings suggest that the electrical and mechanical properties of PDMS changed when doped with nanoparticles.

The results for the PDMS samples doped with nanoparticles imply that the method has to be optimised further. In the case of PDMS 52A sample, newer samples with thicknesses of 52 µm and inferior values could be made in the future to clarify the results.

5.4 Discussion of factors influencing the results

The preceding results had setup issues that affected the results. The linear motor slightly rotates while moving, making predictions on the part of the moving sample that hits the fixed sample more difficult. To address this issue, the moving sample was attached with epoxy at a 90° angle in relation to the fixed sample, generating a cross shape

when they collided to prevent the moving sample from hitting the screws that held the fixed sample's supporting plate in place. This reduced the area of contact between samples, resulting in a loss of performance in the TENG, but in exchange, the homogeneity of the distributed forces between samples is assured, boasting performance. Another issue produced by the linear motor's rotation is the unscrewing of both sides of the tube, one connected to the linear motor and the other to the moving sample. While the first can be fastened during the experiment, the moving sample cannot be fastened, causing the position to change and the contact area to rise, causing previously unaffected fixed sample portions to charge up. By increasing the contact area during the experiment, this effect falsely enhances the output results. The only solution to this problem is to secure the sample tightly enough to reduce the possibility of unscrewing.

The other problem was that the polyurethane foam only withstood temperatures of 70 $^{\circ}C$ for long periods of time and was the best foam available at the time because the silicon rubber, despite withstanding temperatures of 200 $^{\circ}C$, was not compressible, preventing the moving sample from hitting with uniformity in the fixed sample. This caused a loss of performance even with a hole for the cables that connected the electrode to the measuring devices in an attempt to make a more uniform collision. There was also an issue with the double-sided duct tape failing to stick to the silicon rubber, whereas the polyurethane foam did not.

The polyurethane foam suffers mechanical wear from continual operation, as evidenced by touching an used and a newer foam, with the used being softer than the newer. Nevertheless, we concluded that it was the continuous operation that actually affects the foam mechanical properties, as the parts of the foam not compressed by the sample had the original consistency, ruling out temperature as a wear factor. However, this effect has no significant impact on the result obtained (Fig. 5.11).

The results in Fig. 5.11 rule out the foam as a cause of the decline in performance with the third data acquisition in the charging process, leaving only the possibility that the samples deteriorate at temperatures ranging from 70 $^{\circ}C$ to 100 $^{\circ}C$.

Another topic of discussion is the change in size of the samples from 3×4 cm^2 to 2×6 cm^2. Because the samples formed a 90° angle between them, the contact area shrank from 6 to 4 cm^2. The force distribution throughout the contact region was improved as a result of the moving sample colliding in parallel with the fixed sample and remaining in this state when compressing the foam during the collision phase. Throughout the experiment,

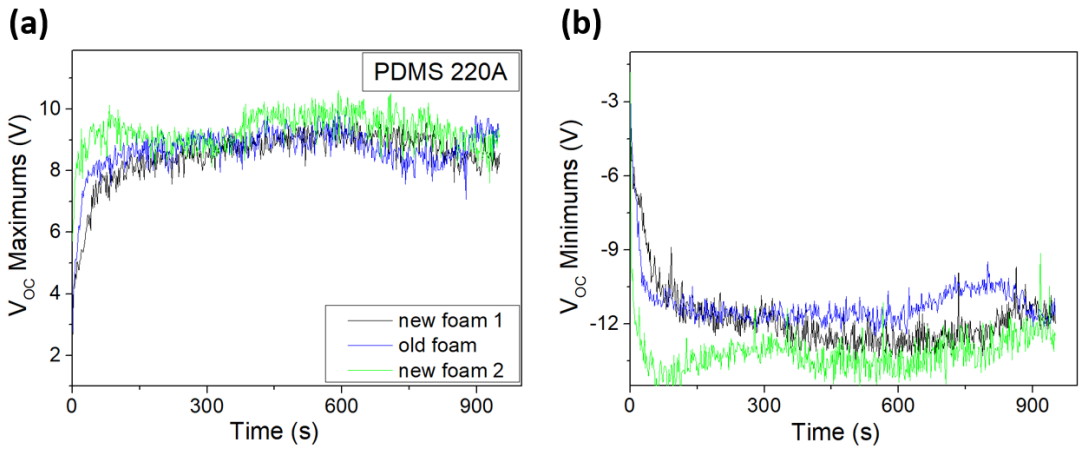

FIGURE 5.11: Room temperature measurements of the **(a)** maximum and **(a)** minimum peaks for different foams. The new foams 1 and 2 had never been used before this experiment, whereas the old foam had been used for 5 to 6 hours.

the latter part was the most difficult to ensure with PDMS 220B and PDMS 220C samples. However, with the PDMS 220A sample, the extra length made it easier to strike the centre of the sample, eliminating the prior problem. This inconsistency between PDMS 220B and PDMS 220C samples contributed to the performance drop as compared to PDMS 220A sample.

Another issue is that copper and aluminium moving samples oxidise in contact with air, reducing TENG performance. To give consistency to the results, the aluminium sample was sanded with sandpaper and cleaned with a paper tissue dipped in ethanol and

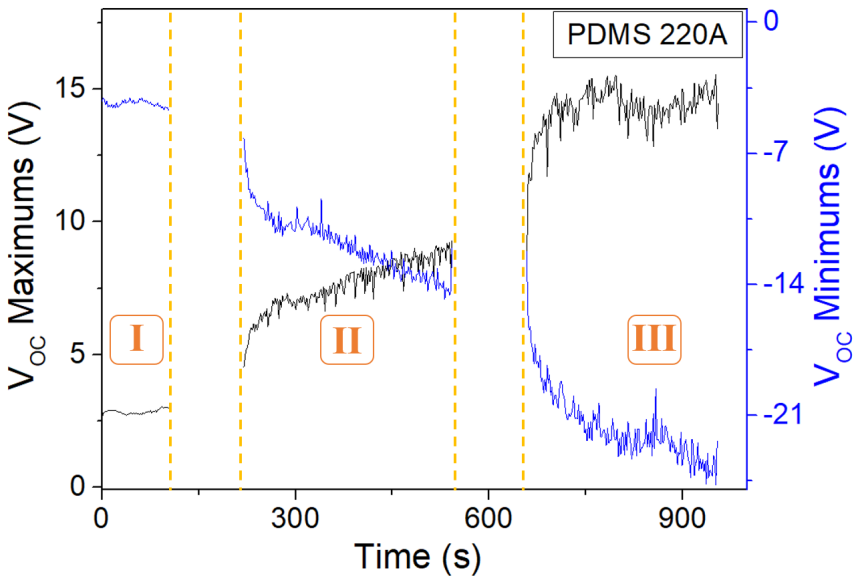

FIGURE 5.12: Charging aluminium and PDMS 220A samples to saturation without cleaning (**I**), sanding and cleaning the aluminium sample with a paper tissue to remove dust (**II**), and cleaning with acetone and ethanol (**III**).

another with acetone. In Fig. 5.12, the charging process is compared between uncleaned and treated samples.

While the improvement is significant when compared to doing nothing (Fig. 5.12 I) or simply sanding the sample (Fig. 5.12 II), the performance improves only at temperatures close to room temperature, as shown in Fig. 5.13, and at higher temperatures, the performance is below the measurements without cleaning. The current exhibits a similar tendency to that shown in Fig. 5.13. This is because acetone and ethanol are volatile and evaporate quickly at higher temperatures. Rubbing against the moving sample may induce charges, such as ions from paper, acetone, or ethanol, which may disperse from the sample at higher temperatures. This was a brief experience, and further investigation is required.

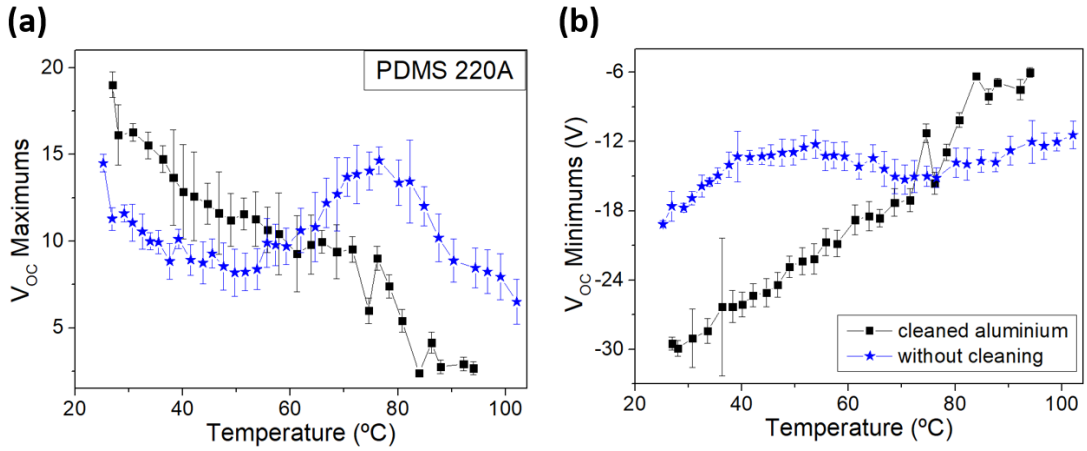

FIGURE 5.13: Voltage **(a)** maximums and **(b)** minimums as a function of the temperature to compare an uncleaned aluminium sample with a sanded and cleaned one as a function of the temperature.

Chapter 6

Conclusion and future work

6.1 Conclusions

In this work, a better understanding of TENGs' performance was achieved.

In the numerical simulation tendencies, the increase in the area (thickness) caused an increase (decrease) in the short circuit current and in the maximum output power. This agreed with Niu's model for contact-separation TENGs. However, the open circuit voltage did not agree with Niu's model and it was confirmed that the smaller (larger) area (thickness) led to fewer local electrical fields being perpendicular to the plane of the triboelectric materials, breaking the Gauss law. This was related with the fact of the area not being far greater than the distance between triboelectric materials. Comparisons were done between a nanoparticle-doped material and a material with the equivalent relative permittivity, and the results matched in the open circuit voltage, short circuit current, and current, with the other parameters agreeing only in tendencies. The charge correction study provided a better understanding of how surface charge density affects relative permittivity, with increased surface charge density of a material contributing indirectly to a material's relative permittivity rise, improving TENGs' performance.

The numerical simulations and experimental setup results confirmed that the higher the load resistance, the slower the charge flowed, leading to a greater decay after the peaks. In the numerical simulations, a delay shift in the separation peaks was observed, which increased with the load resistance rise, and, in the open circuit voltage condition, these peaks occurred at the maximum distance between triboelectric materials, agreeing with Niu's model predictions.

Temperature studies confirmed that TENG performance drops with increasing temperature due to sample degradation and the thermionic effect. With new samples of PDMS, the first acquisition of data may restructure the surface, enhancing the performance for the second acquisition, but with subsequent acquisitions, the degradation of PDMS samples justifies the drop in TENGs' performance.

6.2 Future work

This work opens different options to further understand the TENG behaviour by varying relevant parameters. In the numerical simulations, a further understanding of why the open circuit voltage does not follow the expected area and material thickness tendencies is necessary. An extension of these studies by adding temperature as a factor and seeing how the properties of the materials are affected would also be interesting. Furthermore, a simulation of a contact-separation TENG with a shorter border on one of the sides, 2 to 3 cm to simulate a real experiment would provide a better understanding of how the results of the experimental setup are affected.

The process of manufacturing nanoparticle-doped PDMS samples needs further improvement to guarantee a more uniform distribution. A proposal to test is the extension of the duration of magnetic stirring, using a water bath instead of a hot plate to ensure that an adequate temperature is used, and the use of a volumetric flask instead of a beaker. The crucial thing here is to keep toluene from evaporating too quickly.

In the experimental setup, only the metal-dielectric contact-separation TENG case was tested. It would be interesting to investigate a dielectric-dielectric case using materials such as nylon and PTFE, which did not work for the setup solutions found throughout the experiment. Furthermore, the polyurethane foam was not ideal for use at higher temperatures, limiting the setup's operational range. Acquiring and adapting the setup to a silicon foam that can work at temperatures as high as 200 °C would offer new possibilities to understand the performance of the TENG at higher temperatures.

Finally, the effect of temperature on sample restructuring and deterioration, as well as the effects of cleaning with ethanol and acetone and sanding on TENG performance, are significant aspects for future applications and a better understanding of how the samples are affected. This would focus on mitigating the degradable features with temperature variation that affect TENG performance.

Appendix A

Publications and conferences attended

A.1 Oral presentations

- Carlos Callaty, Isabel Gonçalves, Cátia Rodrigues, João Ventura, "Influence of materials properties in the performance of new triboelectric energy harvesters", Alternative energy materials 2022 (AEM2022), London, England, April 6^{th} 2022.
- Carlos Callaty, Isabel Gonçalves, Cátia Rodrigues, João Ventura, "Simulations of triboelectric nanogenerators and performance optimization", Investigação jovem da universidade do Porto (IJUP 2022), Porto, Portugal, May 4^{th} 2022.

A.2 Poster presentations

- Carlos Callaty, Isabel Gonçalves, Cátia Rodrigues, João Ventura, "Influence of materials properties in the performance of new triboelectric energy harvesters", Doctoral congress in engineering, Porto, Portugal, June 28^{th} 2022 (Fig. A.1).
- Carlos Callaty, Isabel Gonçalves, Cátia Rodrigues, João Ventura, "Performance optimization of triboelectric nanogenerators", FÍSICA 2022, Porto, Portugal, September 8^{th} 2022 (Fig. A.2).

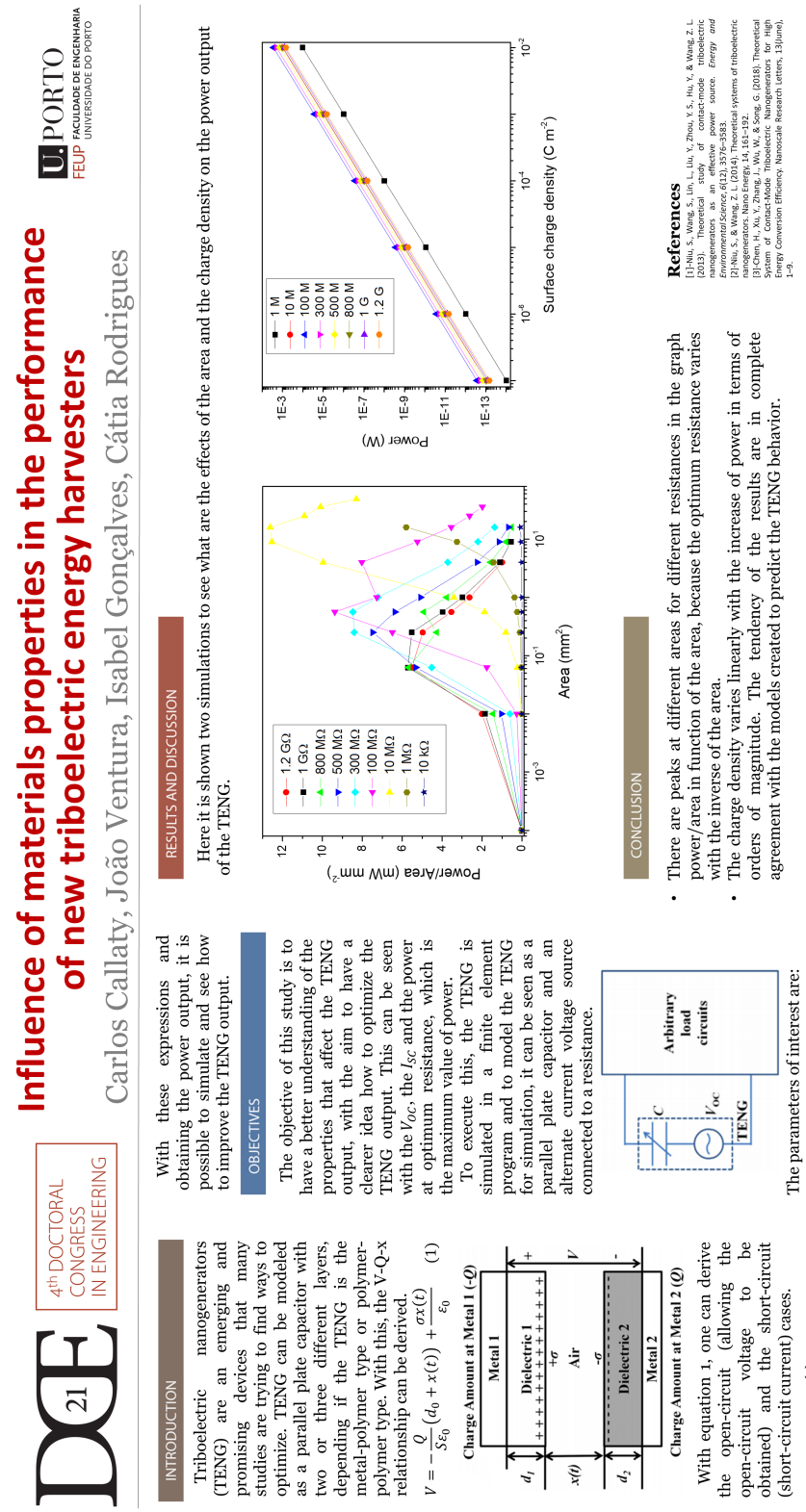

FIGURE A.1: Poster presented at the conference doctoral congress in engineering 2021 (DCE21) on June 28th 2021.

IFIMUP
Instituto de Física de Materiais Avançados, Nanotecnologia e Fotónica
Universidade do Porto

U.PORTO
FACULDADE DE CIÊNCIAS
UNIVERSIDADE DO PORTO

Performance optimization of triboelectric nanogenerators

Carlos Callaty[1], Isabel Gonçalves[1], Catia Rodrigues[1] and João Ventura[1]

[1]IFIMUP and Department of Physics and Astronomy, University of Porto, Portugal,
up201304115@edu.fc.up.pt

Summary

Triboelectric nanogenerators (TENG) are an environmentally friendly and promising energy harvest device that converts mechanical energy into electrical energy [1]. Using the contact separation TENG configuration, numerical simulations were carried out, based on Niu's model [2] to further optimise the performance of the TENG for the following parameters: area, thickness, and relative permittivity. In the relative permittivity study, a comparison of PDMS with nanoparticle doping and PDMS with the equivalent relative permittivity of the prior material is made.

Numerical methods

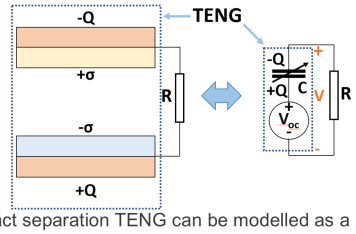

The contact separation TENG can be modelled as a parallel plate capacitor. Using a finite method for the simulations, the open-circuit voltage, the short circuit current, and the optimum resistance were used to characterise the tendencies of the TENG varying parameters, such as, area, thickness, and relative permittivity, according to Niu's model V-q-x relation:

$$V = -\frac{Q}{S\varepsilon_0}\left(\frac{d_1}{\varepsilon_{r_1}} + \frac{d_2}{\varepsilon_{r_2}} + x(t)\right) + \frac{\sigma x(t)}{\varepsilon_0}$$

The equivalent effective relative permittivity can be described as [3]:

$$\varepsilon_{r_{eff}} = \varepsilon_{r_1} f_1 + \varepsilon_{r_2} f_2$$

Relative permittivity

Niu's model states that as the concentration of nanoparticles or relative permittivity increases, both the open circuit voltage and the short circuit current remain constant. This is supported by the results. However, for the voltage values using a resistance near the peak of power, the numerical values between the effective relative permittivity and doped PDMS with nanoparticles do not match.

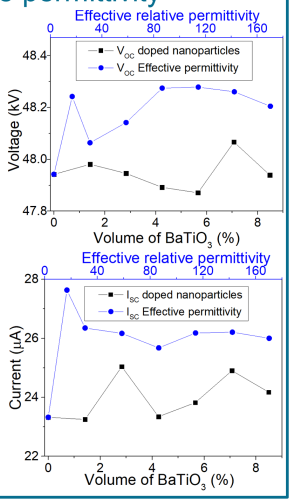

Area and thickness

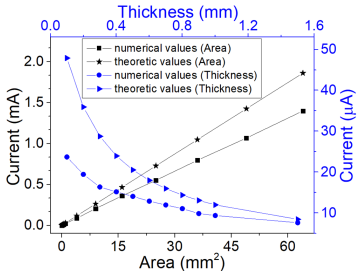

The short circuit current tendencies for the material thickness present on the TENG decrease as the thickness rises, but the short circuit current increases as the area increases, as predicted by Niu's model.

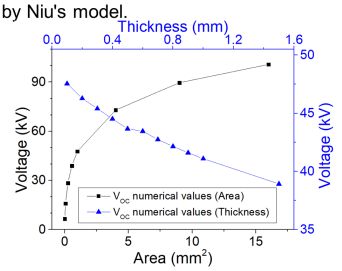

According to Niu's model, the open circuit voltage should be constant with the area and thickness variation. However, due to the area being of the magnitude order of the distance between electrodes, the gauss law does not hold well, with the decrease (increase) of the area (thickness), resulting in the local electrical fields not being perpendicular to the plane of the TENG .

Conclusions

- The results for the short circuit current of the varied parameters agree with Niu's model.
- The open circuit voltage results do not agree with Niu's model due to the gauss law not holding well for smaller (larger) areas (thickness).
- The relative permittivity study results between PDMS doped with nanoparticles and the equivalent effective relative permittivity only agree with each other in the open circuit, current, and short circuit current results.

References:

[1] Lin, Z., Chen, J., & Yang, J. (2016). *Journal of Nanomaterials*,

[2] Niu, S., Wang, S., Lin, L., Liu, Y., Zhou, Y. S., Hu, Y., & Wang, Z. L. (2013).*Environmental Science*, *6*(12), 3576–3583.

[3] Chen, J., Guo, H., He, X., Liu, G., Xi, Y., Shi, H., & Hu, C. (2016). *ACS Applied Materials and Interfaces*, *8*(1), 736–744.

Acknowledgements:

The authors acknowledge funding from projects I.NANO.WEC – FA 02 2017 002, HarshEnergy-739797 and UTAP-EXPL/NTec/0021/2017. FCT, ATTRACT, FSE/POPH, FEDER, COMPETE and ON2 are also acknowledged. The authors also acknowledge support from the ICON funded by Lloyd's Register Foundation. C. Rodrigues is thankful to FCT for grant SFRH/BD/147811/2019. The authors acknowledge FCT and IFIMUP for the support from projects UIDB/04968/2021 and UIDP/04968/2021

FIGURE A.2: Poster presented at the conference FÍSICA 2022 on September 8^{th} 2022.

Bibliography

[1] C. Zhang, Z. L. Wang, S. Niu, and Y. Zi, *Triboelectric Nanogenerators*, 1st ed. Springer Cham, 2016.

[2] A. Toreti, D. Bavera, J. Acosta Navarro, C. Cammalleri, A. de Jager, C. Di Ciollo, A. Hrast Essenfelder, W. Maetens, D. Magni, D. Masante, M. Mazzeschi, S. Niemeyer, and J. Spinoni, "Drought in Europe – August 2022," *Publications Office of the European Union, Luxembourg, JRC130493*, p. 24, 2022.

[3] P. Shukla, J. Skea, R. Slade, R. van Diemen, E. Haughey, J. Malley, M. Pathak, and J. P. Pereira, *Climate Change and Land: an IPCC special report on climate change, desertification, land degradation, sustainable land management, food security, and greenhouse gas fluxes in terrestrial ecosystems*. Cambridge University Press, 2019.

[4] Z. Liu, P. Ciais, Z. Deng, R. Lei, S. Davis, S. Feng, B. Zheng, D. Cui, X. Dou, B. Zhu, R. Guo, P. Ke, T. Sun, C. Lu, P. He, Y. Wang, X. Yue, Y. Wang, Y. Lei, and H. Schellnhuber, "Near-real-time monitoring of global CO_2 emissions reveals the effects of the covid-19 pandemic," *Nature Communications*, vol. 11, 10 2020.

[5] H. Akinaga, "Recent advances and future prospects in energy harvesting technologies," *Japanese Journal of Applied Physics*, vol. 59, no. 11, 2020.

[6] B. Pozo, J. I. Garate, J. Á. Araujo, and S. Ferreiro, "Energy harvesting technologies and equivalent electronic structural models - review," *Electronics (Switzerland)*, vol. 8, no. 5, pp. 1–31, 2019.

[7] A. D. Ball, F. Gu, R. Cattley, X. Wang, and X. Tang, "Energy harvesting technologies for achieving self-powered wireless sensor networks in machine condition monitoring: A review," *Sensors (Switzerland)*, vol. 18, no. 12, 2018.

[8] R. Schmela, Michael; Beauvais, Aurélie; Chevillard, Naomi; Paredes, Mariano Guillén; Heisz, Máté; Rossi, "Global Market Outlook For Solar Power," *Global Market Outlook*, p. 92, 2018. [Online]. Available: http://www.solarpowereurope.org/wp-content/uploads/2019/05/SolarPower-Europe-Global-Market-Outlook-2019-2023.pdf

[9] A. B. Djurišić, F. Z. Liu, H. W. Tam, M. K. Wong, A. Ng, C. Surya, W. Chen, and Z. B. He, "Perovskite solar cells - An overview of critical issues," *Progress in Quantum Electronics*, vol. 53, pp. 1–37, 2017.

[10] A. NECHIBVUTE, A. CHAWANDA, N. TARUVINGA, and P. LUHANGA, "Radio Frequency Energy Harvesting Sources," *Acta Electrotechnica et Informatica*, vol. 17, no. 4, pp. 19–27, 2017.

[11] S. Cao and J. Li, "A survey on ambient energy sources and harvesting methods for structural health monitoring applications," *Advances in Mechanical Engineering*, vol. 9, no. 4, pp. 1–14, 2017.

[12] S. B. M. Deshmukh, A. Krishnamoorthy, V. K. Bhojwani, A. Pandhare, A. M. Umbarkar, G. P. Patil, K. B. Jadhav, and A. R. Todkar, "An overview of the applications and performance characteristics of the thermoelectric devices," *ARPN Journal of Engineering and Applied Sciences*, vol. 12, no. 7, pp. 2063–2071, 2017.

[13] S. B. Riffat and X. Ma, "Thermoelectrics: A review of present and potential applications," *Applied Thermal Engineering*, vol. 23, no. 8, pp. 913–935, 2003.

[14] G. Sebald, D. Guyomar, and A. Agbossou, "On thermoelectric and pyroelectric energy harvesting," *Smart Materials and Structures*, vol. 18, no. 12, 2009.

[15] A. Thakre, A. Kumar, H. C. Song, D. Y. Jeong, and J. Ryu, "Pyroelectric energy conversion and its applications—flexible energy harvesters and sensors," *Sensors (Switzerland)*, vol. 19, no. 9, 2019.

[16] J. Davidson and C. Mo, "Recent Advances in Energy Harvesting Technologies for Structural Health Monitoring Applications," *Smart Materials Research*, vol. 2014, pp. 1–14, 2014.

[17] C. Dagdeviren, B. D. Yang, Y. Su, P. L. Tran, P. Joe, E. Anderson, J. Xia, V. Doraiswamy, B. Dehdashti, X. Feng, B. Lu, R. Poston, Z. Khalpey, R. Ghaffari, Y. Huang, M. J.

Slepian, and J. A. Rogers, "Conformal piezoelectric energy harvesting and storage from motions of the heart, lung, and diaphragm," *Proceedings of the National Academy of Sciences of the United States of America*, vol. 111, no. 5, pp. 1927–1932, 2014.

[18] C. Wu, A. C. Wang, W. Ding, H. Guo, and Z. L. Wang, "Triboelectric Nanogenerator: A Foundation of the Energy for the New Era," *Advanced Energy Materials*, vol. 9, no. 1, pp. 1–25, 2019.

[19] D. J. Lacks and T. Shinbrot, "Long-standing and unresolved issues in triboelectric charging," *Nature Reviews Chemistry*, vol. 3, no. 8, pp. 465–476, 2019. [Online]. Available: http://dx.doi.org/10.1038/s41570-019-0115-1

[20] S. Pan and Z. Zhang, "Fundamental theories and basic principles of triboelectric effect: A review," *Friction*, vol. 7, no. 1, pp. 2–17, 2019.

[21] F. Shen, D. Zhang, Q. Zhang, Z. Li, H. Guo, Y. Gong, and Y. Peng, "Influence of temperature difference on performance of solid-liquid triboelectric nanogenerators," *Nano Energy*, vol. 99, no. May, p. 107431, 2022. [Online]. Available: https://doi.org/10.1016/j.nanoen.2022.107431

[22] S. Niu and Z. L. Wang, "Theoretical systems of triboelectric nanogenerators," *Nano Energy*, vol. 14, pp. 161–192, 2014. [Online]. Available: http://dx.doi.org/10.1016/j.nanoen.2014.11.034

[23] Z. Lin, J. Chen, and J. Yang, "Recent Progress in Triboelectric Nanogenerators as a Renewable and Sustainable Power Source," *Journal of Nanomaterials*, vol. 2016, 2016.

[24] H. Askari, E. Hashemi, A. Khajepour, M. B. Khamesee, and Z. L. Wang, "Towards self-powered sensing using nanogenerators for automotive systems," *Nano Energy*, vol. 53, pp. 1003–1019, 2018. [Online]. Available: https://doi.org/10.1016/j.nanoen.2018.09.032

[25] J. Chen, H. Guo, X. He, G. Liu, Y. Xi, H. Shi, and C. Hu, "Enhancing performance of triboelectric nanogenerator by filling high dielectric nanoparticles into sponge pdms film," *ACS Applied Materials & Interfaces*, vol. 8, no. 1, pp. 736–744, 2016, pMID: 26654103. [Online]. Available: https://doi.org/10.1021/acsami.5b09907

[26] Y. Zhou, W. Deng, J. Xu, and J. Chen, "Engineering Materials at the Nanoscale for Triboelectric Nanogenerators," *Cell Reports Physical Science*, vol. 1, no. 8, p. 100142, 2020. [Online]. Available: https://doi.org/10.1016/j.xcrp.2020.100142

[27] S. Niu, S. Wang, L. Lin, Y. Liu, Y. S. Zhou, Y. Hu, and Z. L. Wang, "Theoretical study of contact-mode triboelectric nanogenerators as an effective power source," *Energy and Environmental Science*, vol. 6, no. 12, pp. 3576–3583, 2013.

[28] J. Shao, T. Jiang, W. Tang, X. Chen, L. Xu, and Z. L. Wang, "Structural figure-of-merits of triboelectric nanogenerators at powering loads," *Nano Energy*, vol. 51, pp. 688–697, 2018.

[29] H. Zhang, S. Feng, D. He, P. Molinié, and J. Bai, "Amplitude-variable output characteristics of triboelectric-electret nanogenerators during multiple working cycles," *Nano Energy*, vol. 63, 2019.

[30] C. Rodrigues, D. Nunes, D. Clemente, N. Mathias, J. M. Correia, P. Rosa-Santos, F. Taveira-Pinto, T. Morais, A. Pereira, and J. Ventura, "Emerging triboelectric nanogenerators for ocean wave energy harvesting: State of the art and future perspectives," *Energy and Environmental Science*, vol. 13, no. 9, pp. 2657–2683, 2020.

[31] J. W. Lee, B. U. Ye, and J. M. Baik, "Research Update: Recent progress in the development of effective dielectrics for high-output triboelectric nanogenerator," *APL Materials*, vol. 5, no. 7, 2017. [Online]. Available: http://dx.doi.org/10.1063/1.4979306

[32] H. Wang, J. Cheng, Z. Wang, L. Ji, and Z. L. Wang, "Triboelectric nanogenerators for human-health care," *Science Bulletin*, vol. 66, no. 5, pp. 490–511, 2021. [Online]. Available: https://doi.org/10.1016/j.scib.2020.10.002

[33] D. J. Griffiths, *Introduction to Electrodynamics*, 3rd ed. Prentice Hall, 1999.

[34] L. Li, "Dielectric properties of aged polymers and nanocomposites," *Iowa State University, 2011*, p. 128, 2011.

[35] Y. J. Kim, J. Lee, S. Park, C. Park, C. Park, and H. J. Choi, "Effect of the relative permittivity of oxides on the performance of triboelectric nanogenerators," *RSC Advances*, vol. 7, no. 78, pp. 49 368–49 373, 2017.

[36] A. Ahmed, I. Hassan, A. M. Pourrahimi, A. S. Helal, M. F. El-Kady, H. Khassaf, and R. B. Kaner, "Toward High-Performance Triboelectric Nanogenerators by Engineering Interfaces at the Nanoscale: Looking into the Future Research Roadmap," *Advanced Materials Technologies*, vol. 5, no. 11, pp. 1–20, 2020.

[37] S. Jang and J. H. Oh, "Rapid Fabrication of Microporous $BaTiO_3$/PDMS Nanocomposites for Triboelectric Nanogenerators through One-step Microwave Irradiation," *Scientific Reports*, vol. 8, no. 1, pp. 1–9, 2018. [Online]. Available: http://dx.doi.org/10.1038/s41598-018-32609-6

[38] X. Zhao, L. Li, B. Li, J. Zhang, and A. Wang, "Durable superhydrophobic/-superoleophilic PDMS sponges and their applications in selective oil absorption and in plugging oil leakages," *Journal of Materials Chemistry A*, vol. 2, no. 43, pp. 18 281–18 287, 2014. [Online]. Available: http://dx.doi.org/10.1039/C4TA04406A

[39] S. J. Choi, T. H. Kwon, H. Im, D. I. Moon, D. J. Baek, M. L. Seol, J. P. Duarte, and Y. K. Choi, "A polydimethylsiloxane (PDMS) sponge for the selective absorption of oil from water," *ACS Applied Materials and Interfaces*, vol. 3, no. 12, pp. 4552–4556, 2011.

[40] X. Ren, H. Lu, J. G. Zhou, P. L. G. Chong, W. Yuan, and M. Noh, "Porous Polydimethylsiloxane as a Gas-Liquid Interface for Microfluidic Applications," *Journal of Microelectromechanical Systems*, vol. 26, no. 1, pp. 120–126, 2017.

[41] J. Kim, H. Ryu, J. H. Lee, U. Khan, S. S. Kwak, H. J. Yoon, and S. W. Kim, "High Permittivity $CaCu_3Ti_4O_{12}$ Particle-Induced Internal Polarization Amplification for High Performance Triboelectric Nanogenerators," *Advanced Energy Materials*, vol. 10, no. 9, pp. 1–8, 2020.

[42] D. Tantraviwat, M. Ngamyingyoud, W. Sripumkhai, P. Pattamang, G. Rujijanagul, and B. Inceesungvorn, "Tuning the Dielectric Constant and Surface Engineering of a $BaTiO_3$/Porous PDMS Composite Film for Enhanced Triboelectric Nanogenerator Output Performance," *ACS Omega*, vol. 6, no. 44, pp. 29 765–29 773, 2021.

[43] A. C. Patsidis, "Barium titanate/polydimethylsiloxane nano/ microcomposites fabrication, morphology, dielectric response and functionality," *IET Nanodielectrics*, vol. 3, no. 1, pp. 14–19, 2020.

[44] S. Ke, P. Lin, H. Huang, H. Fan, and X. Zeng, "Mean-Field Approach to Dielectric Relaxation in Giant Dielectric Constant Perovskite Ceramics," *Journal of Ceramics*, vol. 2013, pp. 1–7, 2013.

[45] S. Lin, L. Xu, C. Xu, X. Chen, A. C. Wang, B. Zhang, P. Lin, Y. Yang, H. Zhao, and Z. L. Wang, "Electron Transfer in Nanoscale Contact Electrification: Effect of Temperature in the Metal–Dielectric Case," *Advanced Materials*, vol. 31, no. 17, pp. 1–9, 2019.

[46] B. Cheng, Q. Xu, Y. Ding, S. Bai, X. Jia, Y. Yu, J. Wen, and Y. Qin, "High performance temperature difference triboelectric nanogenerator," *Nature Communications*, vol. 12, no. 1, pp. 1–8, 2021.

[47] C. Xu, Y. Zi, A. C. Wang, H. Zou, Y. Dai, X. He, P. Wang, Y. C. Wang, P. Feng, D. Li, and Z. L. Wang, "On the Electron-Transfer Mechanism in the Contact-Electrification Effect," *Advanced Materials*, vol. 30, no. 15, pp. 1–9, 2018.

[48] C. Xu, A. C. Wang, H. Zou, B. Zhang, C. Zhang, Y. Zi, L. Pan, P. Wang, P. Feng, Z. Lin, and Z. L. Wang, "Raising the Working Temperature of a Triboelectric Nanogenerator by Quenching Down Electron Thermionic Emission in Contact-Electrification," *Advanced Materials*, vol. 30, no. 38, 2018.

[49] C. Xu, B. Zhang, A. C. Wang, W. Cai, Y. Zi, P. Feng, and Z. L. Wang, "Effects of Metal Work Function and Contact Potential Difference on Electron Thermionic Emission in Contact Electrification," *Advanced Functional Materials*, vol. 29, no. 29, 2019.

[50] X. Wen, Y. Su, Y. Yang, H. Zhang, and Z. L. Wang, "Applicability of triboelectric generator over a wide range of temperature," *Nano Energy*, vol. 4, pp. 150–156, 2014.

[51] C. X. Lu, C. B. Han, G. Q. Gu, J. Chen, Z. W. Yang, T. Jiang, C. He, and Z. L. Wang, "Temperature Effect on Performance of Triboelectric Nanogenerator," *Advanced Engineering Materials*, vol. 19, no. 12, pp. 1–8, 2017.

[52] C. Rodrigues, M. Kumar, M. P. Proenca, J. Gutierrez, R. Melo, A. Pereira, and J. Ventura, "Triboelectric energy harvesting in harsh conditions: Temperature and pressure effects in methane and crude oil environments," *Nano Energy*, vol. 72, no. March, 2020.

[53] A. C. Wang, B. Zhang, C. Xu, H. Zou, Z. Lin, and Z. L. Wang, "Unraveling Temperature-Dependent Contact Electrification between Sliding-Mode Triboelectric Pairs," *Advanced Functional Materials*, vol. 30, no. 12, pp. 1–9, 2020.

[54] X. Tao, S. Li, Y. Shi, X. Wang, J. Tian, Z. Liu, P. Yang, X. Chen, and Z. L. Wang, "Triboelectric Polymer with High Thermal Charge Stability for Harvesting Energy from 200 °C Flowing Air," *Advanced Functional Materials*, vol. 31, no. 49, 2021.

[55] M. Liu, J. Sun, and Q. Chen, "Influences of heating temperature on mechanical properties of polydimethylsiloxane," *Sensors and Actuators, A: Physical*, vol. 151, no. 1, pp. 42–45, 2009.

[56] A. Bamido, N. Shettigar, A. Thyagrajan, and D. Banerjee, "Investigation of the Temperature-Dependent Mechanical Properties of Polydimethylsiloxane (PDMS) Membrane for Thermo-Mechanical Applications," *InterSociety Conference on Thermal and Thermomechanical Phenomena in Electronic Systems, ITHERM*, vol. 2021-June, no. September, pp. 617–629, 2021.

[57] L. Li, X. Wang, P. Zhu, H. Li, F. Wang, and J. Wu, "The electron transfer mechanism between metal and amorphous polymers in humidity environment for triboelectric nanogenerator," *Nano Energy*, vol. 70, no. January, p. 104476, 2020. [Online]. Available: https://doi.org/10.1016/j.nanoen.2020.104476

[58] V. Nguyen and R. Yang, "Effect of humidity and pressure on the triboelectric nanogenerator," *Nano Energy*, vol. 2, no. 5, pp. 604–608, 2013. [Online]. Available: http://dx.doi.org/10.1016/j.nanoen.2013.07.012

[59] Z. Yi, D. Liu, L. Zhou, S. Li, Z. Zhao, X. Li, Z. L. Wang, and J. Wang, "Enhancing output performance of direct-current triboelectric nanogenerator under controlled atmosphere," *Nano Energy*, vol. 84, no. February, p. 105864, 2021. [Online]. Available: https://doi.org/10.1016/j.nanoen.2021.105864

[60] K. Han, W. Tang, J. Chen, J. Luo, L. Xu, and Z. L. Wang, "Effects of Environmental Atmosphere on the Performance of Contact–Separation Mode TENG," *Advanced Materials Technologies*, vol. 4, no. 2, pp. 1–8, 2019.

[61] J. Fu, G. Xu, C. Li, X. Xia, D. Guan, J. Li, Z. Huang, and Y. Zi, "Achieving Ultrahigh Output Energy Density of Triboelectric Nanogenerators in High-Pressure Gas Environment," *Advanced Science*, vol. 7, no. 24, pp. 1–8, 2020.

[62] K. Dong, X. Peng, R. Cheng, and Z. L. Wang, "Smart Textile Triboelectric Nanogenerators: Prospective Strategies for Improving Electricity Output Performance," *Nanoenergy Advances*, vol. 2, no. 1, pp. 133–164, 2022.

[63] G. Min, Y. Xu, P. Cochran, N. Gadegaard, D. M. Mulvihill, and R. Dahiya, "Origin of the contact force-dependent response of triboelectric nanogenerators," *Nano Energy*, vol. 83, no. January, p. 105829, 2021. [Online]. Available: https://doi.org/10.1016/j.nanoen.2021.105829

[64] Y. Xu, G. Min, N. Gadegaard, R. Dahiya, and D. M. Mulvihill, "A unified contact force-dependent model for triboelectric nanogenerators accounting for surface roughness," *Nano Energy*, vol. 76, no. July, 2020.

[65] C. Rodrigues, A. Gomes, A. Ghosh, A. Pereira, and J. Ventura, "Power-generating footwear based on a triboelectric-electromagnetic-piezoelectric hybrid nanogenerator," *Nano Energy*, vol. 62, no. January, pp. 660–666, 2019. [Online]. Available: https://doi.org/10.1016/j.nanoen.2019.05.063

[66] *COMSOL multiphysics reference manual*, 2019, last visited on 6/10/2021. [Online]. Available: https://doc.comsol.com/5.5/doc/com.comsol.help.comsol/COMSOL_ReferenceManual.pdf

[67] Improving convergence in nonlinear time dependent models. Last visited on 3/10/2021. [Online]. Available: https://www.comsol.com/support/knowledgebase/1127

[68] G. Casquillas, F. Bertholle, E. Terriac, and M. Le Berre, "PDMS thickness vs spin-coating speed," *Elveflow*, vol. 1, pp. 2–3, 2005. [Online]. Available: https://www.elveflow.com/microfluidic/PDMSthicknessVSspinspeed.pdf

[69] R. A. Serway and J. W. Jewett Jr., *Physics for Scientists & Engineers - with Modern Physics*, 8th ed. Brooks/Cole, 2010.

[70] Z. Wang, W. Liu, J. Hu, W. He, H. Yang, C. Ling, Y. Xi, X. Wang, A. Liu, and C. Hu, "Two voltages in contact-separation triboelectric nanogenerator: From asymmetry to symmetry for maximum output," *Nano Energy*, vol. 69, no. December 2019, 2020.

[71] R. D. Dharmasena, "Inherent asymmetry of the current output in a triboelectric nanogenerator," *Nano Energy*, vol. 76, no. June, p. 105045, 2020. [Online]. Available: https://doi.org/10.1016/j.nanoen.2020.105045